Doctoral Thesis

Gas-Mediated Electron Beam Induced Etching

A thesis submitted in fulfilment of the requirements
for the degree of Doctor of Philosophy

School of Physics and Advanced Materials
University of Technology, Sydney

Author
Aiden Alexander Martin

Supervisors
Prof. Milos Toth
Dr. Charlene Lobo
Prof. Matthew Phillips
A. Prof. Igor Aharonovich

June 2015

Certificate of Original Authorship

I, Aiden Alexander Martin, certify that the work in this thesis titled, 'Gas-Mediated Electron Beam Induced Etching' has not previously been submitted for a degree nor has it been submitted as part of requirements for a degree except as fully acknowledged within the text.

I also certify that the thesis has been written by me. Any help that I have received in my research work and the preparation of the thesis itself has been acknowledged. In addition, I certify that all information sources and literature used are indicated in the thesis.

Signature of Student: Production Note: Signature removed prior to publication.

Date: 12 June 2015

Acknowledgements

I would like to express my deepest thanks to Professor Milos Toth. I am sincerely grateful for the opportunities you have provided during this work and for the future. I would also like to thank Dr. Charlene Lobo, Professor Matthew Phillips and Associate Professor Igor Aharonovich. All of you have given me exceptional guidance and made my time at UTS a truly enjoyable experience.

My sincere thanks to Associate Professor Mike Ford, Mr. Geoff McCredie, Mrs. Katie McBean, Dr. Angus Gentle and Mr. Mark Berkahn for your support over the last decade of work and study.

To my fellow students, I would like to thank all of you for your friendship. A special thank you to James Bishop, Toby Shanley, Cameron Zachreson, Alan Bahm and Russell Sandstrom for allowing me to collaborate with you on your research projects. James Bishop assisted with the electron beam induced etching of diamond experiments featured in Chapter 4.

Thank you Dr. Eric Silver, Dr. Ting Lin, Mr. Gerry Austin and Mr. David Caldwell at the Harvard-Smithsonian Center for Astrophysics for your generosity and stimulating discussions during our collaboration. Eric Silver and Ting Lin performed the energy-dispersive x-ray spectroscopy measurements and hosted the equipment used for the experiments featured in Chapter 8.

I would like to thank FEI Company for their financial and scientific support. The training provided by your organisation has allowed me to travel the world and work with amazing people. Steven Randolph and Aurelien Botman of FEI Company irradiated a diamond sample with oxygen ions for the study in Chapter 6. Thank you to the Science and Industry Endowment Fund for the John Stocker Postgraduate Scholarship, which has enabled collaborations with international researchers. I would also like to thank the Australian Nanotechnology Network and Microscopy Society of America for their conference travel funding.

A special thanks to my family for always nurturing my creativity and preparing me for all of lifes challenges. Lastly and most of all I would like to thank my wife Amanda. Your support, encouragement and love made this work possible.

Contributing Publications

Peer-reviewed publications that contributed to this work:

- Dynamic surface site activation: A rate limiting process in electron beam induced etching, **A. A. Martin**, M. R. Phillips and M. Toth, ACS Appl. Mater. Interfaces, 5 (16), p. 8002 – 8007, 2013
- Subtractive 3D printing of optically active diamond structures, **A. A. Martin**, M. Toth and I. Aharonovich, Sci. Rep., 4, 5022, 2014
- Cryogenic electron beam induced chemical etching, **A. A. Martin** and M. Toth, ACS Appl. Mater. Interfaces, 6 (21), p. 18457 – 18460, 2014
- Maskless milling of diamond by a focused oxygen ion beam, **A. A. Martin**, S. Randolph, A. Botman, M. Toth and I. Aharonovich, Sci. Rep., 5, 8958, 2015, 2015

Non-Contributing Publications

Peer-reviewed publications not featured in this work containing research undertaken during the PhD program:

- Electron beam induced chemical dry etching and imaging in gaseous NH_3 environments, C. J. Lobo, **A. Martin**, M. R. Phillips and M. Toth, Nanotechnology, 23 (37), p. 375302, 2012. This work demonstrated NH_3-mediated electron beam induced etching (EBIE) of carbonaceous material. Etching is highly material selective, and does not volatilise ultra nano-crystalline diamond to any significant degree. The process is also effective at preventing the buildup of residual hydrocarbon impurities that often compromise EBIE, electron beam induced deposition (EBID) and electron imaging.
- Role of activated chemisorption in gas-mediated electron beam induced deposition, J. Bishop, C. J. Lobo, **A. A. Martin**, M. Ford, M. R. Phillips and M. Toth, Phys. Rev. Lett., 109 (14), p. 146103, 2012. This work investigated the rate kinetics of EBID using tetraethoxysilane (TEOS) precursor. Chemisorbed states govern the adsorbate coverage and EBID rates at elevated substrate temperatures. The results show how EBID can be used to deposit high purity materials and characterise the rates and energy barriers that govern precursor adsorption.
- Localized chemical switching of the charge state of nitrogen-vacancy luminescence centers in diamond, T. Shanley, **A. A. Martin**, I. Aharonovich and M. Toth, Appl. Phys. Lett., 105 (6), p. 063103, 2014. This work demonstrated electron beam induced functionalisation of diamond. Fluorination of H-terminated diamond is realised by electron beam stimulated desorption of surface adsorbed H_2O in the presence of NF_3.
- Electron beam-controlled modification of luminescent centers in a polycrystalline diamond thin film, C. Zachreson, **A. A. Martin**, M. Toth and I. Aharonovich, ACS Appl. Mater. Interfaces, 6 (13), p. 10367 - 10372, 2014. This work investigated room temperature activation of several luminescence centres in diamond through a

thermal mechanism that is catalysed by an electron beam. Cathodoluminescence activation kinetics were measured in real-time and attributed to electron induced dehydrogenation of nitrogen-vacancy-hydrogen clusters and dislocation defects.

- Study of narrowband single photon emitters in polycrystalline diamond films, R. G. Sandstrom, Olga Shimoni, **A. A. Martin** and I. Aharonovich, Appl. Phys. Lett., 105 (18), p. 181104, 2014. This work investigated the photophysical properties of bright, narrowband single photon emitters in diamond films grown on a silicon substrate by microwave plasma chemical vapor deposition.

Contents

Certificate of Original Authorship ii

Acknowledgements iii

Contributing Publications v

Non-Contributing Publications vi

List of Figures xiii

List of Tables xv

Abbreviations xvii

Abstract xix

1 Motivation and Background 1
1.1 Introduction 1
1.2 Background 3
1.2.1 EBIE 3
1.2.2 Standard Model of EBIE 4
1.2.3 Silicon 6
1.2.4 Carbon 11
1.3 Experimental Techniques 15
1.3.1 Environmental Reaction Cell 15
1.3.2 Material Characterisation Techniques 17
1.3.3 Material-Particle Interaction Simulation 19
1.4 Description of Chapters 20

2 Electron Beam Induced Etching of Carbon 23
2.1 Abstract 23
2.2 Introduction 23
2.3 Results and Discussion 25
2.4 Conclusions 30
2.5 Supporting Information 31
2.5.1 Conditioning Procedures 31

2.5.2 Materials . . . 32
2.5.3 Experimental Parameters . . . 32
2.5.4 Environmental Reaction Cell . . . 32
2.5.5 Modelling Parameters . . . 33

3 Dynamic Surface Site Activation: A Rate Limiting Process in Electron Beam Induced Etching 35
3.1 Abstract . . . 35
3.2 Introduction . . . 35
3.3 Methods . . . 39
3.3.1 Modelling . . . 39
3.3.2 Experimental . . . 39
3.4 Results and Discussion . . . 40
3.4.1 Surface Site Activation . . . 40
3.4.2 EBIE of UNCD . . . 41
3.4.3 Generation of Chemically Active Defects During EBIE . . . 43
3.5 Conclusions . . . 46

4 Dynamic Formation of Topographic Patterns During EBIE of Single Crystal Diamond 49
4.1 Abstract . . . 49
4.2 Introduction . . . 50
4.3 Results and Discussion . . . 51
4.4 Conclusions . . . 57

5 Subtractive 3D Printing of Optically Active Diamond Nanostructures 59
5.1 Abstract . . . 59
5.2 Introduction . . . 60
5.3 Results and Discussion . . . 61
5.4 Conclusions . . . 64
5.5 Methods . . . 65
5.6 Supporting Information . . . 66

6 Maskless Milling of Diamond by a Focused Oxygen Ion Beam 69
6.1 Abstract . . . 69
6.2 Introduction . . . 69
6.3 Results and Discussion . . . 70
6.4 Conclusions . . . 76
6.5 Methods . . . 76

7 Cryogenic Electron Beam Induced Chemical Etching 79
7.1 Abstract . . . 79
7.2 Introduction . . . 79
7.3 Methods . . . 81
7.4 Results and Discussion . . . 82

7.5 Conclusions . . . 85
7.6 Supporting Information . . . 86
7.6.1 Notes . . . 86
7.6.2 Modelling Introduction . . . 87
7.6.3 Temperature Dependence of EBIE . . . 88
7.6.4 Arrhenius Analysis of Single Step EBIE Reactions . . . 89
7.6.5 Arrhenius Analysis of Multistep EBIE Reactions . . . 92
7.6.6 Model Input Parameters . . . 95

8 Extraction and Analysis of Microparticles Embedded in Silica Aerogel 97
8.1 Abstract . . . 97
8.2 Introduction . . . 98
8.3 Methods . . . 100
8.3.1 Detection of Particles by BSE Imaging . . . 100
8.3.2 Extraction of Particles by EBIE . . . 101
8.3.3 Analysis of Particles by X-ray Spectroscopy . . . 103
8.4 Results and Discussion . . . 104
8.4.1 Detection of Particles by BSE Imaging . . . 104
8.4.2 Extraction of Particles by EBIE . . . 105
8.4.3 Analysis of Particles by X-ray Spectroscopy . . . 107
8.5 Conclusions . . . 108

9 General Conclusions and Future Directions 111
9.1 General Conclusions . . . 111
9.2 Future Directions . . . 113

Bibliography 117

List of Figures

1.1 Simplified schematic of H_2O-mediated EBIE of carbon 3
1.2 Constant pressure and Clausing gas flow EBIE model 5
1.3 NASA's Stardust spacecraft 10
1.4 Silica aerogel keystone 11
1.5 Demonstration of EBIE resolution 12
1.6 Diamond NV colour-centre 14
1.7 CCD image of an eCell installed in the chamber of an FEI Nova NanoSEM 600 16
1.8 eCell configured for operation in a conventional differentially pumped SEM 17

2.1 Electron beam induced removal of carbon from graphene and lacy carbon . 25
2.2 Depths of pits produced in UNCD by EBIE under various environmental conditions and simplified schematic of the EBIE system 26
2.3 Concentration of H_2O, N_2 and Ar adsorbates calculated as a function of pressure 30

3.1 Simplified schematic of H_2O-mediated EBIE of carbon 37
3.2 Etch pit depth versus time, for H_2O-mediated EBIE of UNCD 42
3.3 Electron energy deposition profile, $\frac{\partial E}{\partial z}$, calculated for UNCD using electron energies E_0 of 5, 10 and 20 keV 43
3.4 Maximum depth of pits in UNCD fabricated using 5 and 10 keV electron beams, plotted as a function of etch time 46

4.1 SEM images of topographic features produced by H_2O-mediated EBIE of single crystal (001) orientated diamond 52
4.2 SEM image of topographic features produced by H_2O-mediated EBIE of single crystal (001) orientated diamond at 30° substrate tilt 54
4.3 SEM images of topographic features produced by NH_3-mediated EBIE of single crystal (001) orientated diamond 55
4.4 SEM images of topographic features produced by H_2O and NH_3-mediated EBIE of single crystal (111) orientated diamond 56

5.1 Schematic illustrations of H_2O-mediated EBIE 61
5.2 Diamond pillar fabricated by mask-based EBIE 62
5.3 Optical quality of a diamond pillar fabricated by EBIE 63
5.4 Beam-directed editing of Si-doped diamond micro-particles 65

5.5 Room temperature PL spectrum confirming the presence of the silicon-vacancy colour center with the characteristic ZPL at 738 nm 67

6.1 Optical quality of diamond structures fabricated using a focused oxygen ion beam 71
6.2 CL profiling of oxygen ion induced damage in diamond 73
6.3 Removal of damaged diamond material by EBIE 75

7.1 Etch pit depth versus substrate temperature for NF_3-mediated EBIE of silicon 82
7.2 Etch pit depth versus time measured for Si, SiO_2, SiC and Si_3N_4 etched by NF_3-mediated EBIE 83
7.3 Comparison between NF_3, XeF_2 and Cl_2-mediated EBIE of silicon 84
7.4 High resolution NF_3-mediated EBIE of silicon 86
7.5 Single step EBIE reactions 91
7.6 Multistep EBIE reactions 94

8.1 False colour image of the SEM configured for cryogenic EBIE 100
8.2 NF_3-mediated EBIE overview 102
8.3 Microcalorimeter 103
8.4 BSE imaging of sub-surface material 104
8.5 Simulation of BSE imaging of sub-surface material 106
8.6 Particle extracted from silica aerogel by NF_3-mediated EBIE 107
8.7 Elemental analysis of a particle extracted by EBIE 108
8.8 Localised elemental analysis of a particle extracted by EBIE 109

List of Tables

2.1 Depths of pits produced in UNCD by EBIE under various environmental conditions 26

Abbreviations

AFM	Atomic Force Microscope
BSE	Backscattered Electron
CASINO	Monte Carlo Simulation of Electron Trajectory in Solids
CCD	Charge-Coupled Device
CL	Cathodoluminescence
CVD	Chemical Vapour Deposition
DEA	Dissociative Electron Attachment
DEI	Dissociative Electron Ionisation
EBID	Electron Beam Induced Deposition
EBIE	Electron Beam Induced Etching
EDS	Energy-dispersive X-ray Spectroscopy
eCell	Environmental Reaction Cell
ESEM	Environmental Scanning Electron Microscope
FIB	Focused Ion Beam
HFCVD	Hot Filament Chemical Vapour Deposition
ICPS	Inductively Coupled Plasma Source
LN	Liquid Nitrogen
NASA	National Aeronautics and Space Administration
PLA	Pressure Limiting Aperture
RF	Radio Frequency
RRL	Reaction-rate Limited
NV	Nitrogen-Vacancy
NV^0	Neutral Nitrogen-Vacancy

NV^-	Negative Nitrogen-Vacancy
PL	Photoluminescence
PPM	Parts per Million
SEM	Scanning Electron Microscope
SCCM	Standard Cubic Centimetres per Minute
UNCD	Ultra Nano-crystalline Diamond
XANES	X-ray Absorption Near Edge Structure
ZPL	Zero Phonon Line

Abstract

Gas-mediated electron beam induced etching is a direct-write nanolithography technique. In this thesis, through experimental observation and numerical simulation, descriptions of reaction kinetics of electron beam induced etching were refined to include effects of residual contaminants, substrate material properties, and temperature dependence. Reaction kinetics of electron beam induced etching are of interest because they affect resolution, throughput, proximity effects, and topography of nanostructures and nanostructured devices fabricated by electron beam induced etching.

A number of mechanisms proposed in the literature for electron beam induced removal of carbon were shown to be insignificant. These include atomic displacements caused by knock-on by low energy electrons, electron beam heating, sputtering by ionised gas molecules, and chemical etching driven by a number of gases that include N_2. The behaviour ascribed to these mechanisms was instead explained by chemical etching caused by electron beam induced dissociation of residual contaminants such as H_2O present in the vacuum systems that are typically used for EBIE.

Reaction mechanisms in single crystal and ultra nano-crystalline diamond were shown to be dependent on substrate material properties. Single crystal diamond etch morphology is attributed to anisotropic etching along crystal planes, which varies with precursor composition. In contrast to single crystal diamond, etching of ultra nano-crystalline diamond was shown to proceed via an electron activated pathway. A refined electron beam induced etching model incorporating the role of electron induced damage in ultra nano-crystalline diamond yields higher order reaction kinetics, predicting a new reaction regime limited by the concentration of chemically active surface sites.

A temperature dependent, cryogenic electron beam induced etching technique was implemented to increase the residence time of adsorbates on the surface. This technique efficiently increases the rate of electron beam induced etching, demonstrated using nitrogen trifluoride as the etch precursor for silicon. Cryogenic cooling broadens the range of precursors that can be used for electron beam induced etching, and enables high-resolution,

deterministic etching of materials that are volatilised spontaneously by conventional etch precursors.

Determining the reaction kinetics of electron beam induced etching enables new applications in nanoscale material modification. Methods for the fabrication of optically active, functional diamond structures from single crystal diamond and rapid Stardust particle extraction were demonstrated. Electron beam induced etching is ideal for these applications, where high-resolution, damage-free etching is required.

Chapter 1

Motivation and Background

1.1 Introduction

Gas-mediate electron beam induced etching (EBIE) is a direct-write nanofabrication technique that enables site-specific modification of materials. The technique has many promising applications in materials research and development, but is underexploited because it is relatively new and poorly understood. The aim of this work was to advance fundamental understanding of the physicochemical processes behind EBIE, and develop advanced applications in materials physics and nanotechnology. In particular, the following defined research areas were investigated:

- Development of hardware and experimental protocols for robust, highly reproducible, quantitative EBIE studies (Chapters 2, 3 and 7).
- Influence of gas phase impurities, substrate surface structure, defects and electron beam damage on EBIE rate kinetics (Chapters 2, 3 and 4).
- Application of EBIE to materials used in photonics and optoelectronics, such as diamond, SiC, SiO_2 and Si (Chapters 3, 4, 5, 6 and 7).
- Application of EBIE for the removal of damage generated in single crystal diamond by a focused oxygen ion beam (Chapter 6).

- Application of EBIE for the extraction of NASA Stardust cometary microparticles from silica aerogels (Chapter 8).

These areas focus on materials that have scientific and industrial significance, and aspects of EBIE fundamentals that are poorly understood. This work utilised recently designed, unique instrumentation that enables EBIE research beyond limits imposed by existing commercially available systems. Quantitative experimental data were used to determine EBIE reaction mechanisms. The standard model of EBIE was expanded to include additional parameters including material structure and electron induced defect generation. These models were used to reproduce observed experimental growth kinetics. Development of hardware and applications for EBIE was done alongside scientific endeavours.

1.2 Background

1.2.1 EBIE

EBIE is a direct-write technique for nano- and micro-scale modification of surfaces in reactive gaseous environments. Nanoscale resolution is attainable [1], and fabrication of a 4 nm wide gap has been demonstrated in H_2O-mediated EBIE of carbon nanowires on electrically insulating, bulk quartz substrates [2]. The technique is analogous to gas-assisted focused ion beam (FIB) milling [1, 3]. However, EBIE is a chemical process that does not involve sputtering and ion implantation, and exhibits greater material selectivity than FIB processing [1].

EBIE is a dry, chemical process where a solid is irradiated with electrons in the presence of a precursor gas. Surface-adsorbed precursor molecules (e.g., H_2O) are dissociated by incident electrons, generating fragments (e.g., O^* and OH^*) [4] that react with the substrate to produce volatile species (e.g., CO and CO_2). The volatile species desorb and are removed by a pumping system, leaving a void in the substrate (Figure 1.1).

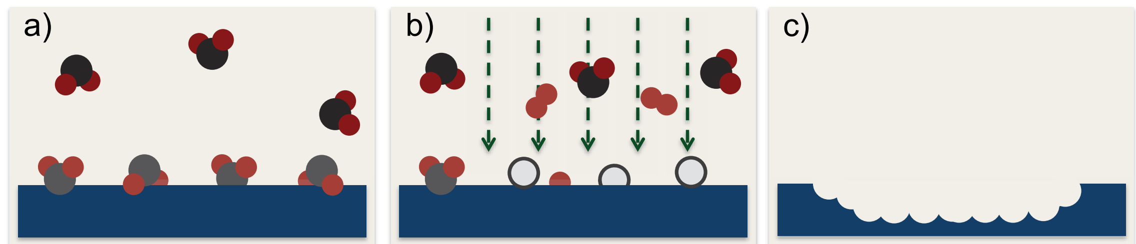

FIGURE 1.1: Simplified schematic of H_2O-mediated EBIE of carbon. a) H_2O adsorption on the surface. b) Generation of reactive fragments (e.g., O^* and OH^*) by incident and emitted electrons. c) Reaction between carbon and fragments produce volatile species (e.g., CO and CO_2) which desorb, leaving a void in the substrate.

EBIE has been demonstrated in a range of precursor-material combinations. Precursors used for EBIE include H_2O, O_2, NH_3, Cl_2, XeF_2, SF_6 and ClF_3 [1]. Materials where EBIE has been investigated include graphene [5–9], carbon nanotubes [10–13], amorphous carbon-rich nanowires [2, 14] and films [2, 12, 15–17], diamond [18–21], silicon [22–25], silicon dioxide [26–28], silicon carbide [29], silicon nitride [29], alumina [30], germanium

[31], gallium arsenide [32], titanium [33], chromium oxide [34], poly(methyl methacrylate) (PMMA) [12] and polyimide [35].

The applicability and wide scale adoption of EBIE is limited primarily by poor process control and reproducibility stemming from a limited understanding of the underlying science. Historically, nanofabrication hardware has been added to charged particle beam platforms originally designed for microscopy, microanalysis or ion beam sputtering. Consequently, studies and optimisation of the resulting chemical processes have been severely limited by inadequate control of residual contaminants, the state of the substrate surface, and the precursor pressure distribution at the substrate.

Despite the above problems, a number of groups have recently demonstrated that these individual issues can be resolved by improved vacuum system quality and enhanced control of the substrate surface [36], appropriate selection of precursor molecule species [37] and gas mixture composition [38], optimisation of beam chemistry process parameters [37, 39, 40], and the use of post-growth annealing and plasma treatments [41–43]. By building on these studies, methods are implemented in this work to improve EBIE's weaknesses as a nanofabrication technique. With improvements in the hardware used for EBIE (Chapters 2 and 7), and a greater understanding of the mechanisms of EBIE in carbon (Chapter 2, 3 and 4) and silicon (Chapter 7) based materials, EBIE is becoming an essential part of the nanofabrication toolkit.

1.2.2 Standard Model of EBIE

Continuum models of EBIE rate kinetics are based on equations for the rate of change of concentration of adsorbates at the substrate surface [1, 28, 44]:

$$\frac{\partial N_a}{\partial t} = \Lambda - k_0 N_a - \frac{\partial N_\alpha}{\partial t} + D_a \nabla^2 N_a, \tag{1.1}$$

where a and α signify precursor molecules and fragments, respectively, and N is number density at the surface. The equation is a sum of fluxes ($\mathrm{m}^{-2}\mathrm{s}^{-1}$) representing precursor molecule adsorption ($\Lambda = sF\Theta$), desorption ($k_0 N_a$), dissociation ($\frac{\partial N_\alpha}{\partial t}$), and diffusion

$(D_a \nabla^2 N_a)$ (F is the gas molecule flux incident onto the substrate, s is the sticking coefficient, Θ is surface coverage, k_0 is the desorption rate and D_a is the diffusion coefficient).

Existing models [1, 28, 44] assume that the adsorbate dissociation rate $\frac{\partial N_\alpha}{\partial t}$ is proportional to the the product of the electron flux f and N_a, and that the vertical etch rate $\frac{\partial z}{\partial t}$ is proportional to $\frac{\partial N_\alpha}{\partial t}$:

$$\frac{\partial N_\alpha}{\partial t} = \sigma_\alpha f N_a, \tag{1.2}$$

$$\frac{\partial z}{\partial t} = V_\gamma \frac{\partial N_\alpha}{\partial t}, \tag{1.3}$$

where σ_α is the cross-section for the generation of fragments α that volatilise the substrate and V_γ is the volume occupied by a single molecule removed from the substrate in the etch reaction. Models based on Equations 1.1 - 1.3 yield an etch rate (in molecules per second) that is first order overall, and with respect to N_a, and a rate coefficient k equal to $\sigma_\alpha f$. Multiple adsorbate species are accounted for by a rate equation such as Equations 1.1 and 1.2 for each precursor molecule [45] and precursor fragment [46] species present at the surface, respectively, and analogous equations for reaction products [44] that have significant residence times at the surface.

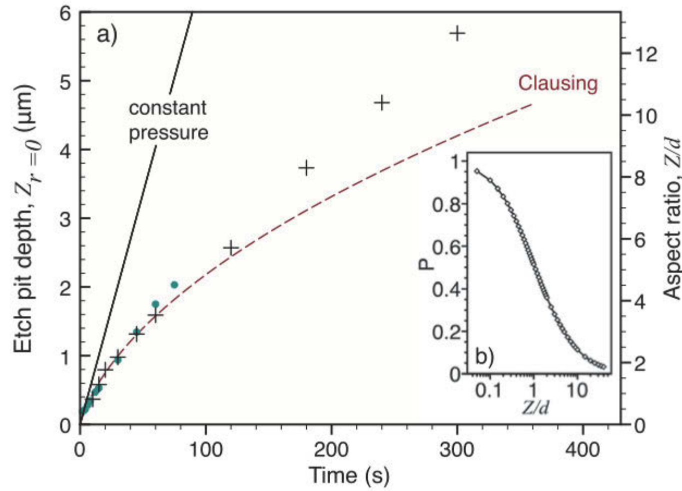

FIGURE 1.2: Etch pit depth at the beam axis (r=0) versus time simulated using the constant pressure and Clausing gas flow model, and observed experimentally in films of SiO_2 [28].

Solutions to Equations 1.1 - 1.3 predict an initial decrease in N_a that typically lasts $\sim 10^{-3}$ s, followed by constant, steady state etching [45]. The initial decrease is caused by adsorbate depletion under the beam by $\sigma_\alpha f N_a(t)$. Hence, $\frac{\partial N_\alpha}{\partial t}$ (and $\frac{\partial z}{\partial t}$) does not change with time, the model yields linear $z(t)$ profiles over the experimental time scale, and the effective cross-section σ_α governs the slope of $z(t)$. The models yield etch rates that are fixed or decrease due to precursor consumption in the etch reaction, and assume that the surface does not change with time (i.e., the fraction of surface sites that can be volatilised is constant). Variation from steady state etching has been observed previously where Clausing gas flow limits the replenishment of precursor molecules [28]. The Clausing model incorporates gas flow conductance of the cylindrical etch pit into the description of the gas molecule flux incident onto the substrate (F). Gas flow conductance is reduced during growth of the fixed diameter, cylindrical etch pit, resulting in a decrease in precursor concentration at the etch surface with time (Figure 1.2). Prior to the study of electron sensitive material in Chapter 3, no mechanisms were presented which affect the kinetics in a super-linear manner.

Studies of material-precursor interactions during electron beam processing have been performed to investigate phenomena such as activated chemisorption [46] and precursor dissociation by dissociative electron attachment [47, 48], however these are still limited to the analogous field of electron beam induced deposition (EBID). A key criticism of the standard EBIE model is the lack of material based properties in the description of the etch kinetics. A study of the re-dissociation of reaction products by the electron beam prior to desorption [44], shows the importance of the substrate material properties in the kinetics of EBIE. This is one of the few extensions of the standard EBIE model to account for chemical reactions at the substrate surface, and shows how quantitative measurements and modelling can be used to increase our understanding of EBIE reaction mechanisms. This work is extended in Chapter 7. Prior to this work, properties such as defect structure [49, 50], bond hybridisation [51] and anisotropic etching along crystal planes [52] were not accounted for in the model, most likely due to the lack of experimental evidence. As shown in Chapters 3 and 4, these properties significantly affect the etch kinetics and can be harnessed to fabricate complex surface geometries.

1.2.3 Silicon

Silicon is the basis for integrated circuit technology making it one of the most relevant materials to the semiconductor industry [26, 53] and new applications are constantly being explored in areas such as quantum information [54–56], nonlinear optical components [57], optical modulators [58], lasers [59], microelectromechanical sensors (MEMS) [60] and medicine [61]. Given the long history of silicon device fabrication a number of now routine fabrication techniques including wet etching [62, 63], reactive ion etching (RIE) [63, 64], low energy electron-enhanced etching (LE4) [65, 66], metal-assisted chemical etching [67], vapour phase etching [29, 62] and plasma etching [62–64, 68, 69] are available to erode silicon based material, each with their own strengths and weaknesses depending on the application. These techniques use masks produced by optical [70, 71] or electron beam lithography [72, 73] to pattern the desired structures. Non-mechanical, maskless techniques for erosion of silicon include ultrafast laser milling [74, 75], FIB milling [42, 76–78] and EBIE [1, 26].

Of the maskless techniques FIB milling is the most akin to EBIE, enabling nanoscale, direct-write removal of material. FIB milling proceeds via sputtering of substrate material by energetic ions [42]. Sputtering is always accompanied by ion implantation into the top layer of substrate material with the thickness dependent on the ion type, energy, incidence angle and crystal structure [77]. A range of ion types are used in FIB milling, with Ga^+, He^+, Ne^+ and Xe^+ ion source systems sold by the major manufacturers [77]. FIB milling is typically used for photolithographic mask repair, device modification, failure analysis, integrated circuit debugging, metrology, direct-write lithography and transmission electron microscope sample preparation [76, 79].

FIB milling rates and material quality can be improved by injecting a gaseous precursor into the vacuum system at the near-substrate region during milling [42]. The processes is analogous to EBIE and the material removal rate enhancement is linearly proportional to the number of surface atoms excited by the ion collision cascades [42]. Gaseous precursors such as XeF_2 and Cl_2 are used respectively to assist FIB milling of silicon. The dissociation of the precursor by the ion beam produces localised chemical etching at the substrate surface, increasing the etch rate [42]. Even in the absence of a gaseous precursor, the material

removal rate by FIB milling is orders of magnitude faster than EBIE. However, EBIE is increasingly being used where the surface damage induced by FIB milling is no longer acceptable to device performance such as in the repair of chromium photolithographic masks [80].

The most prominent and industrially applied EBIE precursor for silicon is XeF_2 [42]. Etching of silicon by XeF_2 is spontaneous at room temperature, and has been studied in detail [81]. The XeF_2 molecule physisorbs at temperatures below 450 K, and undergoes direct impact dissociation at higher temperatures on silicon and SiO_2 [82]. Below 450 K, the physisorbed XeF_2 molecule reacts with silicon to form intermediate SiF_2, and finally volatile SiF_4, which desorbs from the surface. In XeF_2-mediated EBIE, the electron beam merely accelerates the local etch rate [22, 26], with spontaneous etching resulting in roughening of the silicon surface unless preventative measures are taken [83]. These measures however, are sensitive to subsequent exposure to an electron beam (e.g. during electron imaging used to monitor EBIE). Surface reactions during XeF_2-mediated EBIE of SiO_2 have been studied to determine the effect of re-dissociation of etch products (e.g. SiF_2) on the etch kinetics [44]. These findings are extended in Chapter 7 where temperature and/or electron flux are varied to show how these parameters affect the characterisation of the rates and energy barriers that govern adsorption [46].

Precursors that do not etch silicon spontaneously have been demonstrated, including Cl_2 [23, 24] and SF_6 [25]. It has been shown that in the case of Cl_2, precursor replenishment takes place predominantly from the gas phase while surface diffusion only plays a minor role, and that the etching process is governed by the secondary electron flux. For SF_6-mediated EBIE, the influence of different EBIE parameters, such as the beam energy, electron beam flux and sample bias, have been investigated. However, Cl_2 and SF_6 have not found widespread use because SF_6 is highly inefficient and can result in the deposition of sulfur [84], and Cl_2 is highly corrosive, toxic and flammable.

The limited range of precursor-substrate combinations available for EBIE of silicon is noticeable compared to the range available in conventional plasma etching [68, 69]. This is because many of the precursors that yield radicals responsible for plasma etching have properties that are undesirable for EBIE. This limited scope of EBIE is exemplified by

precursors such as nitrogen trifluoride (NF_3) and tetrafluoromethane (CF_4). NF_3 is a common fluorine precursor used in laser [85] and plasma [86] induced etching of silicon and silicon carbide [87]. NF_3 satisfies most key requirements for EBIE: it has a large electron dissociation cross-section [88]; high vapour pressure; relatively low toxicity and broad material compatibility. In particular, NF_3 does not cause corrosion of components in electron microscope chambers, and does not etch most solids spontaneously, including silicon [89]. Despite these favourable characteristics, NF_3-mediated EBIE was previously thought not to be a viable process [90], likely a result of the poor surface coverage of NF_3 at room temperature. Standard theory of gas-mediated electron beam processing [1, 26, 28, 42, 44, 46, 91–94] predicts that the low NF_3 adsorption energies (on the order of 200 meV) give rise to very low etch rates at and near room temperature. In Chapter 7 substrate cooling temperature is introduced as a method to increase the surface coverage of weakly bound precursor molecules. The realisation of inert EBIE precursors such as NF_3 enables nanofabrication or editing of silicon-based and multielement structures where chemical treatments are detrimental to material quality. Inert precursors also allow fabrication to take place in a gaseous environment, as in environmental electron microscopy, where charging of specimens can be suppressed [95]. Injection of XeF_2 (and Cl_2) is limited to the conventional high vacuum capillary-style gas injection systems, as the precursor spontaneously reacts with microscope components and is a safety hazard.

With the capabilities realised by the NF_3-mediated EBIE process for erosion of silicon based materials, new applications for EBIE can be realised. In 2006, NASA's Stardust spacecraft delivered to Earth thousands of dust particles collected from the coma of comet 81P/Wild 2 for laboratory study [96] (Figure 1.3). Studying cometary material is critical for determining the origin and evolution of the solar system. Comets formed from presolar and early nebular matter at the outermost edges of the solar system [96], and are an archive of chemical and physical processes which occurred during the early evolution of planetary bodies [97]. These samples were the first opportunity to directly study cometary particles of known origin in the laboratory [98]. Unlike previous studies of interplanetary dust particles of unknown origin, these dust particles were likely shielded from damage by thermal, aqueous or radiative processes, therefore retaining their properties since early solar system formation [99].

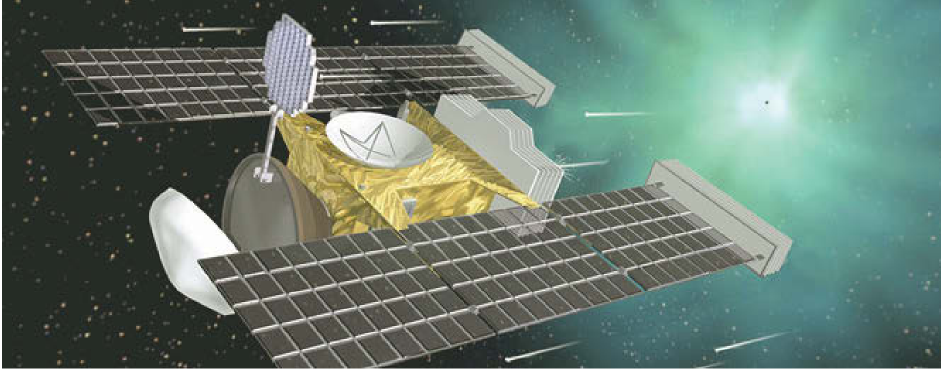

Figure 1.3: NASA's Stardust spacecraft, which collected comet and interstellar dust in 2004 and later delivered the tennis-racket shaped dust collectors to Earth via parachute. Image courtesy of NASA.

Stardust cometary samples were collected in a low-density, nano-porous silica aerogel [100], arguably making them the most technically challenging of all of NASA's extraterrestrial collections to study. Cometary impact particles are fine-grained and fragile, so they disintegrate on impact with the aerogel. The largest and most robust particles penetrate deep into the aerogel, but the smallest fragments are distributed non-uniformly along the lengths of carrot-shaped impact tracks [101]. Prior to analysis of the particle, removal from the collection medium is generally required. Particles 3 μm and larger can be extracted essentially free of silica aerogel using silicon micro-tweezers and precision (200 nm) motorised micromanipulators [102]. The process is monitored optically, and requires > 50,000 discrete automatised motions over many hours to extract the particle from the aerogel. Further optimisation of this process using borosilicate glass micro-needles enables the preparation of a silica aerogel keystone containing a complete impact event [103] (Figure 1.4). The keystone can then be analysed, or further processed by flattening, mounting on micro-forks and/or sectioning. Particles and fragments as small as 1 μm across can be extracted by sectioning a keystone embedded in epoxy by ultramicrotomy [104]. Techniques for extracting sub-1 μm particles and fragments are however, limited. Furthermore, directly observing the removal of small particles is not possible with light-based techniques.

Direct-write, beam-driven nanoscale etching techniques are ideal for this application, particularly if in situ nanoscopic analytical techniques are used for real-time imaging and

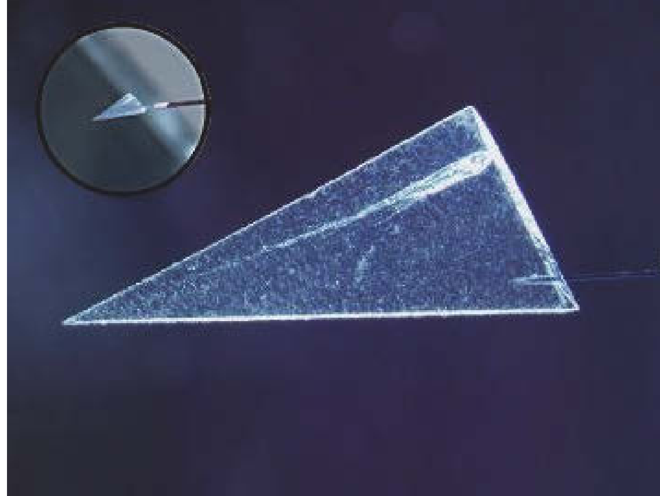

FIGURE 1.4: A particle and its track cut out of the collector material, into a wedge-shaped slice keystone. A specialised silicon pickle fork is then used to remove the keystone from the remaining aerogel for further analysis. Image courtesy of NASA/JPL-Caltech.

rapid analysis of the particles. Conventional FIB milling is unsuitable for particle extraction due to indiscriminate etching and gallium ion staining of the embedded particles, and severe charging of the insulating aerogels during ion beam irradiation [105]. Material incompatibility with XeF_2 and Cl_2 was previously limiting the implementation of EBIE for this application. With the development of the inert, NF_3-mediated process the application of EBIE to extraction of microparticles from silica aerogel material can be revisited (Chapter 8).

1.2.4 Carbon

Carbon based materials including graphene [106–109], nanotubes [110, 111], diamond [112–114] and diamond films [111, 115, 116] are increasingly being utilised for their electronic, optical, quantum and biological properties. Many of the fabrication methods utilised in the processing of silicon devices such as wet etching [117], vapour phase [118], RIE [51, 119–124] and plasma etching [49, 125] can be readily applied to carbon based materials. Some of the processes, however, are not ideal for the processing of carbon based materials due to defect generation or chemical incompatibility. This is particularly evident in direct-write techniques such as FIB milling where ion bombardment or high power laser ablation are utilised, resulting in damage and material re-deposition artifacts [126–131].

EBIE has been investigated in a wide range of carbon materials including diamond [18–21], graphene [5, 8], carbon nanotubes [10–12], amorphous hydrocarbon nanowires [14] and carbonaceous films [12, 16] using a range of precursors including air [19], H_2O [10, 12, 16, 19], O_2 [8, 10, 11, 19, 20], N_2 [5, 10, 19], NH_3 [14] and H_2 [10, 21]. These studies have used EBIE to produce functional structures, demonstrate EBIE resolution (see Figure 1.5), and illustrated the affects of primary electron energy and electron beam scan rate on etch rate kinetics. The reaction mechanisms giving rise to EBIE of carbon based material are, however, are not well understood (as is illustrated in Chapters 2, 3 and 4 of this thesis). For EBIE to become a viable nanofabrication technique the reaction mechanisms need to be characterised, so that predictive models of etching and robust process recipes can be constructed.

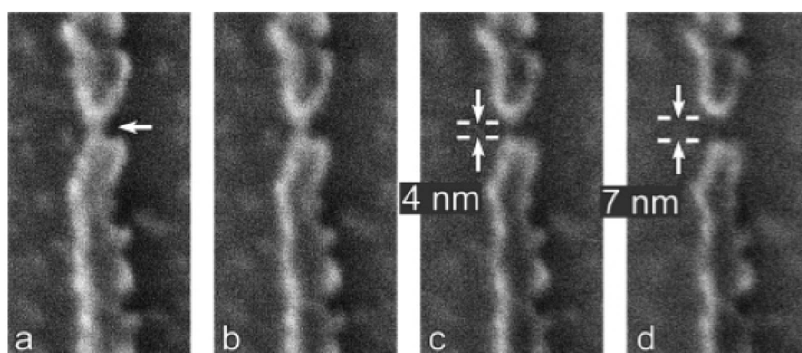

FIGURE 1.5: Demonstration of EBIE resolution. Four consecutive frames of a H_2O-mediated EBIE process used to slim a carbonaceous nanowire and to produce the gap shown in (c, d) [2].

Studies in the EBIE of carbon report removal of material during injection of gaseous precursors into the vacuum chamber, however, many studies do not take into account the contribution of residual H_2O on etch kinetics which can increase during gas injection [132]. For example, reports of etching of graphene [5] and diamond [19] by N_2-mediated EBIE are unexpected given the chemistry of the system. While the production of CN_2 has been demonstrated with activated nitrogen at elevated temperatures [133], it has not been identified under the conditions used for electron beam induced removal of carbon. The previous results of etching with N_2 [5, 19] can be explained by electron induced dissociation of H_2O. Given the uncertainty in the literature with respect to the contribution of H_2O in the removal of carbon material during electron irradiation, the study in Chapter 2

was performed. The study into the presence of residual contaminants such as H_2O and hydrocarbons during EBIE processing is also important as they can have severe negative consequences, including a reduction in material quality, and uncertainty in measurements and discrepancies across different instruments [41].

A previous study of H_2O-mediated EBIE of chemical vapour deposition (CVD) grown poly-crystalline diamond observed an important reaction mechanism. It was shown that material was preferentially removed at crystal grain boundaries. This was ascribed to graphitic inclusions at these sites [18] and is consistent with preferential etching at grain boundaries in RIE of CVD diamond [51]. It is also well known that the surface volatilisation efficiency of carbon is a strong function of local defect structure [49, 50] and bond hybridisation [51]. The effect of anisotropic etch rates between different carbon atom configurations is compounded by the fact that many materials are electron sensitive, and the bulk and surface structure can be altered by the electron beam during EBIE. It is well established that materials such as ultra nano-crystalline diamond (UNCD) are susceptible to radiation damage, and can be restructured by both high and low energy electrons [131, 134–137]. As electron restructuring can occur at the energies used in EBIE and defects can give rise to changes in the volatilisation probability of carbonaceous material, these mechanisms were studied and incorporated into EBIE models in Chapter 3.

While many materials are sensitive to the electron beam, the application of EBIE to erosion of material is advantageous as it eliminates ion related damage to the crystal structure. A material particularly sensitive to changes in it's crystal structure is diamond [138]. For centuries, processing of diamond was considered to be extremely challenging due to its extraordinary strength and chemical resistance. However, diamond is now used in applications across numerous areas of science due to its unique combination of optical, electronic, chemical and thermal properties [112]. Most notably, the nitrogen-vacancy luminescence centre (NV) (Figure 1.6) has been employed as a spin qubit, enabling the use of diamond as a platform for next generation sensing, nanophotonic and quantum devices [139–145]. Identified applications include high-energy particle detectors, ultraviolet LEDs, biolabeling of individual cells, super-resolution optical microscopy, and quantum computation and cryptography [113]. These promising applications are, however, overshadowed by challenges in fabrication arising from its extraordinary hardness and chemical resistance.

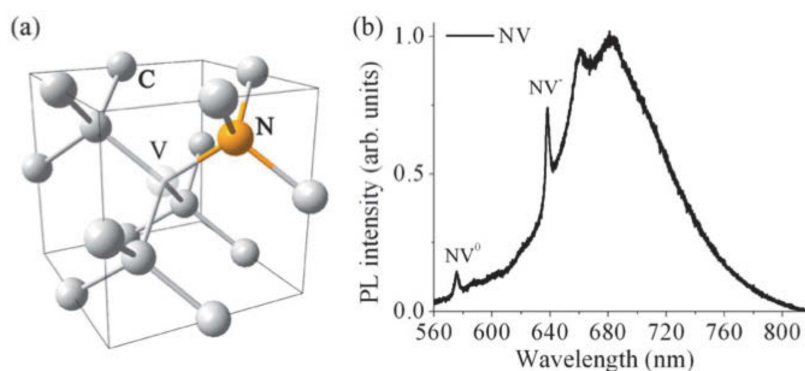

Figure 1.6: The NV centre. a) Crystallographic model of the NV centre in diamond, consisting of a substitutional nitrogen (yellow) adjacent to a vacancy (V). b) Photoluminescence (PL) spectrum showing the zero phonon lines (ZPL) of the neutral (575 nm) and the negatively charged (637 nm) NV centre with phonon side bands at the lower energy side of each ZPL [113].

When compared to conventional semiconductors such as silicon and gallium arsenide, fabrication and editing of optoelectronic grade diamond nanostructures is extremely limited. Prior to the study in Chapter 5, direct-write, deterministic patterning of optical structures in diamond had not been demonstrated in the absence of severe surface damage caused by ion implantation and redeposition of non-volatile, sputtered or ablated material. During FIB milling, momentum transfer from the ions to the target atoms above a critical dose [146, 147] induces amorphisation of diamond within the ion interaction volume. For Ga^+ based FIB milling this amorphisation damage profile is on the order of 46 nm at an ion energy of 30 keV, and the damage layer is heavily stained by implanted gallium ions [147]. It has been shown that gallium staining can be partly removed by ex situ hydrogen plasma and chemical etch treatments [148, 149], however as shown in Chapter 6 this limits resolution and in general it is desirable to utilise in situ techniques such as EBIE, which are typically free from material degradation caused by material incompatibilities with aggressive chemical treatments.

EBIE of single-crystal diamond has been reported in the presence of a number of gases including H_2O, O_2, N_2 and H_2 [19, 21]. Electron irradiation was shown not to affect the bulk crystal structure in these experiments. While these initial experiments were positive, no work has been done since to use EBIE in the fabrication of functional diamond structures, likely due to the low etch rate and diamond's electrically insulating nature. With

the current interest in diamond and new technologies such as the magnetic immersion lens gaseous secondary electron detector [150] enabling high resolution editing of insulating materials such as diamond in gaseous environments [151], EBIE is now a viable technique for the fabrication and nanoscale editing of diamond structures (as shown in Chapter 5). While slow compared to FIB milling, EBIE could be used for modification of existing devices and prototyping of small scale diamond devices. With more development, processing speed could be increased by new gaseous precursors or multiple electron beam systems [152]. Another approach demonstrated in Chapter 6 is to use EBIE as a final polishing step, where large regions are removed by light or inert ion such as He^+, Ne^+, Xe^+ and O^+ [77] and the damage layer removed by EBIE. This approach is currently not viable in diamond processed by Ga^+ FIB milling as there is no EBIE method to remove gallium and carbon material simultaneously. The reported erosion of GaAs by XeF_2-mediated EBIE [32] cannot be reproduced in our laboratory to remove Ga material. Erosion of GaAs using this method can be explained by preferential removal of arsenic and formation of non-volatile GaF_3 [153]. Erosion of gallium by gaseous Cl_2 above room temperature [154] is not viable for diamond as oxidation during EBIE processing of surrounding carbon material suppresses the reaction.

1.3 Experimental Techniques

1.3.1 Environmental Reaction Cell

This work utilised a unique environmental reaction cell (eCell) (Figure 1.7) [14] in Chapters 2 and 3. The eCell enables environmental scanning electron microscope (ESEM) operation in reactive gaseous environments. Specifically, it alleviates process contamination and reproducibility problems, chemical incompatibilities between reactive gases and materials found in ESEM tools, and safety issues inherent to ESEM. These characteristics enable experiments that are incompatible with conventional SEM and ESEM systems. Unlike high vacuum capillary-style gas injection [1], the eCell provides a constant precursor pressure across the entire substrate surface that can be measured using a conventional

pressure gauge. Charge stabilisation of insulating substrates and imaging during operation is realised by a gaseous secondary electron detector [151].

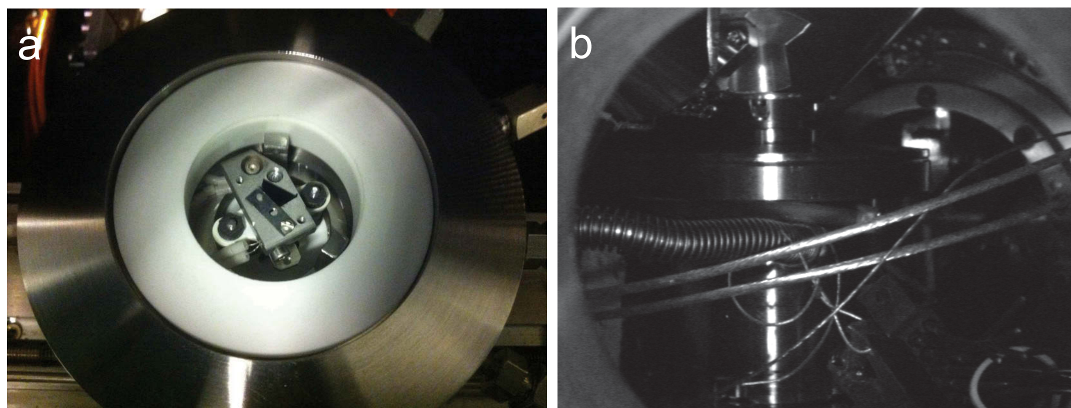

FIGURE 1.7: a) Photograph of the internals of the eCell body. b) Charge-coupled device (CCD) image of an environmental reaction cell installed in the chamber of an FEI Nova NanoSEM 600.

The eCell is comprised of a stainless steel body connected to the SEM stage and a lid attached to the base of the electron column pole piece. The eCell body houses a sample holder, gaseous electron detector [155], Faraday cup and a high temperature ceramic heater (Figure 1.8). The lid contains a pressure limiting aperture (PLA) and the SEM chamber area surrounding the eCell is pumped to high vacuum with a turbo molecular pump (TMP) ensuring a positive flow out of the eCell during operation in the transition flow regime. High vacuum feed-throughs for gas delivery, gaseous electron detector, thermocouple temperature probes and sample current measurement are incorporated into the eCell body located in the SEM specimen chamber. Precursor flow is controlled using a pressure-feedback system comprised of a needle valve or a mass flow controller (MFC), and a capacitance manometer located in the same vacuum space as the eCell.

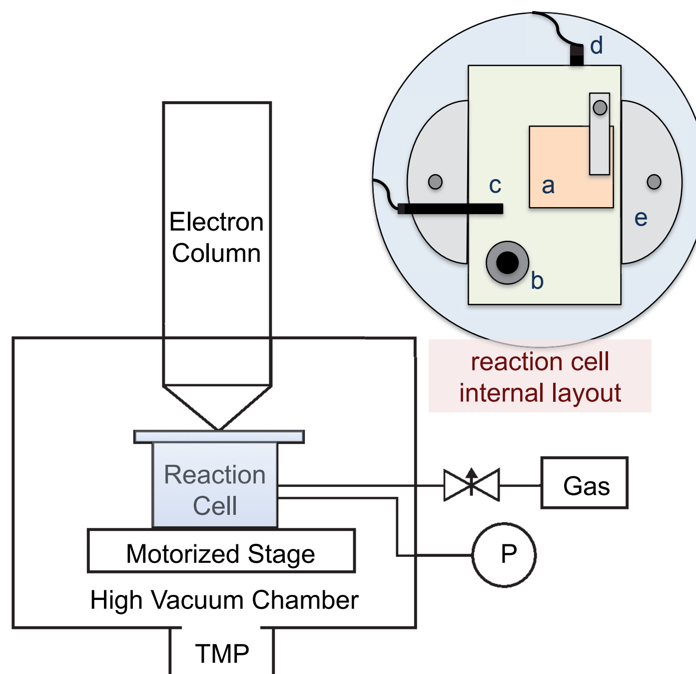

FIGURE 1.8: eCell configured for operation in a conventional differentially pumped SEM. eCell internal layout: a) sample, b) Faraday cup, c) electron detector, d) thermocouple and e) heater [14].

1.3.2 Material Characterisation Techniques

Characterisation of material pre and post processing by EBIE was performed by a number of routine characterisation techniques:

- Scanning electron microscopy [156] was used to image substrates (Chapters 2 - 8). Depending on the application, images are formed by detecting secondary (electron energy < 50 eV) or backscattered (electron energy > 50 eV) electrons. Secondary electron imaging was used as a general imaging tool to observe changes in the surface topography. Secondary electrons are detected in high vacuum using an Everhart-Thornley detector. In gaseous environments, secondary electrons were detected using a gas ionisation cascade detector [95] or a magnetic immersion lens gaseous secondary electron detector [150] (known commercially as an FEI Company Helix detector). Backscattered electron imaging was used to detect sub-surface particles in low density silica aerogel (Chapter 8). Backscattered electrons were detected using a solid state

backscattered electron detector. The detector is capable of detecting backscattered electrons in high vacuum and gaseous environments.

- Atomic force microscopy [157] was used to determine the surface topography of substrates (Chapters 2, 3, 5, 6 and 7). A Digital Instruments Dimension 3100 atomic force microscope (AFM) was used to measure the topography and the data analysed using the software package Gwyddion [158]. Height profiles were used to calculate the depth of pits produced by EBIE. Measurements are traceable to a physical standard which was used to calibrate the instrument.

- Energy-dispersive x-ray spectroscopy (EDS) [156] was used to determine the near-surface elemental composition of silica aerogel and microparticles after EBIE processing (Chapter 8). A high spectral resolution cryogenic microcalorimeter was used as the x-ray detector. The microcalorimeter has superior energy resolution to conventional silicon drift detectors ($\sim$ 6 eV instead of $\sim$ 130 eV at 6 keV x-ray energy), providing greater element discrimination [159]. Elemental concentration was calculated using the atomic number, absorbance and fluorescence (ZAF) correction scheme with standards [156, 160].

- Raman spectroscopy [161] was used to probe the structure of carbonaceous material including diamond [162] (Chapters 5 and 6). Raman measurements were performed using a Renishaw inVia Raman microscope with a 633 nm excitation laser. The peak position and full width at half maximum (FWHM) of areas processed by EBIE was compared to pristine material to determine bond configuration changes in the material. Diamond material was analysed for the appearance of graphitic inclusions or lattice disorder [138, 163].

- Photoluminescence (PL) spectroscopy [164] was used to probe point defects in diamond (Chapters 5 and 6). Here specifically it was used to investigate the NV, silicon-vacancy and GR1 colour-centres in diamond [113]. PL spectra were recorded using a custom built confocal microscope with a 532 nm excitation laser [165]. The PL spectra of pristine and processed material were compared to determine the effect

of electron or ion irradiation on material properties. Electron and ion induced processes can result in changes to the PL intensity from point defects due to changes in the local material structure such as introduction of vacancies or graphitisation.

- Cathodoluminescence (CL) spectroscopy [166] was used to probe point defects in diamond (Chapter 6). Specifically, constant power CL depth profiling [167, 168] was used to investigate ion induced damage in diamond by measurement of nitrogen-vacancy (NV) colour-centre emission [169]. CL measurements were performed at room temperature using an FEI Quanta 200 SEM equipped with a Gatan parabolic CL collection mirror. The mirror is positioned above the sample and directs the emitted light to a Hamamatsu CCD to record the intensity and wavelength of the emitted light.

1.3.3 Material-Particle Interaction Simulation

- The Monte Carlo software CASINO [167, 170, 171] was used to determine electron penetration range, energy deposition profiles and/or backscattered electron coefficients in UNCD (Chapter 3), diamond (Chapters 5 and 6) and silica aerogel (Chapter 8). A DOS based version of the program [167, 170] was used to calculate the range of electrons in diamond as a function of primary electron beam energy. This version was also used to calculate the energy deposition profile in UNCD and diamond. This information was used in defect generation (Chapter 3) and CL depth profile (Chapter 6) calculations. Software version 3.2.0.4 was used to determine the backscattered electron coefficient of silica aerogel under various conditions (Chapter 8). The backscattered electron coefficient was determined by dividing the total number of electrons escaping the top plane of the silica aerogel by the total number of primary electrons used in the simulation.

- Stopping and Range of Ions in Matter (SRIM) software [172] (2013 version) was used to determine the depth distribution of oxygen ions implanted in diamond (Chapter 6). The software uses simple binary approximation Monte Carlo simulations of interactions between the ion and atoms in the material. Specifically, SRIM was used to determine O ion implantation depth distributions for ion energies $\leq$ 30 keV. SRIM

is only able to model amorphous materials, therefore effects such as ion channelling are not reflected in ion depth distribution when using single crystal material [173]. This limitation was taken into consideration during analysis of ion implantation data.

1.4 Description of Chapters

Chapter 1, includes the aims of the thesis and background information. The standard continuum EBIE model is presented to introduce the reaction kinetics of EBIE. A review of experimental EBIE studies is given with a focus on carbon and silicon. An introduction to the application of EBIE for processing diamond and Stardust cometary samples is included within the review. The research methodology section describes the eCell and standard analytical techniques used during this work to process and analyse samples.

Chapter 2, describes the influence of gas phase impurities on EBIE of carbon. Etching of graphene and diamond by low energy electrons previously attributed to mechanisms including atomic displacements caused by knock-on, electron beam heating, sputtering by ionised gas molecules, and chemical etching driven by a number of gases that include N_2, are shown to be caused by electron beam induced dissociation of residual contaminants present in the vacuum system. A system for reducing residual H_2O during EBIE is presented, improving reproducibility of EBIE experiments and providing insights into the etch mechanisms. This chapter has been prepared in a format for publication.

Chapter 3, reports a new mechanism that limits the rate of EBIE. Typically, the etch rate is assumed to scale directly with the precursor adsorbate dissociation rate. It is shown that this is a special case, and that the rate can instead be limited by the concentration of active sites at the surface. Novel etch kinetics are expected if surface sites are activated during EBIE, and observed experimentally using the electron sensitive material UNCD. Significant portions of this chapter were copied verbatim from the peer reviewed article "*Dynamic surface site activation: A rate limiting process in electron beam induced etching*, **A. A. Martin**, M. R. Phillips and M. Toth, ACS Appl. Mater. Interfaces, 5 (16), p.

8002 8007, 2013" (Impact Factor: 5.900).

Chapter 4, presents a new method for simultaneously producing and observing self-ordered topographic patterns in single crystal material. Chemical etching is realised by EBIE and the evolving structure observed by secondary electron imaging. Kinetics and mechanisms of EBIE of single crystal diamond are inferred by interpretation of the dynamics of pattern formation. The patterns formed during etching are a result of anisotropic etching along crystal planes, which varies with precursor chemistry. The general EBIE model is extended to incorporate the observed etch rate anisotropy. This chapter has been prepared in a format for publication.

Chapter 5, demonstrates a method to fabricate diamond nanostructures in single crystal diamond with $\sim$ 100 nm nanometer resolution using EBIE. H_2O-mediated EBIE is employed for maskless editing of inclined diamond surfaces. Editing of multiple inclined facets is nearly impossible by mask-based processing techniques, including electron- and photo- lithography. Fabricated structures, including pillar cavities and diamond nanostructures retain their optical properties and exhibit bright florescence. The realised structures demonstrate the potential of EBIE for the fabrication of optically active structures in diamond. Significant portions of this chapter were copied verbatim from the peer reviewed article "*Subtractive 3D printing of optically active diamond structures*, **A. A. Martin**, M. Toth and I. Aharonovich, Sci. Rep., 4, 5022, 2014" (Impact Factor: 5.078).

Chapter 6, demonstrates maskless fabrication of diamond structures using a focused oxygen ion beam. Material quality of fabricated structures is assessed by Raman and luminescence analysis. It is shown that the damage layer generated by oxygen ions can be removed non-intrusively by EBIE. Significant portions of this chapter were copied verbatim from the peer reviewed article "*Maskless milling of diamond by a focused oxygen ion beam*, **A. A. Martin**, S. Randolph, A. Botman, M. Toth and I. Aharonovich, Sci. Rep., 5, 8958, 2015" (Impact Factor: 5.078).

Chapter 7, reports the use of substrate cryogenic cooling to enable efficient EBIE in systems where etching is negligible at elevated substrate temperatures due to weak physisorption of precursor molecules to the substrate. It is demonstrated using NF_3 precursor gas, and Si, SiC, SiO_2, and Si_3N_4 substrates. This technique enables the use of NF_3 for high resolution EBIE in the absence of artifacts caused by delocalised spontaneous etching of the substrates, as in the case of XeF_2-mediated EBIE of silicon. Significant portions of this chapter were copied verbatim from the peer reviewed article "*Cryogenic electron beam induced chemical etching*, **A. A. Martin** and M. Toth, ACS Appl. Mater. Interfaces, 6 (21) p. 18457 - 18460, 2014" (Impact Factor: 5.900).

Chapter 8, describes the use of in situ SEM techniques, including EBIE to identify, extract and analyse the elemental composition of particles analogous to those collected by NASAs Stardust mission. This chapter has been prepared in a format for publication.

Chapter 9, includes a summary of the thesis and suggestions for future work in the field of EBIE.

Chapter 2

Electron Beam Induced Etching of Carbon

2.1 Abstract

Nanopatterning of graphene and diamond by low energy ($\leq$ 30 keV) electrons has previously been attributed to mechanisms that include atomic displacements caused by knock-on, electron beam heating, sputtering by ionised gas molecules, and chemical etching driven by a number of gases that include N_2. Here we show that a number of these mechanisms are insignificant, and that the observed behaviour can instead be explained by chemical etching caused by electron beam induced dissociation of residual contaminants present in the vacuum systems used in such experiments.

2.2 Introduction

Nanopatterning of graphene [174] and diamond [114, 175] has attracted interest due the unique electrical [107] and optical [113] properties of these materials. They are however, sensitive to doping levels and defects in the crystal structure which can be affected by the processing method [148, 176]. Gas-mediated electron beam induced etching [1, 177] (EBIE) is increasingly being used for rapid prototyping of functional structures in graphene [8]

and diamond [178] as it eliminates damage to the material produced by masking and ion implantation.

In the EBIE process, gaseous precursor molecules are delivered to the substrate surface where they are dissociated by an electron beam, producing reactive fragments which give rise to volatilisation of the substrate. EBIE has been used to etch numerous carbon materials including graphene [5–9], carbon nanotubes [10–13], diamond [19–21, 178], ultra nano-crystalline diamond [94] (UNCD), and amorphous carbon-rich nanowires [2, 14] and films [2, 12, 15–17]. At low electron beam energies ($\leq$ 30 keV), where atomic displacements by knock-on collisions between electrons and carbon are negligible [7, 131, 134], the removal of carbon is typically attributed to chemical etching (i.e. volatilisation of carbon). The etching is generally ascribed to chemical pathways that involve O^*, H^* or OH^* radicals produced by electron induced dissociation of H_2O [7, 10, 12, 16, 17, 19, 94, 178], O_2 [6–8, 10, 11, 13, 15, 19, 20], NH_3 [14] or H_2 [10, 21] precursor molecules adsorbed to the surface of the etched material.

Electron beam nanopatterning of carbon materials has, surprisingly, also been demonstrated using N_2 as the precursor gas. Specifically, it has been reported that electron beam induced removal of carbon from graphene [5] and diamond [19] can be accelerated by introducing N_2 into the vacuum chamber. These observations were attributed to sputtering [19] and chemical etching [5] of carbon caused by nitrogen ions. Here we demonstrate that the injection of not only N_2, but also Ar can indeed be used to increase the removal rate of carbon irradiated by an electron beam. However, we show that this increase can be eliminated using an appropriate experimental configuration, and can not be explained by chemical etching caused by these gases, nor by sputtering caused by nitrogen or argon ions. Instead, it is ascribed to EBIE caused by residual H_2O molecules whose flow rate to the etched material is increased by the injection of N_2 and Ar into the vacuum chamber. We also propose that the combination of H_2O and hydrocarbon contaminants can, in principle, explain unexpected behaviour that has been observed recently in graphene and attributed to mechanisms that include electron beam induced heating and atomic displacements caused by knock-on (at electron beam energies as low as 5 keV) [9].

2.3 Results and Discussion

We start by showing that low energy electron beams can be used to remove carbon from a range of materials in a high vacuum (3×10^{-4} Pa) environment. Electron beam processing was performed at room temperature using a field emission gun scanning electron microscope (SEM) described elsewhere [14]. Hydrocarbon contamination in the vacuum system was minimised by plasma cleaning [179] the SEM chamber using an XEI Scientific Evactron for $\sim$ 12 hours (RF power = 13 W, O_2 pressure = 40 Pa) prior to loading substrates into the system, and heating substrates in situ using the conditioning procedures detailed in the Supporting Information Section 2.5.1. Figure 2.1 shows regions of graphene and lacey carbon, each of which was removed by scanning a 10 keV, 1.3 nA focused beam over an area of 200 $\times$ 200 nm for 30 and 20 minutes, respectively. Figure 2.2a and Table 2.1 show the depths of pits made in UNCD in high vacuum (and in Ar and N_2 environments, under a number of conditions detailed below). These results illustrate that the injection of a precursor gas into a high vacuum SEM is not required for the removal of carbon, which we attribute to H_2O-mediated EBIE. H_2O is the most abundant species present in this vacuum regime [180] and is known to give rise to etching under electron irradiation [181].

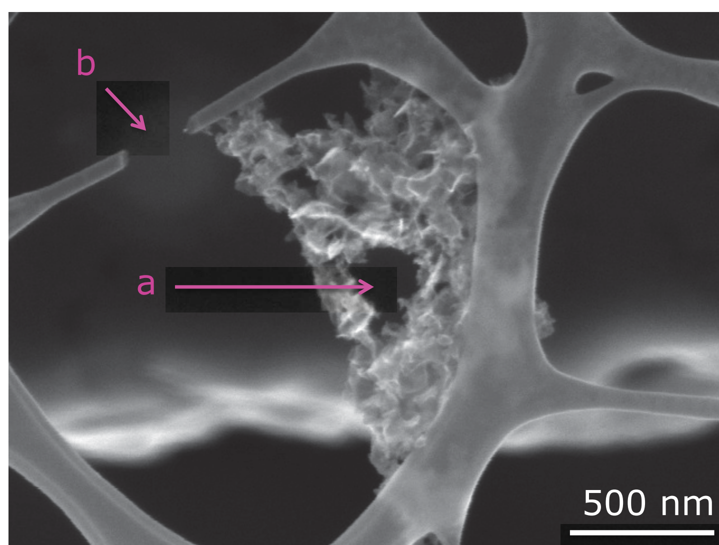

FIGURE 2.1: Electron beam induced removal of carbon from (a) graphene and (b) lacy carbon.

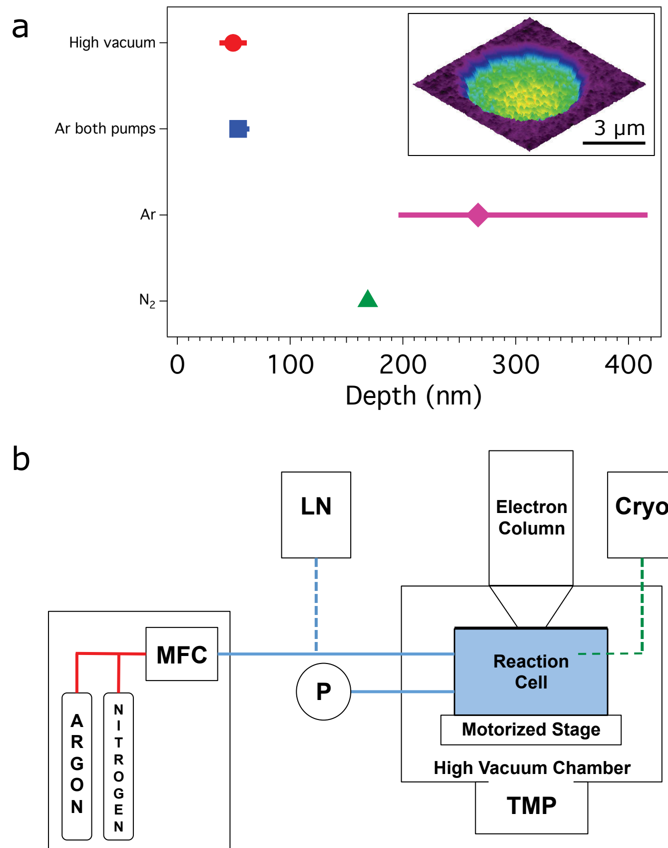

FIGURE 2.2: a) Depths of pits produced in UNCD using an electron beam under the environmental conditions listed in Table 2.1: (●) high vacuum, (▲) N_2, (♦) Ar, and (■) Ar with both cryogenic pumps cooled. Markers and lines indicate the average and the range of pit depths produced under each set of conditions, respectively. *Inset:* AFM image of a typical etch pit. b) Simplified schematic of the system including the gas delivery system, eCell, and LN cryogenic pumps connected to the gas delivery line and eCell.

Environment	Pressure (Pa)	Gas line pump (K)	eCell pump (K)	Depth (nm)
High vacuum	3×10^{-4}	298	298	62, 37
Ar	13	298	298	417
Ar	13	~ 77	298	234, 196, 220
Ar	13	~ 77	~ 218	48, 64, 50, 54
N_2	13	~ 77	298	169

TABLE 2.1: Depths of pits produced in UNCD using an electron beam under a number of environmental conditions. The two cryogenic pumps are shown in Figure 2.2b.

To confirm the role of H_2O in the observed carbon removal process, a set of pits (summarised in Figure 2.2a and Table 2.1) were fabricated in high vacuum, and at N_2 and Ar pressures of 13 Pa. The experiments were performed using a UNCD substrate, a 20 keV

stationary top-hat electron beam with a diameter of ~ 6.6 μm, and the vacuum system configuration based on the environmental reaction cell (eCell) shown in Figure 2.2b (for a complete list of experimental parameters and a description of the eCell, see the Supporting Information Section 2.5.1, 2.5.2, 2.5.3 and 2.5.4). UNCD was used because H_2O-mediated EBIE of UNCD has been characterised previously over a range of beam energies (5 to 20 keV), and the etch kinetics are well understood [94]. The broad, stationary beam with a top-hat electron flux profile was used (instead of a highly focused, scanned Gaussian beam) because this configuration improves reproducibility and quantitative analysis of pits made by an electron beam [94, 182]. The eCell shown in Figure 2.2b was used (instead of a conventional cappilary-style gas injection system [42]) because it improves the degree of control over the vacuum chamber environment [14, 46], and enables EBIE experiments to be performed with a high degree of reproducibility [94]. Two liquid nitrogen (LN) cold traps were installed, one on a gas delivery line and one inside the eCell (see Figure 2.2b) to enable optional cryogenic pumping of gaseous contaminants present in the vacuum system.

First, we compare pits made in UNCD with both cryogenic pumps disabled. The depths of pits made in high vacuum and an Ar environment were 37 - 62 nm and 417 nm, respectively, as shown in Table 2.1 (for a full description of the experiment, see the Supporting Information Section 2.5.1). The variation observed in high vacuum depends on the procedure used to reach the irradiation conditions. If the UNCD is irradiated immediately after pumping down to a pressure of 3×10^{-4} Pa, the pit depth (62 nm) is greater than when the system is pumped for an extended period of time prior to irradiation (37 nm). This is consistent with a decrease in the concentration of residual H_2O in the vacuum system. The increase in carbon removal rate caused by Ar can, in principle, be explained by residual H_2O contaminants since the injection of gases into a vacuum chamber can increase the partial pressure of H_2O [132]. To test this hypothesis, the cryogenic pump installed on the gas delivery line shown in Figure 2.2b was cooled from 298 K to ~ 77 K while Ar was flowing into the vacuum chamber, yielding pit depths in the range of 196 - 234 nm. The reduction in pit depth (from 417 nm to 196 - 234 nm) caused by cooling of the cryogenic pump is consistent with the proposal that the increase in carbon removal rate observed

upon the introduction of Ar is caused by the delivery of H_2O impurities to the UNCD substrate.

Next, the cryogenic pump installed inside the eCell shown in Figure 2.2b was cooled from 298 K to ∼ 218 K. After conditioning (see the Supporting Information Section 2.5.1), a series of 4 electron irradiations in an Ar environment produced pit depths in the range of 48 - 64 nm. These results are comparable to the depths of 37 - 62 nm produced in high vacuum, and show that cryogenic pumping can be used to eliminate the enhancement in carbon removal rate caused by the injection of an inert gas into a high vacuum process chamber.

To compare pits made in N_2 and Ar environments, the system was conditioned (see the Supporting Information Section 2.5.1) with the gas delivery line cryogenic pump cooled to ∼ 77 K. Electron irradiation in an N_2 environment produced a pit depth of 169 nm. Hence, the results summarised in Table 2.1 illustrate that the introduction of either N_2 or Ar to a high vacuum chamber can cause a significant increase in the carbon removal rate. However, given that N_2 does not increase the removal rate relative to Ar, the mechanism of chemical etching by nitrogen ions (leading to the production of volatile cyanogen (CN_2) molecules) proposed by Fox et. al. [5] is likely insignificant. We note that the production of CN_2 has been demonstrated with activated nitrogen at elevated temperatures [133], but not under the conditions used for electron beam induced removal of carbon.

The above results, summarised in Figure 2.2a and Table 2.1, can not be explained by chemical etching caused by the gases injected into the vacuum system [5] or sputtering [19] caused by nitrogen or argon ions. They are, however, consistent with: (i) EBIE caused by H_2O contaminants present in the high vacuum chamber, and (ii) an increase in the H_2O delivery rate to the sample by N_2 and Ar gases. The difference between pit depths produced whilst cooling one (196 - 234 nm) and both (48 - 64 nm) cryogenic pumps in an Ar environment indicates that most of the extra H_2O evolves from gas delivery plumbing and vacuum system walls exposed to the flowing Ar gas.

Next, we show that under the conditions used to perform the above experiments in high vacuum, N_2 and Ar environments, the surface of the etched material is covered predominantly by H_2O molecules. In the absence of electron irradiation, the concentration of

surface-adsorbed molecules (N) is found by solving [1]:

$$\frac{dN}{dt} = sF(1-\Theta) - N/\tau, \tag{2.1}$$

where $sF(1-\Theta)$ is the flux of gas molecules adsorbing to the surface, N/τ is the desorption flux, s is the sticking coefficient, F is the gas molecule flux incident onto the surface ($F = P/\sqrt{2\pi mkT_g}$), P is pressure, m is the gas molecule mass, k is Boltzmann's constant, T_g is gas temperature, Θ is the adsorbate coverage (which is typically limited to one monolayer by the Langmuir isotherm, $\Theta = AN$), A is the area of a single surface site and τ is the adsorbate residence time:

$$\tau = \tau_0 e^{E/kT}, \tag{2.2}$$

where τ_0 is the reciprocal desorption attempt frequency, E is the activation energy for thermal desorption and T is the temperature of the surface. Equation 2.1 has the steady state solution:

$$N_\infty = \frac{sF}{sFA + 1/\tau}, \tag{2.3}$$

which, at 298 K, yields a H_2O concentration of 1.5×10^{10} cm^{-2} at a pressure of 3×10^{-4} Pa, N_2 concentration of 9.4×10^9 cm^{-2} at 13 Pa and Ar concentration of 4.7×10^9 cm^{-2} at 13 Pa (a complete list of parameters used in Equation 2.3 is provided in the Supporting Information Section 2.5.5). The dependencies of these concentrations on pressure is plotted in Figure 2.3. The plot shows that, over the range of pressures encountered in high vacuum EBIE systems, the concentration of H_2O adsorbates is always greater than or similar to that of N_2 or Ar. This is caused by the significantly higher adsorption energy of H_2O on all surfaces. Given the rate of EBIE scales with the concentration of surface-adsorbed precursor molecules [1, 177], the above results show that residual H_2O adsorbates must be considered when interpreting electron irradiation experiments performed in high vacuum systems, as well as changes in the supply rate of H_2O caused by the injection of gases into an EBIE chamber.

Finally, we note that many medium and long chain hydrocarbons have high adsorption energies on common surfaces [1, 183], and the role of residual hydrocarbon contaminants must not be overlooked when interpreting electron beam irradiation experiments. Hydrocarbon impurities are common in high vacuum systems and give rise to electron beam

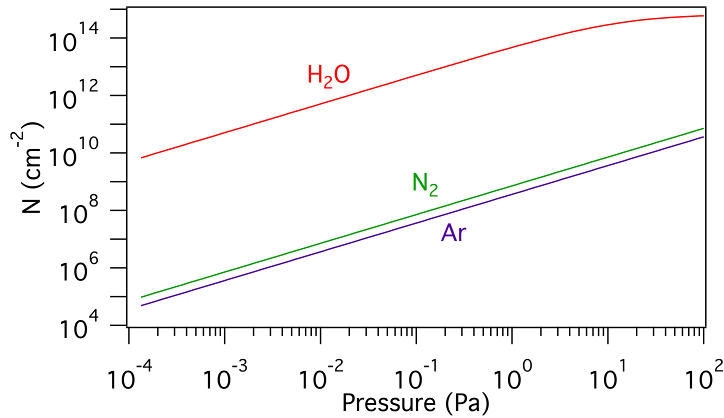

FIGURE 2.3: Concentration (N) of H_2O, N_2 and Ar adsorbates calculated as a function of pressure.

induced deposition (EBID) of amorphous carbonaceous materials [181]. In the present work, this EBID process was minimised by using the conditioning procedures described above and in the Supporting Information. However, when such procedures are not employed, and standard electron microscopes are used for H_2O-mediated EBIE, deposition of amorphous carbon-rich material competes with etching [14, 16, 45]. The material deposited by EBID is simultaneously etched and restructured (damaged) by the electron beam. The restructuring makes the material non-uniform, generating nano-clusters with locally modified etch rates [2]. The net effect of such simultaneous EBID, restructuring and EBIE is a complex dependence of etch rate on parameters such as the electron beam energy, current, flux and scan rate [2, 16]. In particular, the etch rate can increase with increasing scan rate, and the restructuring rate can increase with decreasing electron beam energy. These dependencies provide an alternate explanation to behaviour that has recently been ascribed to knock-on displacements of atoms from graphene (by electrons with energies as low as 5 keV) and electron beam induced heating of graphene [9].

2.4 Conclusions

In conclusion, the injection of inert gases into a high vacuum chamber was shown to increase the removal rate of carbon from UNCD by a low energy electron beam. It is

caused by an increase in the concentration of residual H_2O adsorbates at the sample, and can be eliminated using an appropriate vacuum system configuration.

2.5 Supporting Information

2.5.1 Conditioning Procedures

Ar, no cryogenic pump: The SEM was pumped to high vacuum, and a UNCD substrate was baked to remove residual contaminants from the substrate, eCell and gas delivery system. First, the substrate was baked at 573 K for 4 hours (eCell open) and then for 2 hours in a 27 Pa Ar environment (eCell closed). After baking, the substrate was cooled to 298 K, the eCell was opened and the chamber was left in high vacuum (3×10^{-4} Pa) for 40 hours. Ar was then introduced into a closed eCell to pressure of 13 Pa. The LN cryogenic pump on the gas delivery system was not cooled to reduce residual H_2O entering the eCell. The UNCD substrate was irradiated by the electron beam for 2 hours, producing a pit with a depth of 417 nm.

High vacuum: Following from the above irradiation in Ar, gas flow was stopped, eCell opened and system evacuated to 3×10^{-4} Pa. The UNCD was then irradiated for 2 hours producing a pit depth of 37 nm. The system was then vented and evacuated to 3×10^{-4} Pa. The UNCD substrate was irradiated for 2 hours, producing a pit depth of 62 nm.

Ar with gas delivery line cryogenic pump cooled: A UNCD substrate was baked at 573 K for 6 hours in a 13 Pa Ar environment. After baking, the substrate was cooled to 298 K and the LN cryogenic pump on the gas delivery system was cooled to 77 K. Under these conditions a series of 3, 2 hour electron irradiations on UNCD produced pit depths of 234, 196 and 220 nm.

Ar with both cryogenic pumps cooled: A UNCD substrate was baked at 573 K for 6 hours in a 13 Pa Ar environment. After baking, the substrate was cooled to 298 K with the Ar pressure maintained at 13 Pa. The gas delivery line cryogenic pump was cooled

to 77 K and eCell cryogenic pump was cooled to $\sim$ 218 K. Under these conditions a series of 4, 2 hour electron irradiations on UNCD produced etch pit depths of 48, 64, 50 and 54 nm.

N_2 with gas delivery line cryogenic pump cooled: Following from the "*Ar with gas delivery line cryogenic pump cooled*" irradiations, the eCell was opened and the chamber evacuated to 3×10^{-4} Pa for 19 hours. The eCell was then closed and N_2 flowed through the eCell at 6.6 sccm (133 Pa) for 50 minutes to purge the gas delivery system prior to lowering the nitrogen pressure to 13 Pa. The UNCD substrate was irradiated for 2 hours producing a pit depth of 169 nm.

2.5.2 Materials

- Ultra nano-crystalline diamond (UNCD) on a silicon substrate; thickness = 1.7 μm, grain size = 2 – 5 nm, average roughness = 10 nm, MTI corporation.
- N_2; 99.999% , $\leq$ 5 ppm H_2O, $\leq$ 3 ppm O_2, Scientific and Technical Gases Ltd.
- Ar 99.998+%, $\leq$ 3 ppm H_2O, $\leq$ 3 ppm O_2, Sigma-Aldrich.

2.5.3 Experimental Parameters

Cylindrical pits in UNCD were fabricated by irradiation for 2 hours with a 20 keV, 14.6 nA stationary electron beam, under-focused to a diameter of $\sim$ 6.6μm to produce a top-hat, radially symmetrical flux profile of 2.7×10^{17} cm^{-2} s^{-1}. All electron irradiations performed on UNCD used identical electron beam parameters. Etch pits were imaged by a SEM and using the tapping mode of a Digital Instruments Dimension 3100 atomic force microscope (AFM). AFM data was analysed using the software package Gwyddion [158].

2.5.4 Environmental Reaction Cell

The eCell [14] is located inside the SEM vacuum chamber which is pumped by a turbo molecular pump. The cell lid contains a pressure limiting aperture (PLA) and is suspended

from the SEM pole piece. The rest of the cell body is secured to the SEM sample translation stage which can be used to open or close the cell by lowering or raising the cell body:

- In the 'open' configuration, the cell interior is exposed to the high vacuum SEM chamber and is pumped actively by the turbo molecular pump.
- In the 'closed' configuration, the cell interior is isolated from the high vacuum SEM chamber, and the cell is filled with the precursor gas. Gas flow is always out of the cell, into the column (through the PLA) and into the SEM chamber (through any leaks present in the seal between the cell lid and the cell body). The SEM chamber is always pumped by the turbo molecular pump and acts as a vacuum jacket around the cell that prevents the flow of contaminants to the sample.

In the closed configuration, the gas pressure inside the eCell is uniform over the entire sample which is located on a heater used in the conditioning procedures described below. Gas delivery to the eCell is controlled by a mass flow controller and the pressure is measured by a capacitance manometer. The gas delivery system is constructed from stainless steel tubing with metal gasket face seals. The gas delivery lines are heated to 323 K during evacuation from atmosphere to $\sim 10^{-3}$ Pa to remove residual contaminants.

2.5.5 Modelling Parameters

- Common: $T = T_g = 298$ K; $\tau_0 = 10^{-13}$ s (appropriate for small molecules [184]).
- H_2O [185, 186]: P = 3×10^{-4} Pa, $E = 482$ meV, $A = 14.8$ Å^2.
- Ar [187, 188]: P = 13 Pa, $E = 188$ meV, $A = 13.8$ Å^2.
- N_2 [187, 189]: P = 13 Pa, $E = 192$ meV, $A = 16.2$ Å^2.

Author Contributions

Aiden Martin and Milos Toth designed the project. Aiden Martin performed the experiments. Aiden Martin and Milos Toth performed the numerical modelling. Aiden Martin,

Geoffrey McCredie and Milos Toth designed and implemented the experimental equipment. Aiden Martin and Milos Toth analysed the data and contributed to the writing of the manuscript.

Chapter 3

Dynamic Surface Site Activation: A Rate Limiting Process in Electron Beam Induced Etching

3.1 Abstract

We report a new mechanism that limits the rate of gas-mediated electron beam induced etching (EBIE). Typically, the etch rate is assumed to scale directly with the precursor adsorbate dissociation rate. Here we show that this is a special case, and that the rate can instead be limited by the concentration of active sites at the surface. Novel etch kinetics are expected if surface sites are activated during EBIE, and observed experimentally using the electron sensitive material ultra nano-crystalline diamond (UNCD). In practice, etch kinetics are of interest because they affect resolution, throughput, proximity effects and the topography of nanostructures and nanostructured devices fabricated by EBIE.

3.2 Introduction

EBIE is a direct-write nanolithography technique used to modify surfaces at nano- and micro-scales [1, 26, 42]. EBIE proceeds through chemical reactions induced by electron

irradiation of a solid substrate exposed to a precursor gas. Surface-adsorbed precursor molecules such as H_2O are dissociated by electrons, generating fragments (e.g., O^* and OH^*) [4] that react with a substrate (e.g., C) to produce volatile species (e.g., CO and CO_2) that desorb and are removed by a pumping system, thus giving rise to localised chemical dry etching in the vicinity of an electron beam (see Figure 3.1). Precursors such as XeF_2, Cl_2, ClF_3, NH_3, O_2 and H_2O can be used to etch a wide range of materials including graphene, carbon nanotubes, amorphous carbon [2, 6, 12–15, 17, 190], diamond [18, 19, 21] and a variety metals, semiconductors and insulators [1, 26, 42]. Nanometer resolution is attainable [1] and $\sim$ 4 nm has been demonstrated in H_2O-mediated EBIE of carbon nanowires on electrically insulating, bulk quartz substrates [2]. The technique is analogous to gas-assisted focused ion beam (FIB) milling [1, 3]. However, EBIE is a chemical process that does not involve sputtering or ion implantation.

EBIE resolution and the time-evolution of structures fabricated by EBIE are affected by the electron flux profile at the substrate surface, and by the precursor adsorbate supply and dissociation rates [17, 42, 191]. The flux profile is governed by the diameter and shape of the electron beam, and the spatial distribution of electrons emitted from the substrate. It governs EBIE resolution in the limit of zero depletion (i.e., in the so-called 'reaction rate limited' etch regime) where the etch rate scales linearly with electron flux. However, adsorbate depletion makes the etch rate sub-linear with electron flux, which in turn serves to alter (usually decrease) resolution because the etch efficiency increases with electron flux which typically decreases with distance away from the electron beam axis. Consequently, much effort has gone into the development of simulators for predictive modelling of EBIE and the related technique of gas-mediated electron beam induced deposition (EBID) [1, 26, 28, 42, 44, 46, 92, 93, 191]. The models come in a number of varieties, but all are based on assumptions contained in rate equations of the form:

$$\frac{\partial N_a}{\partial t} = \Lambda - k_0 N_a - \frac{\partial N_\alpha}{\partial t} + D_a \nabla^2 N_a, \tag{3.1}$$

where a and α signify surface-adsorbed precursor molecules (e.g., H_2O) and fragments (e.g., O^*), respectively, $\frac{\partial N_a}{\partial t}$ is the rate of change of concentration of precursor adsorbates at each point on the surface, expressed as a sum of fluxes (m^{-2} s^{-1}) representing adsorption

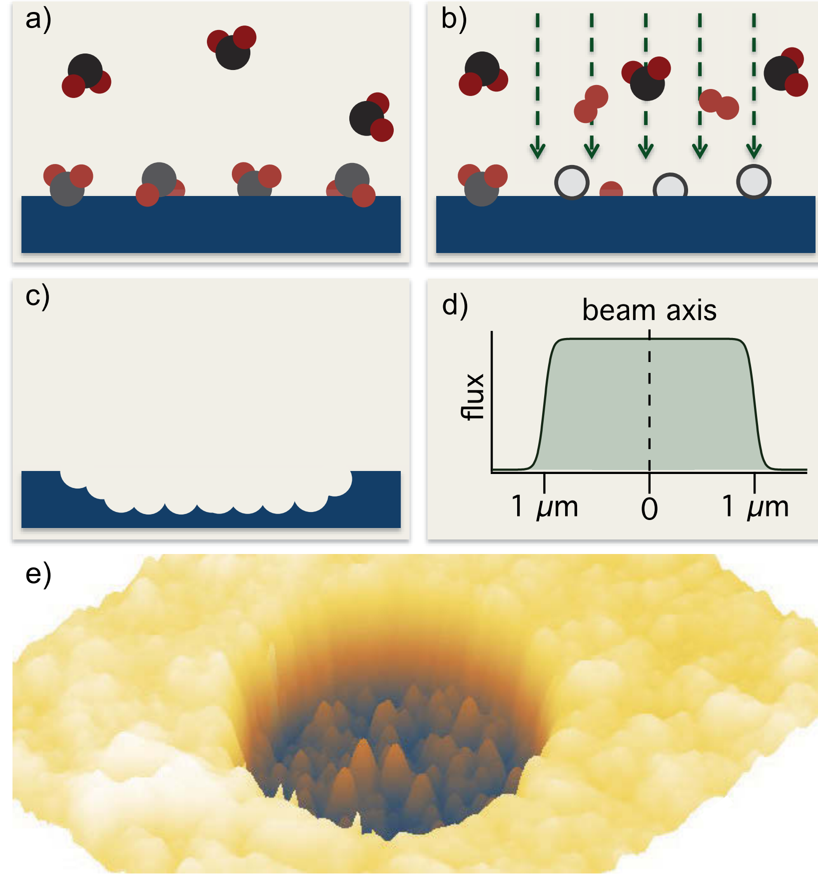

FIGURE 3.1: Simplified schematic of H_2O-mediated EBIE of carbon: (a) H_2O adsorption and surface diffusion, (b) generation of O^* fragments by incident and emitted electrons, and (c) etching caused by C volatilisation by O^* adsorbates. Also shown is (d) a 2 μm wide electron beam with a top-hat flux profile, and (e) an AFM image of a pit etched in UNCD using a stationary top-hat beam (diameter = 2 μm, depth (z_d) = 175 ± 22 nm).

$(\Lambda = sF(1-\Theta))$, desorption $(k_0 N_a)$, electron induced dissociation $(\frac{\partial N_\alpha}{\partial t})$ and diffusion $(D_a \nabla^2 N_a)$. N is number density at the surface, F is the gas molecule flux incident onto the substrate, s is the sticking coefficient, Θ is H_2O surface coverage (which is typically limited to 1 ML by the Langmuir isotherm, $\Theta = A_a N_a$), A_a is the area of a single surface site, k_0 is the desorption rate and D_a is the diffusion coefficient. The etch rate is given by:

$$\frac{\partial N_\alpha}{\partial t} = \sigma_\alpha f N_a, \tag{3.2}$$

$$\frac{\partial z_d}{\partial t} = V_\gamma \frac{\partial N_\alpha}{\partial t}, \tag{3.3}$$

where f is electron flux, σ_α is the effective cross-section for the generation of fragments

that volatilise the substrate [1], z_d is the depth of an etch pit such as the one in Figure 3.1e, $\frac{\partial z_d}{\partial t}$ is the vertical etch rate and V_γ is the volume of a single molecule (e.g., C) removed from the substrate in the etch reaction.

Equations 3.1, 3.2 and 3.3, referred to from here on as 'model #1', are representative of standard EBIE models [1, 26, 28, 42, 44], which are based on the assumption that the etch rate is proportional to the adsorbate dissociation rate (i.e., Equations 3.2 and 3.3). A shortcoming of these models is that they neglect the possibility that volatilisation (i.e., etching) may occur only at sites that are chemically 'active', such as defects, and that the active site concentration may change during EBIE. This simplification is clearly inappropriate for beam sensitive materials which are altered by the electron beam used for EBIE.

Electron beam damage (or 'restructuring') is a common phenomenon encountered in materials such as carbon whose defect structure and bond hybridisation can be altered by electron irradiation [131, 134–137, 192–194]. It is well known (from plasma and thermal etching studies) that the bond hybridisation [51] and defect structure [49, 50, 195] of carbon affect the surface volatilisation efficiency. It is therefore reasonable to expect the EBIE efficiency of such materials to change with time as an electron beam creates surface defects during etching. To verify this hypothesis, we generalise model #1 to account for active sites at the surface, and dynamic surface site activation occurring during EBIE ('model #2'). Subsequently, model #2 is adapted to the specific case of site activation caused by electron beam damage of the substrate ('model #3') which is shown to be in excellent agreement with EBIE experiments performed using the electron sensitive material UNCD.

[1]The values of σ_α and σ_a used in the models represent cross-sections weighed by the overlap between the corresponding energy dependent cross-section and energy spectra of electrons incident onto and emitted from the substrate [1].

3.3 Methods

3.3.1 Modelling

Models #1 - #3 were implemented using numerical methods described elsewhere [1, 191]. The parameters f and F were measured directly, s was fixed at unity, $k_0 \approx 10^{13}$ s^{-1} [185], $E_a = 0.48$ eV, $V_\gamma \approx 5.70$ Å^3 (calculated using a density of 3.5 g cm^{-2}), and the area of a H_2O molecule $\sim$ 14.8 Å^2 [186]. All experiments were performed under conditions where adsorbate depletion is negligible. The parameter D was therefore set to zero [1, 46]. Calculated $N_a(t)$ profiles confirmed that the extent of depletion was negligible (($<$ 1%)) under all conditions used in the present study (i.e., $N_a[t \rightarrow \infty]/N_a[t = 0] \approx 1$). Hydrophilic and hydrophobic surface were treated identically in the etch model since adsorbate depletion was negligible in both cases (i.e., surface hydrophobicity affects only the etching of the first monolayer of UNCD).

3.3.2 Experimental

EBIE was performed at room temperature using a FEI Nova NanoSEM variable pressure [95] scanning electron microscope (SEM) equipped with an environmental reaction cell [14]. The substrates were 1.7 μm films of UNCD grown on silicon by hot filament chemical vapor deposition (HFCVD) at 953 K (grain size = 2 – 5 nm, average roughness = 10 nm) [196]. Samples were annealed in situ for six hours at 573 K under flowing H_2O vapor to desorb residual hydrocarbon adsorbates prior to performing EBIE at 300 K using 13.6 Pa of H_2O as the precursor gas. Cylindrical etch pits were fabricated as a function of time using a 20 keV, 3.4 nA, stationary electron beam under-focused to a diameter of $\sim$ 1.9 μm to produce a top-hat flux profile [28] (see Figure 3.1). Additional pits were produced using a beam diameter of $\sim$ 1.0 μm, beam energies of 5 and 10 keV and currents of 2.3 and 3.3 nA, respectively (Figure 3.4). All pits were imaged ex situ using the tapping mode of a Digital Instruments Dimension 3100 atomic force microscope (AFM), and analysed using the software package Gwyddion [158]. As-grown, H-terminated UNCD was hydrophobic, with a water contact angle θ_c of $\sim$ 85°. Hydrophilic UNCD ($\theta_c \sim$ 8°, measured in air after samples were removed from the SEM) was produced by oxygen plasma processing

[197, 198] performed in situ [199] for 2.5 hours, using a XEI Scientific Evactron installed on the SEM used for EBIE (RF power = 13 W, O_2 pressure = 40 Pa). Error bars in Figures 3.2 and 3.4 account for measurement uncertainty and are dominated by the effects of surface roughness on AFM image analysis.

3.4 Results and Discussion

3.4.1 Surface Site Activation

The case of active sites on a passive surface can be incorporated in model #1 by multiplying Equation 3.2 by A_sN_s, where N_s and A_s are the concentration and area of an active site, respectively:

$$\frac{\partial N_\alpha}{\partial t} = \sigma_a f N_a A_s N_s. \tag{3.4}$$

If N_s changes with time, as in the case of cumulative radiation damage occurring during EBIE, then:

$$\frac{\partial N_s}{\partial t} = C(1 - A_s N_s), \tag{3.5}$$

where C is the surface site activation flux ($m^{-2}s^{-1}$) and $(1-A_sN_s)$ limits the concentration of active sites to one monolayer. A_sN_s is the fraction of sites that are chemically active and can be volatilised by the fragments α, and $(1 - A_sN_s)$ is the corresponding fraction of α which are generated by the electron beam but do not contribute to etching. These fragments are assumed to leave the substrate through desorption (e.g., O(a) $\rightarrow$ O(g), and O(a) + O(a) $\rightarrow$ O_2(g)). Consequently, σ_a is the true adsorbate dissociation cross-section, rather than the 'effective' reaction cross-section σ_α used in Equation 3.2, which can be redefined as:

$$\sigma_\alpha \equiv \sigma_a A_s N_s. \tag{3.6}$$

We note, however, that the above definition of an effective cross-section is less meaningful than Equation 3.4 since N_s can change with time, whereas EBIE models are normally based on scattering cross-sections which depend only on the species of the adsorbate a, and the substrate surface. Hence, we define model #2 by Equations 3.1, 3.3, 3.4 and 3.5, and use Equation 3.6 merely to illustrate a shortcoming of standard EBIE models.

A consequence of Equation 3.5 that is experimentally verifiable and unique to model #2 is that the etch rate can increase with time during EBIE. Below, we demonstrate such an increase by H_2O-mediated EBIE of the electron sensitive material UNCD. The observed behavior can not be explained by standard EBIE models. It reveals a novel EBIE regime that is rate limited by a growing concentration of active sites, and is distinct from the electron flux and precursor mass transport limited regimes [1, 26, 28, 42, 200] documented in the literature.

3.4.2 EBIE of UNCD

Figure 3.2 shows plots of etch pit depth versus time measured from hydrophobic and hydrophilic UNCD. The initial vertical etch rate ($\frac{\partial z_d}{\partial t}$) is negligible and increases in both cases over the entire time scale (60 to 1440 s) probed by the experiments. Figure 3.2a also shows a datapoint from an etch process that was performed for 8 minutes, interrupted for 15 minutes and resumed for 7 minutes. The resulting depth is the same as that of an uninterrupted 15 minute etch process, showing that the change in etch rate is not reversible over the experimental time scale. The etch rate per unit electron flux was the same in all cases and did not change with small changes in beam diameter. From these results we can conclude that residual hydrocarbons [14, 16, 45], hydrophobicity, variations in adsorbate concentration and beam heating are not primary causes of the observed super-linear $z_d(t)$ profiles, and that adsorbate depletion [1, 26, 28, 42] was negligible during EBIE (i.e., the rate was not limited by mass transport of precursor molecules into the etched region of the substrate).

Conventional EBIE models (i.e., model #1) can not reproduce the measured super-linear $z_d(t)$ profiles seen in Figure 3.2. The models predict an initial decrease in N_a that typically lasts $\sim 10^{-3}$ s [2], followed by constant, steady state etching over the time scale of a typical etch pit fabrication process ($\sim 10^1$ to 10^3 s) [3]. That is, model #1 predicts $z_d(t)$ profiles

[2] The initial decrease corresponds to the transition from initial ($N_a[t=0]$) to steady state ($N_a[t \rightarrow \infty]$) at the start of an etch process. It is caused by adsorbate consumption in the etch reaction [1], and was negligible under the conditions used here (i.e., $N_a[t \rightarrow \infty]/N_a[t=0] \approx 1$).

[3] An additional decrease in etch rate with time has been reported in the case of high aspect ratio pits and mass transport limited EBIE [28]. It is caused by a decrease in the conductance of a growing etch pit during EBIE, and can not explain the super-linear $z_d(t)$ profiles reported here.

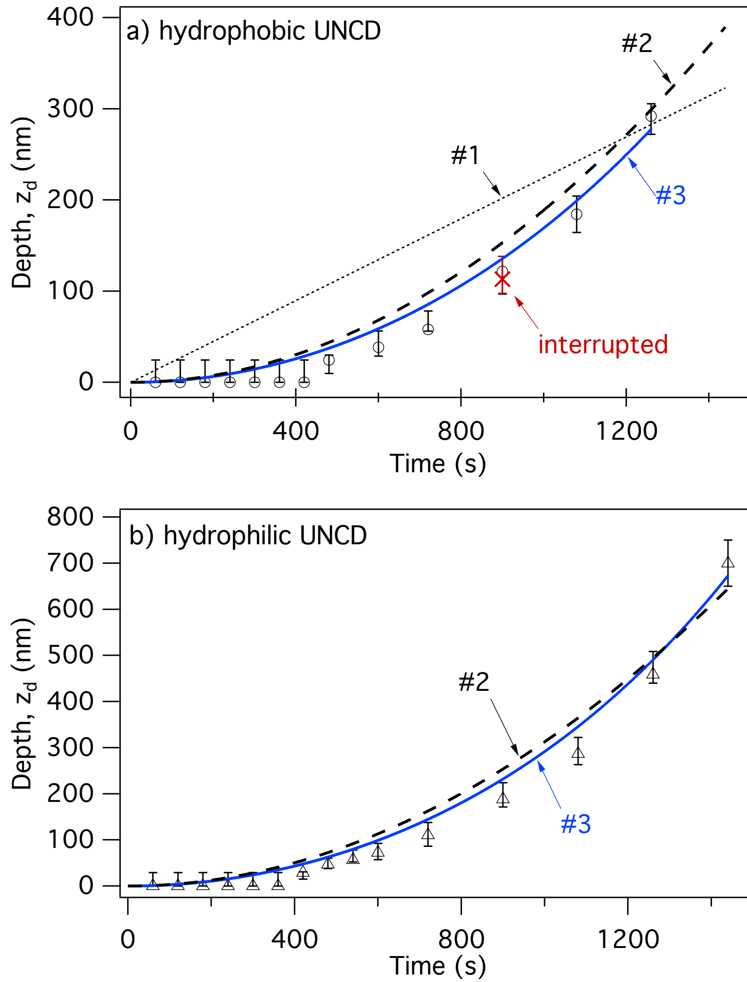

FIGURE 3.2: Etch pit depth (z_d) versus time (t) measured from (a) hydrophobic (○, beam diameter = 2 μm) and (b) hydrophilic (△, beam diameter = 1.8 μm) UNCD. Also shown is a datapoint [×] from a process that was interrupted for 15 minutes, and curves calculated using models #1, #2 and #3 (σ_α = 0.2 Å^2, σ_a = 2.8 Å^2). The difference in vertical etch rate between (a) and (b) is caused by the difference in electron beam diameter (the etch rate per unit electron flux is the same in both cases).

such as the one shown in Figure 3.2a, which are linear over the experimental time scale, and have a slope given by σ_α.

The measured data are, however, qualitatively consistent with model #2. This is illustrated in Figure 3.2 by curves obtained by treating σ_a and C as fitting parameters which determine the amplitude and curvature of the calculated $z_d(t)$ profiles. In both cases (i.e., hydrophobic and hydrophilic UNCD), best fit was obtained by setting σ_a to 2.8 Å^2 and C/f to 6×10^{-7} (active sites per electron injected into the substrate).

The etch behavior predicted by model #2 is in reasonable agreement with experiment. However, the model is based on the simplifying assumption that C does not change with time during etching. This assumption is incorrect for the case of damage produced by an electron beam because the electrons have a maximum penetration range R_e in the substrate (shown in Figure 3.3), and defects are generated at different rates throughout the electron-solid interaction volume. Hence, in the following, we develop 'model #3' which accounts for both the depth and the time dependence of the defect generation rate in the UNCD substrate, and for the fact that the etched surface recedes during EBIE.

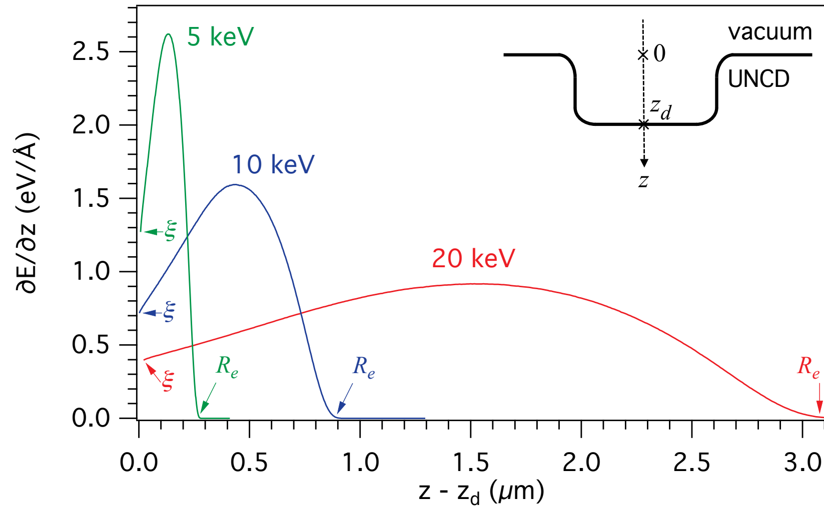

FIGURE 3.3: Electron energy deposition profile, $\frac{\partial E}{\partial z}$, calculated for UNCD using electron energies E_0 of 5, 10 and 20 keV (R_e = maximum electron energy penetration range, $\xi = \frac{\partial E}{\partial z}$ in the limit $[t \to 0]$) *Inset:* Schematic illustration of an etch pit and the co-ordinate system used in model #3.

3.4.3 Generation of Chemically Active Defects During EBIE

Electron induced defect generation is initiated through two general mechanisms: (i) knock-on caused by momentum transfer from electrons to nuclei, and (ii) bond breaking, ionization and excitation caused by electron-electron scattering [7, 131, 131, 134–137, 192–194]. The latter dominate at low electron energies (such as that used here), and the electron-electron scattering rate is approximately proportional to the total electron energy density [167, 192, 193, 201], $\frac{\partial E}{\partial V}$ (eV m^{-3}), deposited by the beam into each point (x, y, z) in the solid. However, in the present case of a broad, top-hat, stationary electron beam (Figure

3.1d), $\frac{\partial E}{\partial V}$ is approximately constant at each value of z (i.e., across the etch pit, in the plane of the substrate surface). We therefore ignore proximity effects at the etch pit periphery, and approximate the energy deposition profile with $\frac{\partial E}{\partial z}$, the energy deposited into the substrate per unit distance per electron (eV m^{-1}). The deposited energy varies with depth as shown in Figure 3.3 for electron beam energies of 5, 10 and 20 keV, and is assumed to be independent of x and y within the diameter of each etch pit (it was calculated for UNCD using standard Monte Carlo models [167, 170] of electron-solid interactions).

Hence, local defect generation at each point (x, y, z) within the electron-solid interaction volume can be described by:

$$\frac{\partial K}{\partial t} = n \frac{\partial E}{\partial z} f \left(1 - V_s K\right), \tag{3.7}$$

where K the local defect concentration (m^{-3}) which is a function of z and t, $\frac{\partial K}{\partial t}$ is defect generation flux (defects m^{-3} s^{-1}), and n is the number of defects generated per unit energy deposited into the substrate (eV^{-1}). That is, $n\frac{\partial E}{\partial z}$ is the number of defects generated in the solid per unit energy deposited into the substrate, and V_s is the volume of a single defect (and corresponds to A_s).

We can now complete model #3 by incorporating the expression $K(z, t)$ into model #2 by redefining N_s as:

$$N_s = \int_{z_d}^{z_d + z_\gamma} K dz, \tag{3.8}$$

where z_γ is the thickness of one monolayer of the substrate (and corresponds to V_γ in Equations 3.3 and 3.7). Figure 3.2 shows the best fit to experiment obtained using model #3, defined by Equations 3.1, 3.3, 3.4, 3.7 and 3.8. The model input parameters were those used in model #2, the 20 keV $\frac{\partial E}{\partial z}$ profile shown in Figure 3.3, and the coordinate system shown in the inset of Figure 3.3. The fitting parameter n was set to 1.35 MeV^{-1} (i.e., 135 defects per 100 MeV deposited into the substrate). The resulting $z_d(t)$ profile is in better agreement with experiment than model #2 because $\frac{\partial E}{\partial z}$ increases with z throughout the maximum etch pit depth probed by the experiments (i.e., 292 and 700 nm in the case of hydrophobic and hydrophilic UNCD, as seen in Figure 3.2a and b, respectively) [4].

[4] Based on model #3, a steady state (whereby $\frac{\partial N_s}{\partial t} = 0$ at the etch pit/vacuum interface) will be reached if the sample thickness and the etch pit depth are greater than the electron penetration range.

We note that the value of σ_α used in model #1 is much lower than that of σ_a used in models #2 and #3 [5] ($\sigma_\alpha = 0.2$ Å^2 and $\sigma_a = 2.8$ Å^2). This difference is expected since σ_α accounts only for the dissociation of fragments that lead to etching, as defined by Equation 3.6.

To verify the validity of model #3, we performed an additional experiment in which we analysed the etch rate at a number of electron beam energies, E_0. Figure 3.3 shows $\frac{\partial E}{\partial z}$ profiles calculated for E_0 = 20, 10 and 5 keV. The curves illustrate that, at the surface $[z \to 0]$, $\frac{\partial E}{\partial z}$ increases as E_0 is reduced from 20 to 5 keV. Hence, based on model #3, the initial EBIE rate, $\frac{\partial z_d}{\partial t}$, should scale accordingly since it is directly proportional to $\frac{\partial E}{\partial z}[z \to 0]$. To test this prediction, we measured the etch onset time, t_e, which we defined as the minimum EBIE time needed to detect a pit in AFM images of the substrate. This comparison is appropriate because the initial experimental etch rate was undetectable (over the intrinsic surface roughness of the as-grown UNCD), implying that t_e is governed by N_s and essentially independent of σ_a. Conversely, a quantitative comparison of the etch rates, $\frac{\partial z_d}{\partial t}$, at 5, 10 and 20 keV is confounded by the fact that the amplitude of the secondary electron spectrum and hence the value of σ_a change with E_0.

Figure 3.4 shows the experimental data obtained using electron beam energies of 5 and 10 keV. The results are expressed as the maximum depth detected in the AFM image of each etch pit so as to show how the values compare to the intrinsic surface roughness of the substrate (a sample AFM image and line profile are shown in 3.4b). The figure also shows the etch onset times predicted for 5 and 10 keV using:

$$t_e(E_0) = t_{20}\xi_{20}/\xi_{E_0}, \tag{3.9}$$

where t_{20} is the experimental etch onset time at 20 keV (obtained from the data shown in Figure 3.2), ξ_{20} is $\frac{\partial E}{\partial z}[t \to 0]$ at $E_0 = 20\ keV$, and ξ_{E_0} are the corresponding values at 5 and 10 keV (shown in Figure 3.3). The predicted etch onset times are in good agreement with experiment, indicating that the initial rate does indeed scale with the energy density deposited into the near-surface region of the substrate, as predicted by model #3.

[5] The values of σ_α and σ_a used in the models represent cross-sections weighed by the overlap between the corresponding energy dependent cross-section and energy spectra of electrons incident onto and emitted from the substrate [1].

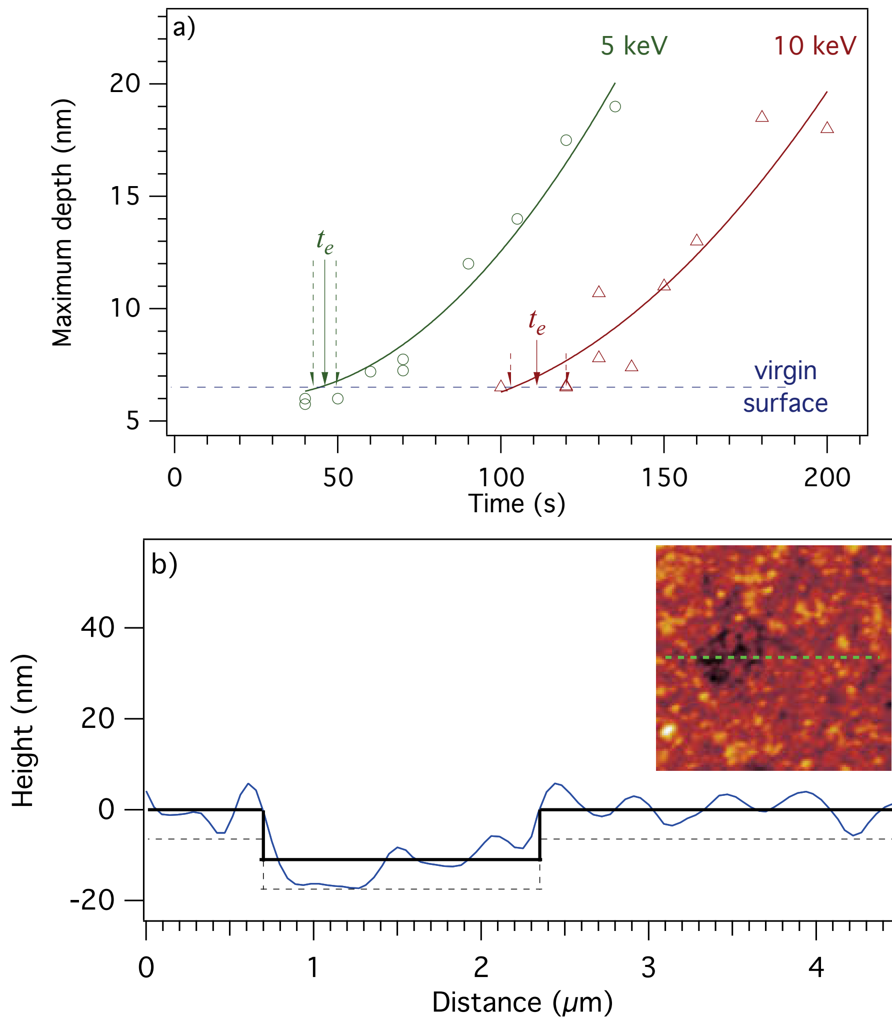

FIGURE 3.4: a) Maximum depth of pits in UNCD fabricated using 5 and 10 keV electron beams, plotted as a function of etch time. The dashed horizontal line indicates the maximum depth measured in adjacent, non-irradiated regions of UNCD, and serves as a measure of initial surface roughness. Arrows labelled t_e show the etch onset times predicted using model #3. Dashed arrows show the corresponding error bars. b) AFM line profile across a pit fabricated using a beam energy of 5 keV and an etch time of 120 s. The solid and dashes lines show the location of the etch pit and the substrate surface determined using the minimum and average depths measured inside and near the etch pit. *Inset:* AFM image and the position of the line scan used to generate the plot in (b).

3.5 Conclusions

We have incorporated dynamic surface site activation and the role of electron beam damage into models of EBIE rate kinetics. The refined models yield higher order rate kinetics, predict a new rate kinetics regime limited by the concentration of active surface sites, N_s,

and reduce to standard EBIE models when the active site coverage approaches unity (i.e., $A_s N_s \rightarrow 1$). The refined models are in good agreement with experiments which indicate that EBIE of UNCD proceeds through an electron restructuring pathway. Analogous restructuring effects likely play a role in EBIE of other materials, and possibly account for atypical dependencies of etch rate on time which have been reported previously for a number of precursor-substrate combinations [2, 17, 202]. The results presented here have implications for the construction of predictive EBIE models, ultimate resolution and proximity effects inherent to EBIE.

Author Contributions

Aiden Martin and Milos Toth designed the project. Aiden Martin performed the experiments. Aiden Martin and Milos Toth performed the numerical modelling. All authors analysed the data and contributed to the writing of the manuscript.

Chapter 4

Dynamic Formation of Topographic Patterns During EBIE of Single Crystal Diamond

4.1 Abstract

This chapter describes the dynamics of pattern formation during gas-mediated electron beam induced etching (EBIE) of single crystal diamond. Patterns are observed by simultaneous secondary electron imaging during etching. The etch rate anisotropy of H_2O-mediated EBIE of (001) oriented diamond gives rise to terraced step formation and propagation of the etch front in the [110], $[\bar{1}10]$, $[\bar{1}\bar{1}0]$ and $[1\bar{1}0]$ directions of the surface. From this pattern we determined the (110), $(\bar{1}10)$, $(\bar{1}\bar{1}0)$ and $(1\bar{1}0)$ planes have the slowest etch rate of the crystallographic orientations. The addition of NH_3 precursor gas to H_2O results in stabilisation of {111} planes by hydrogen radicals, which significantly changes the surface topography. This study of self-ordered pattern formation provides key insights into EBIE reaction kinetics and mechanisms, which are critical for the processing of this advanced material.

4.2 Introduction

Erosion of material by ion sputtering [203–207] and gas-assisted focused ion beam (FIB) milling [208, 209] gives rise to self-ordered pattern formation under specific material, particle and environmental conditions. In addition to being visually stimulating, these patterns give important insight into reaction mechanisms which enable ordered fabrication of technologically important structures such as semiconductor quantum dots [210] and black silicon [211]. In this chapter, we present a new method for simultaneously producing and observing self-ordered topographic patterns in single crystal material. Erosion of material is realised by EBIE and the evolving structure observed by secondary electron imaging, using a scanning electron microscope (SEM).

Diamond has found applications across numerous areas of science due to its unique combination of optical, electronic, chemical, thermal and quantum properties [112, 113]. Previous studies of the EBIE of single crystal diamond have shown EBIE to be ideal for fabricating optically active structures and polishing material [19–21, 178], without producing the structural damage induced by FIB milling [147, 212]. The kinetics and mechanisms of EBIE which are critical for predictive models however, are not well understood.

EBIE is a dry, chemical process where surface adsorbed precursor molecules (i.e. H_2O) are dissociated by an electron beam, producing reactive fragments (O^*). The fragments react with surface atoms (C), producing volatile molecules (CO_x) that desorb from the surface leaving a void [42]. The rate of etching in the standard EBIE model is described in terms of the concentration of reactive fragments (N_α) at the substrate surface which give rise to etching and is defined by [1, 26, 28, 42, 44, 46, 92–94, 191]:

$$\frac{\partial N_\alpha}{\partial t} = \sigma_\alpha \; f \; N_a, \tag{4.1}$$

where f is electron flux, σ_α is the effective cross-section for the generation of fragments that volatilise the substrate, and N_a is the concentration of surface adsorbed precursor molecules. The standard model however, does not include various substrate properties and previous EBIE studies have shown this description of the etch kinetics is poor at

reproducing the effects seen in materials such as ultra nano-crystalline diamond [94] and silicon [44].

Here we report EBIE of (001) and (111) orientated single crystal diamond under various gaseous environment conditions. Kinetics and mechanisms of EBIE of single crystal diamond are inferred by interpretation of the dynamics of pattern formation. The patterns formed during etching are a result of anisotropic etching along crystallographic planes, which varies with gaseous species. Anisotropic etching is commonly observed in wet chemistry, plasma and reactive ion etching of single crystal material [63] but has not been observed in previous studies of EBIE.

Absence of anisotropic etching in previous studies of EBIE of silicon is due to the precursor chemistry and substrate conditions used for etching. XeF_2 [213], NF_3 [182] and SF_6 [25]-mediated EBIE of silicon proceed through a fluorine chemical pathway, which results in isotropic removal of material [29]. Chlorine-based chemical etching can give rise to anisotropic etching of silicon under specific conditions [214], however anisotropic etching was not observed in Cl_2-mediated EBIE of silicon [24]. This is likely due to changes in the etch kinetics caused by the presence of hydrocarbon contaminants [16, 23] or silicon doping levels [214]. The absence of observation of anisotropic etching during EBIE of these systems also shows that the variation in work function [215] and precursor binding energy [216] between crystal planes has minimal affect on etch rate anisotropy. Work function and precursor binding energy vary the magnitude of the secondary electron yield [217] and N_a respectively.

4.3 Results and Discussion

EBIE of (001) (Element Six, CVD grown, [001] surface direction) and (111) (B-doped, CVD grown, [111] surface direction) orientated single crystal diamond was performed under various gaseous environments with a 5 keV electron beam at room temperature using an FEI Nova NanoSEM variable pressure [95] SEM equipped with a magnetic immersion lens gaseous secondary electron detector [150]. Prior to etching, diamond substrates were

cleaned by sonication in chloroform, acetone, isopropyl alcohol and Milli-Q H_2O respectively for 30 minutes each, followed by cleaning in piranha etch solution (H_2SO_4:H_2O_2, 3:1) for 30 minutes to remove silicone and hydrocarbon oils. This aggressive cleaning method was used to ensure contaminants did not affect the etch kinetics.

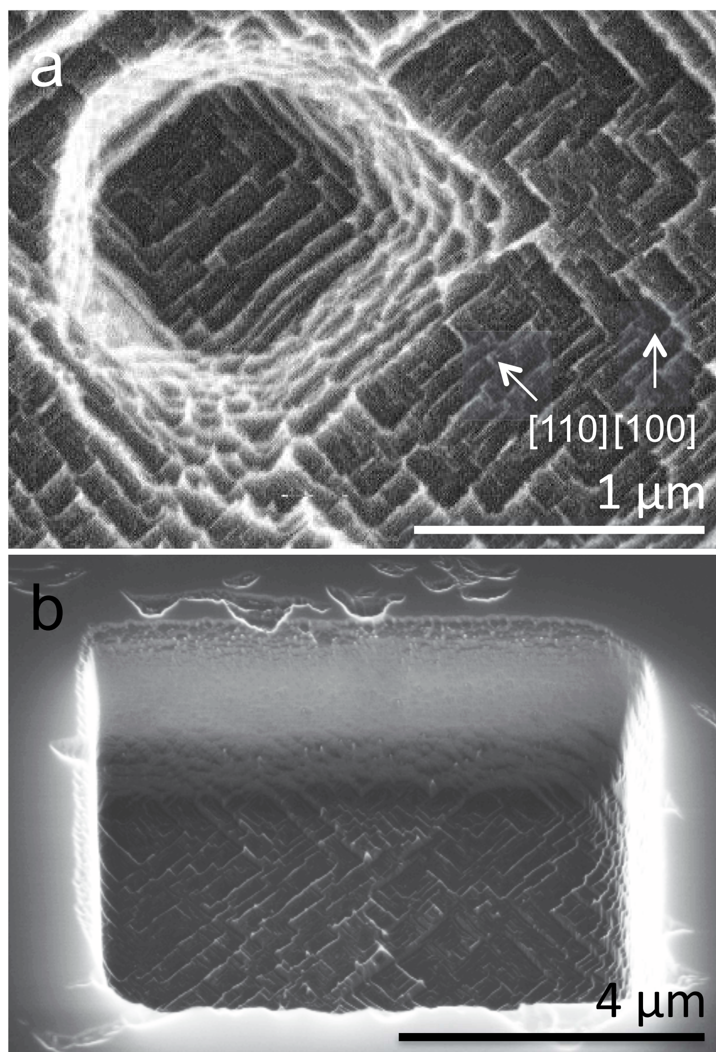

FIGURE 4.1: a, b) SEM images of topographic features produced by H_2O-mediated EBIE of single crystal (001) orientated diamond using a 5 keV electron beam, normal to the substrate.

EBIE of (001) oriented diamond substrate was performed in a 9.3 Pa environment of H_2O with the electron beam normal to the substrate (Figure 4.1 and Supplementary Information Video 1). Etching was observed to begin at surface imperfections and with time terraced steps appeared across the irradiated region of the substrate. After formation the surface

topography is dynamic, with the step edges propagating across the surface in the [110], [$\bar{1}$10], [$\bar{1}\bar{1}$0] and [1$\bar{1}$0] directions. Surface material is removed as the steps propagate across the surface until finally coming to rest at the edge of the area irradiated by the electron beam.

Terraced step formation is a direct result of anisotropic etching along the major diamond crystallographic orientations, with surface topography dominated by the slowest etching set of planes [52]. Here {111} planes are noticeably absent from the topography due to rapid removal by oxidative etching [218]. Sidewalls of the steps are the slowest etching (110), ($\bar{1}$10), ($\bar{1}\bar{1}$0) and (1$\bar{1}$0) planes. The 90° step corners are formed at the intercepts of the (110), ($\bar{1}$10), ($\bar{1}\bar{1}$0) and (1$\bar{1}$0) planes. For corner formation in this direction to occur the (100), (010), (0$\bar{1}$0) and ($\bar{1}$00) planes must be removed at a rate faster than the (110), ($\bar{1}$10), ($\bar{1}\bar{1}$0) and (1$\bar{1}$0) planes. From these observations, we conclude that H_2O-mediate EBIE removes material from the 100 and 111 set of planes at a faster rate than the (110), ($\bar{1}$10), ($\bar{1}\bar{1}$0) and (1$\bar{1}$0) group of planes.

To determine the dependence of electron beam tilt on the anisotropy of etching, H_2O-mediated EBIE of the (001) orientated diamond was performed with a substrate tilt of 30° (Figure 4.2a and Supplementary Information Video 2). The resulting surface topography is similar to that obtained with an electron beam normal to the substrate (Figure 4.1), with steps forming and propagating in [110], [$\bar{1}$10], [$\bar{1}\bar{1}$0] and [1$\bar{1}$0] directions. A schematic of the surface geometry post-EBIE is shown in Figure 4.2b. A noticeable difference between the two substrate tilt conditions is terrace step formation only being pronounced at the ($\bar{1}$10) and ($\bar{1}\bar{1}$0) planes, while large walls are present at the (110) and (1$\bar{1}$0) planes. The difference in surface topography is likely due to the local electron flux being a function of the incidence angle of the electron beam with the surface plane. As the electron interaction volume can vary significantly based on the surface topography, the flat wall and terraced step formations also exacerbates the difference in local electron flux during etching.

The relationship between local electron flux and electron beam incidence angle can also describe the difference in etch rate between planes in the {110} set of planes when the electron beam is normal to the substrate (Figure 4.1). While equivalent in structure, the (110), ($\bar{1}$10), ($\bar{1}\bar{1}$0) and (1$\bar{1}$0) group of planes differ from the (101), (011), ($\bar{1}$01) and (0$\bar{1}$1)

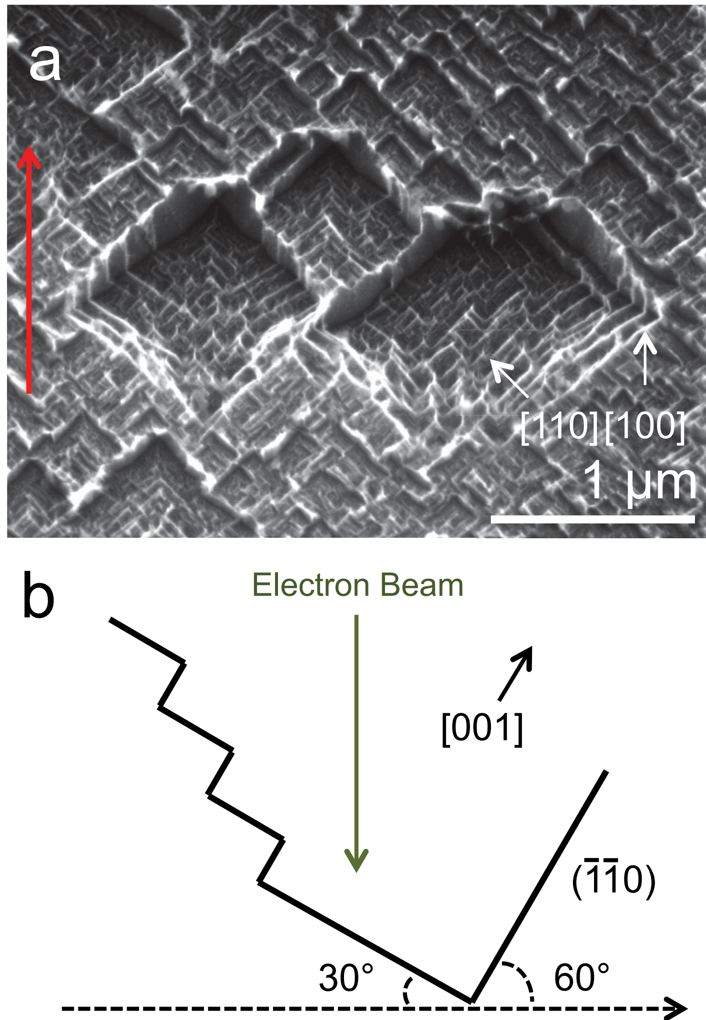

FIGURE 4.2: a) SEM image of topographic features produced by H_2O-mediated EBIE of single crystal (001) orientated diamond at 30° substrate tilt using a 5 keV electron beam. Red arrow indicates direction of line profile in (b). b) Schematic of observed etch profile.

group of planes by 45° in θ (where θ is the polar angle, measured relative to the substrate normal). If the local electron flux was identical for both groups of planes the (101), (011), ($\bar{1}$01) and (0$\bar{1}$1) group of planes would have the same etch rate as the (110), ($\bar{1}$10), ($\bar{1}\bar{1}$0) and (1$\bar{1}$0) group, and the surface topography would be dominated by (101), (011), ($\bar{1}$01) and (0$\bar{1}$1) features.

Next, we investigated the influence of precursor chemistry on etch rate anisotropy by performing EBIE of (001) orientated diamond with NH_3 added to the gaseous environment

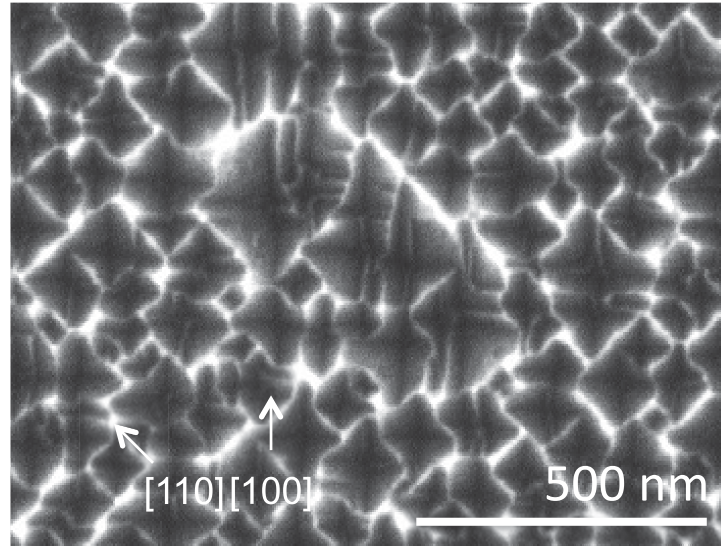

FIGURE 4.3: SEM images of topographic features produced by NH_3-mediated EBIE of single crystal (001) orientated diamond using a 5 keV electron beam.

(1.9 Pa H_2O and 6.4 Pa NH_3). Significant changes are observed in the structure produced by EBIE under these conditions (Figure 4.3 and Supplementary Information Video 3). We note that structures produced in an environment of only NH_3 are identical to those produced with the addition of H_2O. Etching of material likely proceeds through dissociation of injected or residual [14] H_2O. The contribution to etching of carbonaceous material by dissociation of residual H_2O is detailed in Chapter 2. Inverted pyramids of varying size are formed across the surface, in stark contrast to the terraced step formation seen with only H_2O. The walls of the inverted pyramids are {111} planes, which implies that the {111} planes have the slowest etch rate of the crystallographic orientations. We ascribe this change in anisotropic etching to the generation of hydrogen and amidogen (NH_2) at the surface by electron induced dissociation of NH_3 [14]. Hydrogenation reconstructs [219] and NH_2 can terminate [220] the sp^3 {111} surface. Hydrogenation likely plays the major role in changing the anisotropy of etching by protecting the {111} surface from further oxidation [219].

Finally, we show the atomic arrangement of the diamond surface during etching can be inferred directly from pattern formation during EBIE of (111) orientated diamond. Previous studies have shown the direction of trigon formation (positive or negative [221]) in (111) orientated diamond directly relates to the coordination of surface atoms in diamond

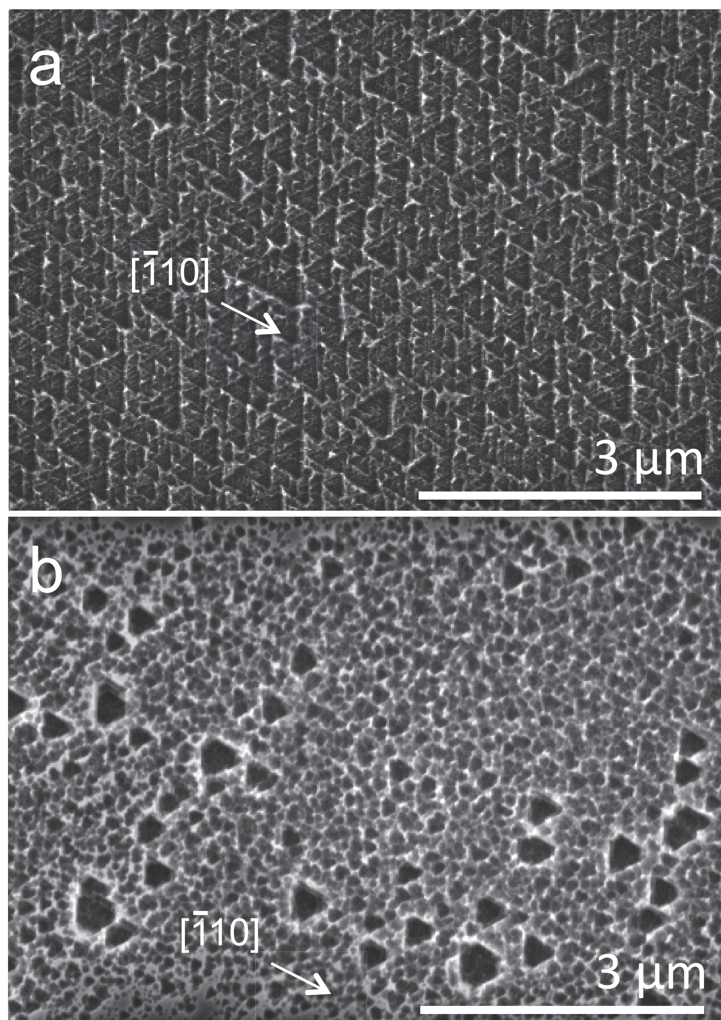

FIGURE 4.4: SEM images of topographic features produced by (a) H_2O and (b) NH_3-mediated EBIE of single crystal (111) orientated diamond using a 5 keV electron beam.

crystal structure materials [222–224]. To determine the surface atom arrangement during EBIE with different precursor chemistries, a series of irradiations was performed in H_2O (9.3 Pa) and NH_3 (1.3 Pa H_2O and 5.9 Pa NH_3) gaseous environments (Figure 4.4).

EBIE performed with H_2O precursor results in the formation of positive trigons which expand across the surface with time (Figure 4.4a and Supplementary Information Video 4). Comparing this result to a previous study of gas phase etching of diamond with O_2 and H_2O, we ascribe the formation of positive trigons during H_2O-mediated EBIE to arise from lattice edge atoms being bound directly to two carbon atoms in the lattice [218]. The

two dangling bonds are likely terminated by -OH, -H, =O or a C-O-C bridge between two neighboring carbon atoms [223].

Inclusion of NH_3 to the gaseous environment produces structures that are initially hexagonal in shape and expand to form negative trigons as EBIE proceeds (Figure 4.4b and Supplementary Information Video 5). As shown in the case of (100) terminated diamond, NH_3 stabilises the {111} surface, which is likely to arise from hydrogenation or amination of the surface. Negative trigons have one dangling bond at their lattice step edges, indicating stabilisation of the dangling bond by a monovalent atom [223]. We therefore present this finding as further evidence that hydrogen and NH_2 fragments produced by electron induced dissociation of NH_3 dominate the etch rate anisotropy.

4.4 Conclusions

In summary, we have determined the kinetics and mechanisms of EBIE of single crystal diamond under different environmental conditions by interpretation of dynamic patterns formed by the etching process. Pattern formation was shown to be dependent on the gaseous environment used for etching which causes a change in the anisotropy of etching. EBIE of (001) orientated diamond in a H_2O environment proceeds with rapid removal of the {111} set of planes and slow etching in the (110), $(\bar{1}10)$, $(\bar{1}\bar{1}0)$ and $(1\bar{1}0)$ planes leading to terraced step formation. Positive trigon formation in (111) orientated diamond shows step edge atoms to be bound to two neighboring carbon atoms during EBIE in H_2O. The addition of NH_3 to the gaseous environment changes the EBIE reaction mechanism through production of hydrogen radicals by electron induced dissociation of NH_3. Hydrogen radicals terminate the surface leading to stabilisation of the {111} set of planes, with step edge atoms bound to three neighboring carbon atoms during etching and the surface protected from oxidation. Etching of (001) oriented diamond with NH_3 present is therefore dominated by slow etching of {111} planes leading to an inverted pyramid surface topography.

Anisotropic etching and the local electron flux dependence on electron beam incidence angle were shown to be important parameters in describing the etching of diamond. These

results have major implications for the methods used to perform EBIE of single crystal material and demonstrates a new method for the fabrication of self-ordered patterns. The fabricated structures are similar in topography to anti-reflection layers produced in silicon [225]. EBIE may therefore provide a route to directly fabricate these structures in selected areas of optical devices. With optimisation of material and gas chemistry we predict the structures fabricated here by EBIE processing of diamond to extend to other single crystal materials including silicon.

Author Contributions

Aiden Martin and Milos Toth designed the project. Aiden Martin and James Bishop performed the experiments. Aiden Martin and Milos Toth analysed the data and contributed to the writing of the manuscript.

Chapter 5

Subtractive 3D Printing of Optically Active Diamond Nanostructures

5.1 Abstract

Controlled fabrication of semiconductor nanostructures is an essential step in engineering of high performance photonic and optoelectronic devices. Diamond in particular has recently attracted considerable attention as a promising platform for quantum technologies, photonics and high resolution sensing applications. Here we demonstrate the fabrication of optically active, functional diamond structures using gas-mediated electron beam induced etching (EBIE). The technique achieves dry chemical etching at room temperature through the dissociation of surface-adsorbed H_2O molecules by energetic electrons in a water vapor environment. Parallel processing is possible by electron flood exposure and the use of an etch mask, while high resolution, mask-free, iterative editing is demonstrated by direct-write etching of inclined facets of diamond microparticles. The realised structures demonstrate the potential of EBIE for the fabrication of optically active structures in diamond.

5.2 Introduction

Diamond, long considered unconquerable due to its extraordinary strength and chemical resistance, has found applications across numerous areas of science due to its unique combination of optical, electronic, chemical and thermal properties [112]. Most notably, the nitrogen-vacancy luminescence center (NV) has been employed as a spin qubit, enabling the use of diamond as a platform for next generation sensing, nanophotonic and quantum devices [139–145]. These tantalising applications are, however, overshadowed by challenges in fabrication arising from its extraordinary hardness and chemical resistance.

At present, diamond fabrication requires cumbersome masking techniques, and ion bombardment or high power laser ablation, which often causes damage and material redeposition artifacts [126–130]. Fabrication and editing of optoelectronic grade nanostructures is therefore extremely limited relative to conventional semiconductors such as silicon and gallium arsenide. Furthermore, direct-write, deterministic patterning of optical structures in diamond has not been demonstrated in the absence of severe surface damage caused by ion implantation and redeposition of non-volatile, sputtered or ablated material.

Here we demonstrate the fabrication of functional, optically active diamond structures using EBIE [1, 19, 20, 26, 94] (Figure 5.1). EBIE achieves dry chemical etching at room temperature in a water vapor environment through the electron-induced dissociation of surface-adsorbed H_2O molecules, generating reactive fragments that give rise to volatilisation of carbon. The reaction steps are shown in Figure 5.1b and c. The process utilises low energy electrons which do not cause damage through knock-on displacement of carbon, sputtering and staining that are characteristic of focused ion beam milling, and cause quenching of diamond luminescence [1, 148]. Parallel processing is possible by electron flood exposure and the use of an etch mask. Mask-free EBIE is used to realise direct-write subtractive 3D printing of diamond nanostructures on inclined planes of diamond microparticles. The processes are demonstrated using a variable pressure scanning electron microscope (SEM) making diamond nanofabrication accessible to most nanotechnology laboratories in the world.

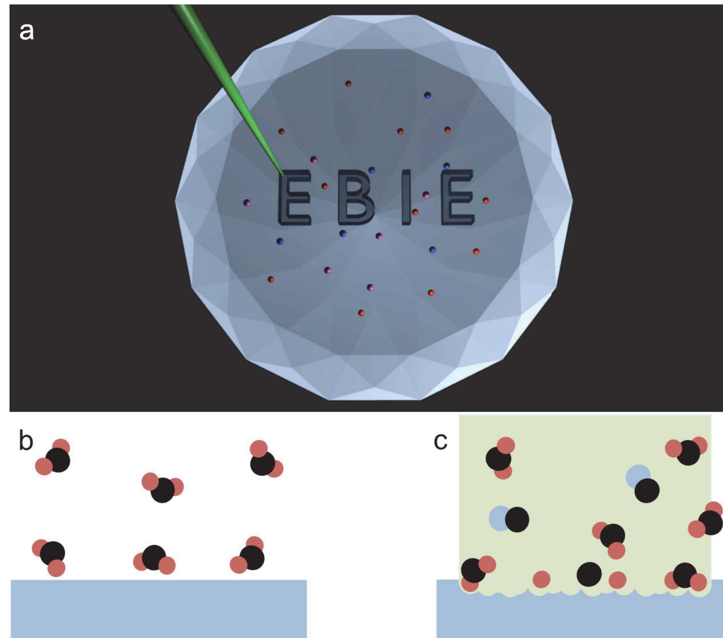

FIGURE 5.1: Schematic illustrations of H_2O-mediated EBIE. a) Direct-write subtractive printing of diamond. b-c) Volatilisation of diamond by electron exposure in a gaseous H_2O environment.

5.3 Results and Discussion

To demonstrate the applicability of EBIE to device fabrication, we start by fabricating a pillar from a single crystal diamond using an etch mask. Pillars are used as antennas that enhance light extraction from embedded emitters, particularly of high refractive index semiconductors. The EBIE process is shown schematically in Figure 5.2a-c. The mask must either absorb the incident electrons or prevent H_2O from adsorbing to the diamond substrate. Here we use a silica mask to prevent low energy (2 keV) electrons from penetrating into underlying regions of diamond. The resulting pillars (Figure 5.2d) have high aspect ratios and straight side-walls, making them ideal for photonic applications. The minimum pillar diameter is ultimately limited by the diameter of the interaction volume of a delta function electron beam, which scales super-linearly with electron energy [226]. In diamond, it is equal to $\sim$ 19 nm at 2 keV, and $\sim$ 9 nm at 1 keV, as shown in Figure 5.2e [170]. Nanostructures can therefore be fabricated with high resolution using the correct combination of mask diameter and electron energy. On the other hand, micron sized depths can be achieved, enabling high aspect ratio geometries.

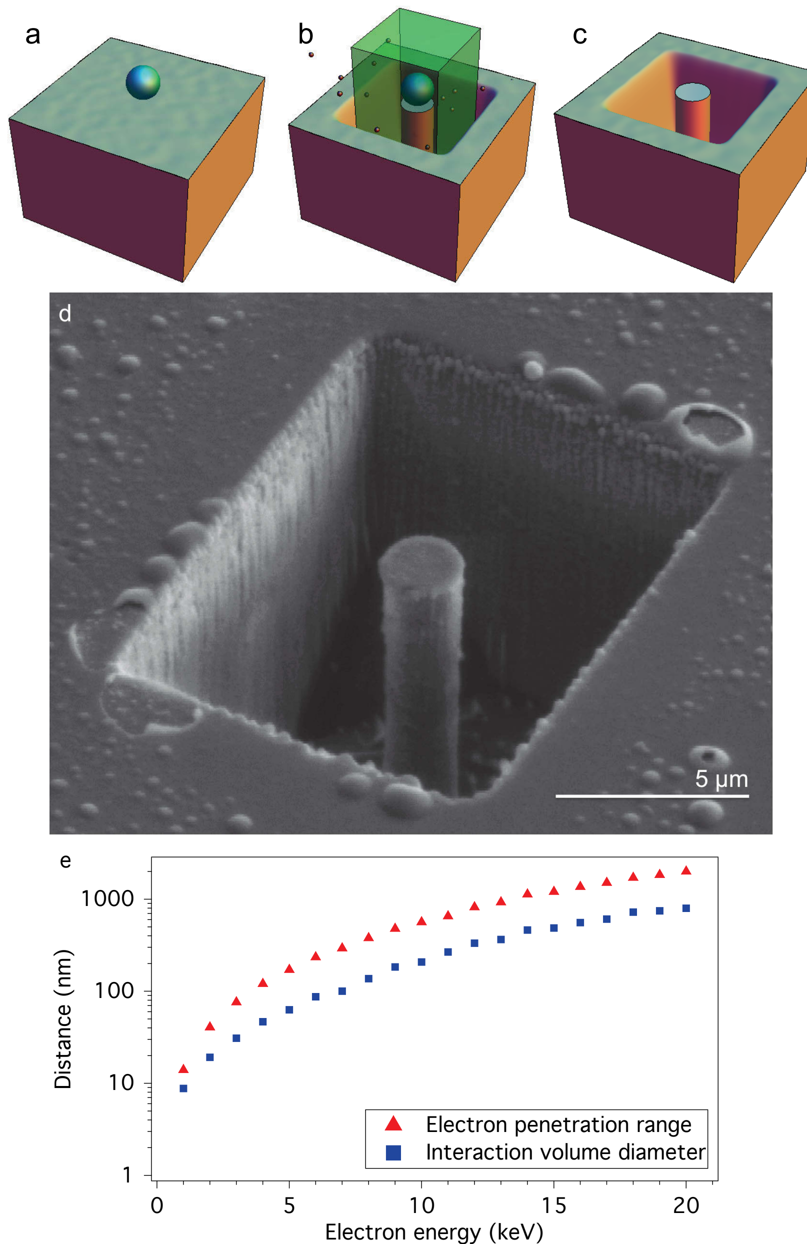

FIGURE 5.2: Diamond pillar fabricated by mask-based EBIE. a-c) Schematic illustration of pillar fabrication by H_2O-mediated EBIE. a) Silica bead on a diamond surface. b) Diamond volatilisation achieved by scanning a 2 keV electron beam over a rectangle repeatedly in a H_2O environment. The silica bead acts as an etch mask that prevents the electrons from reaching the diamond surface. c) Final pillar geometry after the silica bead was removed from the substrate. d) Electron image of a pillar fabricated in single crystal diamond by H_2O-mediated EBIE using the process shown in (a-c). e) Depth and diameter of the electron interaction volume that contains 90 % of the energy deposited into diamond, plotted as a function of electron energy. The values were calculated using a Monte Carlo model of electron-solid interactions.

Optical properties of the pillars are shown by the fluorescence and Raman scattering data in Figure 5.3. Photoluminescence (PL) spectra were recorded using a confocal microscope with a 532 nm excitation laser. The PL intensity of the pillar (Figure 5.3a) shows a two-fold increase over the neighboring, unprocessed region of diamond (under identical PL collection conditions). Raman spectroscopy (Figure 5.3b) shows no evidence of graphitic inclusions in the irradiated area with the first-order diamond peak positioned at 1332 cm^{-1} and FWHM of $\sim$ 3.6 cm^{-1}, consistent with the Raman signature of pristine, single crystal diamond [138, 163].

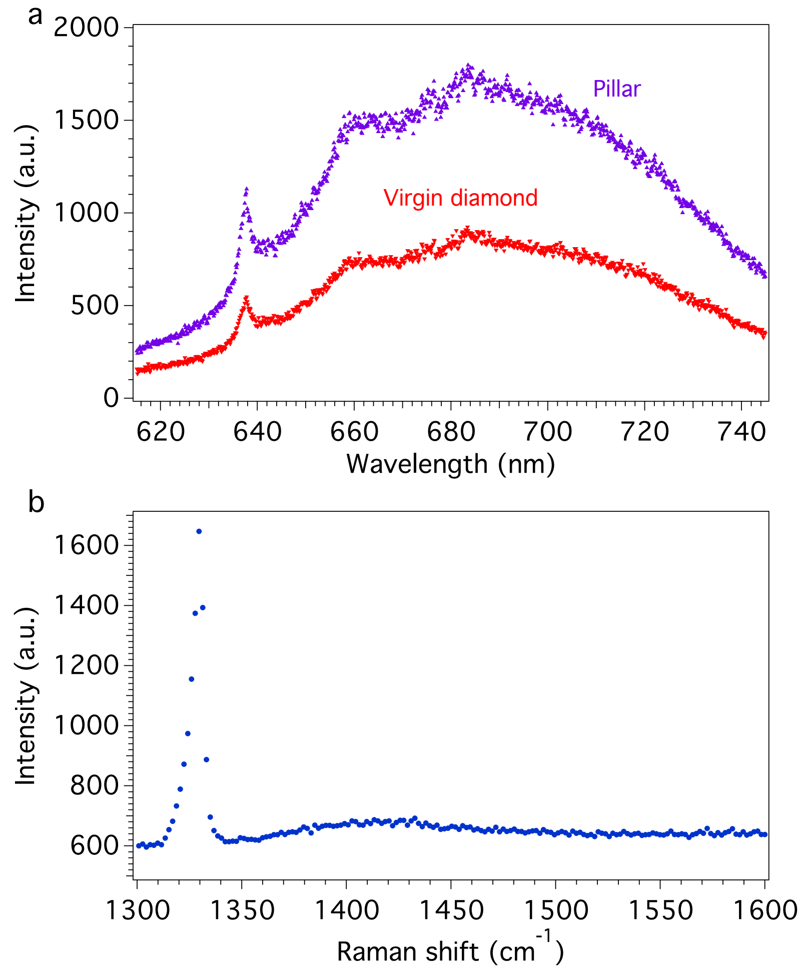

FIGURE 5.3: Optical quality of a diamond pillar fabricated by EBIE. a) PL spectra of the pillar and an adjacent, unprocessed region of diamond. b) Raman spectrum of the pillar showing the absence of defects generated by EBIE.

Next, we demonstrate the capability of EBIE for mask-free editing of inclined diamond

surfaces. Editing of multiple inclined facets is nearly impossible by mask-based processing techniques, including electron- and photo-lithography. To demonstrate the three dimensional capability of writing on inclined surfaces, we patterned the letters 'UTS' and 'NANO' into individual microparticles (Figure 5.4) simply by tracing out the letters using an electron beam as shown schematically in Figure 5.1d. Etching was carried out using a 20 keV electron beam, while charging was stabilised using a low vacuum (13 Pa) environment of H_2O. The letters are clearly visible in SEM images (Figure 5.4a), while atomic force microscope (AFM) maps of the 'UTS' logo show line widths and depths of $\sim$ 100 nm (Figure 5.4b). The letters 'NANO' were written intentionally across three diamond (111) facets, showing the ability of EBIE to edit three dimensional, inclined nanostructures. Figure 5.4c shows an individual diamond microparticle with visible (111) facets and Figure 5.4e shows the word 'NANO' imprinted in the crystal, with the letters 'NA', 'N' and 'O', occupying all three (111) planes, respectively. PL measurements recorded from the diamond microparticles exhibit strong fluorescence, confirming that the etch process does not destroy optical properties and material functionality (See Figure 5.5 in the Supporting Information). The maskless patterning approach is particularly attractive for generation of high resolution microfluidic channels in microdiamond crystals, in close proximity to optical emitters [227, 228].

5.4 Conclusions

The potential of EBIE exceeds that of traditional etching techniques for wide bandgap semiconductors. For instance, a combination of EBIE with cathodoluminescence analysis techniques may enable probing of the spectroscopic properties of nanostructures while the etch parameters are modified during fabrication. Alternatively, substrate tilting can enable fabrication of undercut structures that are currently not available in diamond. Finally, the EBIE method will be pivotal for realising hybrid devices when direct sculpting of a nanostructure is required to achieve close proximity with an external cavity or metallic nanostructure [229].

We have demonstrated a promising approach to pattern and sculpt optically active diamond structures using two variants of H_2O-mediated electron induced chemical etching: a

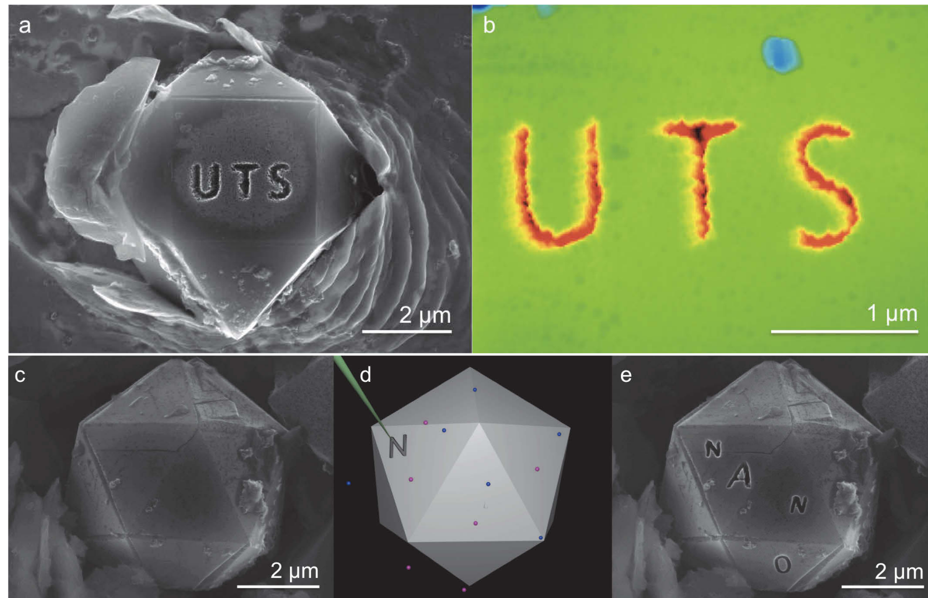

Figure 5.4: Beam-directed editing of Si-doped diamond micro-particles. a) SEM image of the symbol 'UTS' patterned by H_2O mediated EBIE on the 110 plane of a single diamond micro-particle embedded in platinum. b) AFM image of the symbol 'UTS' shown in a (depth of each letter $\sim$ 100 nm). c) SEM image of a diamond micro-particle. d) Schematic illustration of the process used to pattern the micro-particle shown in (c). Each letter of 'NANO' was patterned individually using H_2O mediated EBIE on three different 111 faces of diamond. e) SEM image of the microparticle shown in (c) after the letters 'NANO' were patterned by EBIE.

mask-based lithographic approach, and an extremely versatile, direct-write editing process. For the first time, direct 3D writing is realised on various facets of a single microparticle. PL and Raman analysis were used to show that the unique optical properties of diamond are maintained and no graphitisation occurs. By leveraging the advanced functionalities provided by a conventional SEM in conjunction with EBIE a modification to existing devices and direct nanofabrication for rapid prototyping is enabled. EBIE is the first step towards rendering 3D single crystal diamond geometries for high performance photonic, sensing and quantum devices.

5.5 Methods

EBIE of diamond pillar. EBIE was performed using a FEI Nova NanoSEM variable pressure [95] SEM equipped with a magnetic immersion lens gaseous secondary electron

detector [150]. The SEM chamber was pumped to 3×10^{-4} Pa prior to performing EBIE at room temperature under 13 Pa of H_2O (Milli-Q) precursor vapor. Pillars were fabricated using dispersed 2 μm silica beads that served as a hard mask on a (100) oriented single crystal diamond (Element Six). Silica beads were transferred from a suspension in isopropyl alcohol, which was flash dried to remove the solvent. Single beads were located in the SEM before irradiation. H_2O-mediated EBIE was performed by irradiating a 10 μm $\times$ 8 μm rectangle with a 2 keV, 29.9 nA electron beam for 12 hours, using a dwell time of 1.34 ms per pixel. Electron penetration and energy deposition profiles were calculated using standard Monte Carlo models of electron-solid interactions [167, 170].

Optical measurements. PL measurements were performed using a custom confocal microscope with a 532 nm excitation laser. Raman measurements were performed using a Renishaw inVia Raman microscope with a 633 nm excitation laser.

EBIE of diamond micro particles. Diamond micro-particles were grown using a CVD method ($\sim$ 950 W, 1 % methane, 8×10^3 Pa). The particles were transferred to a platinum surface prior to EBIE. The 'UTS' symbol was etched into a single particle using a 20 keV, 9.9 nA electron beam controlled using a custom pattern generator connected to the SEM scan coils. The dwell time per pixel was 256 ms and the total process time 15 minutes. The symbol 'NANO' was etched using the same conditions, but etch letter was etched individually into the diamond. The 'UTS' symbol was measured ex situ using the tapping mode of a Digital Instruments Dimension 3100 atomic force microscope (AFM), and analysed using the software package Gwyddion [158].

5.6 Supporting Information

EBIE proceeds through the dissociation of surface-adsorbed precursor molecules (e.g. H_2O) by electrons, generating radicals (O*) that react with surface atoms (C) to produce volatile species (CO_x, where x = 1 - 2) that desorb and are removed by the pumping system, leaving a void in the substrate [1]. Substrates that are electrical insulators can be charge-stabilised by an environmental scanning electron microscope (ESEM) to the extent needed to achieve nanometer ESEM image resolution [151]. Graphitisation and

material staining that is present in focused ion beam milling [1, 148] can be avoided, by using electron beam energies lower than the knock-on displacement threshold of diamond ($\sim$ 145 keV) [230].

Figure 5.5 shows a photoluminescence (PL) spectrum taken from a diamond microparticle after it was edited by EBIE. The strong luminescence centered at 738 nm is associated with the silicon-vacancy colour center in diamond [231].

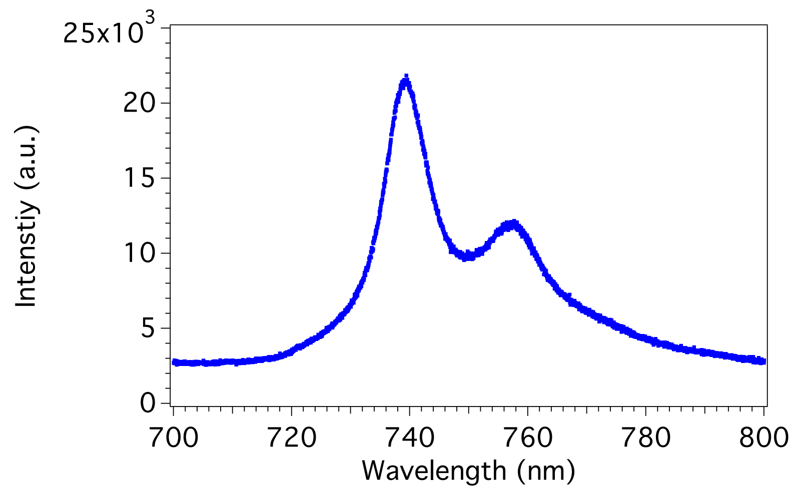

FIGURE 5.5: Room temperature PL spectrum confirming the presence of the silicon-vacancy colour center with the characteristic zero phonon line at 738 nm.

Author Contributions

Aiden Martin, Milos Toth and Igor Aharonovich designed the project. Aiden Martin performed the EBIE experiments and Raman measurement. Aiden Martin and Igor Aharonovich performed the PL measurements. Aiden Martin performed the Monte Carlo simulations. All authors analysed the data and contributed to the writing of the manuscript.

Chapter 6

Maskless Milling of Diamond by a Focused Oxygen Ion Beam

6.1 Abstract

Recent advances in focused ion beam (FIB) technology have enabled high-resolution, maskless nanofabrication using light ions. Studies with light ions to date have, however, focused on milling of materials where sub-surface ion beam damage does not inhibit device performance. Here we report on maskless milling of single crystal diamond using a focused beam of oxygen ions. Material quality is assessed by Raman and luminescence analysis, and reveals that the damage layer generated by oxygen ions can be removed by non-intrusive post-processing methods such as localised electron beam induced chemical etching.

6.2 Introduction

FIB milling is a popular technique for rapid, direct-write nanofabrication via the sputtering of target material through momentum transfer from an energetic primary ion [42]. Most commercial FIB systems are equipped with gallium liquid metal ion sources [77]. However, advances made over the past decade in technologies such as gas field ion [232–234] and inductively coupled plasma [235, 236] (ICPS) sources have increased the use of light species

(H, He, O and Ne) in the fabrication of nanostructures [237–239]. These species enable control over implantation, sputtering and chemical interactions with the target, but the damage generated by many of these ions is poorly understood at the high fluences required for FIB milling [147, 235] (relative to those used for implantation [240, 241]).

In this chapter, we report maskless milling of optical structures in single crystal diamond using a focused beam of oxygen ions. To characterise the influence of the ions on material properties, we employ photoluminescence (PL) and Raman spectroscopy, and constant power cathodoluminescence (CL) depth profiling of the nitrogen-vacancy (NV) colour centre [169]. We find the neutral nitrogen-vacancy (NV^0) CL emission is quenched over depths much greater than those expected from simple binary approximation Monte Carlo simulations of ion interactions with matter [172]. We conclude that oxygen channelling contributes significantly to the sub-surface damage profile of single crystal diamond. The damage layer is significantly thicker than that generated by Ga^+ ions. It can, however, be removed by relatively nonintrusive localised methods such as H_2O-mediated electron beam induced etching [42, 177, 178] (EBIE).

Diamond is a promising material for quantum photonic applications due to it's unique chemical, physical and optical properties [114]. During FIB milling, momentum transfer from the ions to the target atoms above a critical dose [146, 147] induces amorphisation of diamond within the ion interaction volume. For gallium based FIB milling this amorphisation damage profile is on the order of 46 nm at an ion energy of 30 keV, and the damage layer is heavily stained by implanted gallium ions [147]. It has been shown that gallium staining can be partly removed by ex situ hydrogen plasma and chemical etch treatments [148, 149]. In general, however, it is desirable to utilise in situ techniques such as EBIE, which are typically free from material degradation caused by material incompatibilities with aggressive chemical treatments.

6.3 Results and Discussion

An undercut bridge structure [148] was fabricated in (100) oriented single crystal diamond (CVD grown, Element Six) by a focused oxygen beam (O^+ / ${O_2}^+$ ions, approximately 1:1

relative ion abundance ratio) using an FEI Vion FIB [242] modified to incorporate an O_2 source. The resulting free-standing diamond structure is shown in the inset of Figure 6.1a.

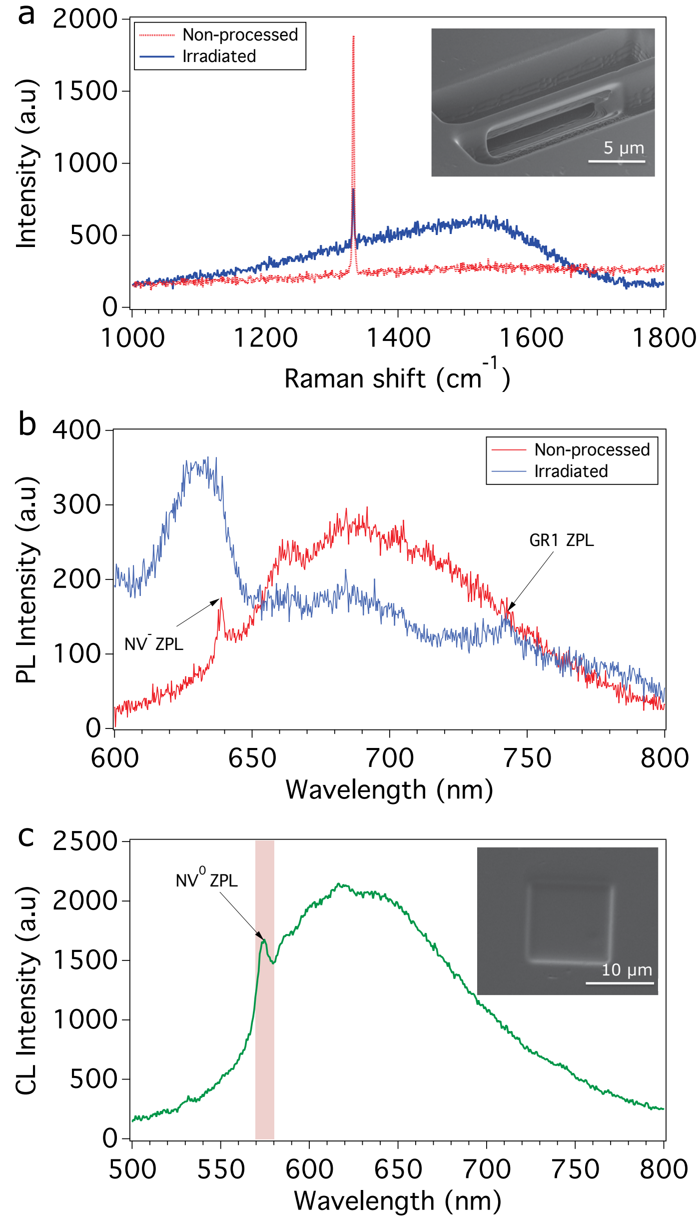

FIGURE 6.1: Optical quality of diamond structures fabricated using a focused oxygen ion beam. a) Raman spectra of non-processed diamond and a bridge structure (shown in the inset) fabricated using 30 keV oxygen ions. b) PL spectra of non-processed diamond and the bridge. c) CL spectrum obtained using a 15 keV electron beam of a region of diamond (shown in the inset) irradiated by 30 keV oxygen ions.

The bridge exhibits a broad Raman scattering profile, similar to that found in amorphous carbon [243] (we note that the diamond line at 1332 cm^{-1} originates from non-processed

diamond located underneath the ion induced damage layer [138]). PL from the bridge is characterised by significant quenching of the negative nitrogen-vacancy (NV^-) emission, an intense broad-band emission that overlaps with the NV^- zero phonon line (ZPL), and the neutral vacancy defect 'GR1' ZPL which is characteristic of ion bombarded diamond [244].

To determine the range of damage in diamond caused by oxygen FIB milling, a series of boxes were fabricated at normal incidence. Boxes were fabricated with ion energies of 2, 8, 16 and 30 keV (and fluences of 5, 27, 27 and 27 nC μm^2 respectively). Constant power CL depth profiling [167, 168] of the NV^0 colour centre was used to examine the ion induced damage layers. Conveniently, the NV^0 emission probed by CL does not overlap with the additional defect-related emissions seen in PL spectra (Figure 6.1b), as illustrated by the CL spectrum shown in Figure 6.1c.

Figure 6.2a shows NV^0 CL depth profiles obtained from non-processed diamond and regions milled by 2, 8, 16 and 30 keV oxygen ions. The NV^0 emission intensity was measured as a function of electron beam energy using an electron beam power of 40 μW, and a 10 nm bandpass centred on 575 nm (see Figure 6.1c). To correlate the electron beam energy with the maximum CL generation depth, the electron energy deposition profiles shown in Figure 6.2b were simulated using standard Monte Carlo models [170] of electron-solid interactions. The curves in Figure 6.2b are approximately proportional to CL generation profiles within the electron interaction volume [167] in diamond and show how the maximum CL generation depth scales with beam energy.

The CL depth profiles in Figure 6.2a show that the NV^0 emission is quenched within a near-surface region whose thickness increases with the energy of the oxygen ions. To quantify the thickness of this damaged region, we used the x-intercept of each dataset in Figure 6.2a as a measure of the electron beam energy that corresponds to the onset of NV^0 emission. At energies lower than the onset, the CL generation volume is contained within the damaged near-surface region where the NV^0 emission is quenched. For example, in the case of diamond milled by 30 keV oxygen ions, the NV^0 emission onset is observed at an electron beam energy of 8 keV, which corresponds to a maximum CL generation depth of 500 nm (see Figure 6.2b). Hence, the first 500 nm of the diamond is comprised of damaged,

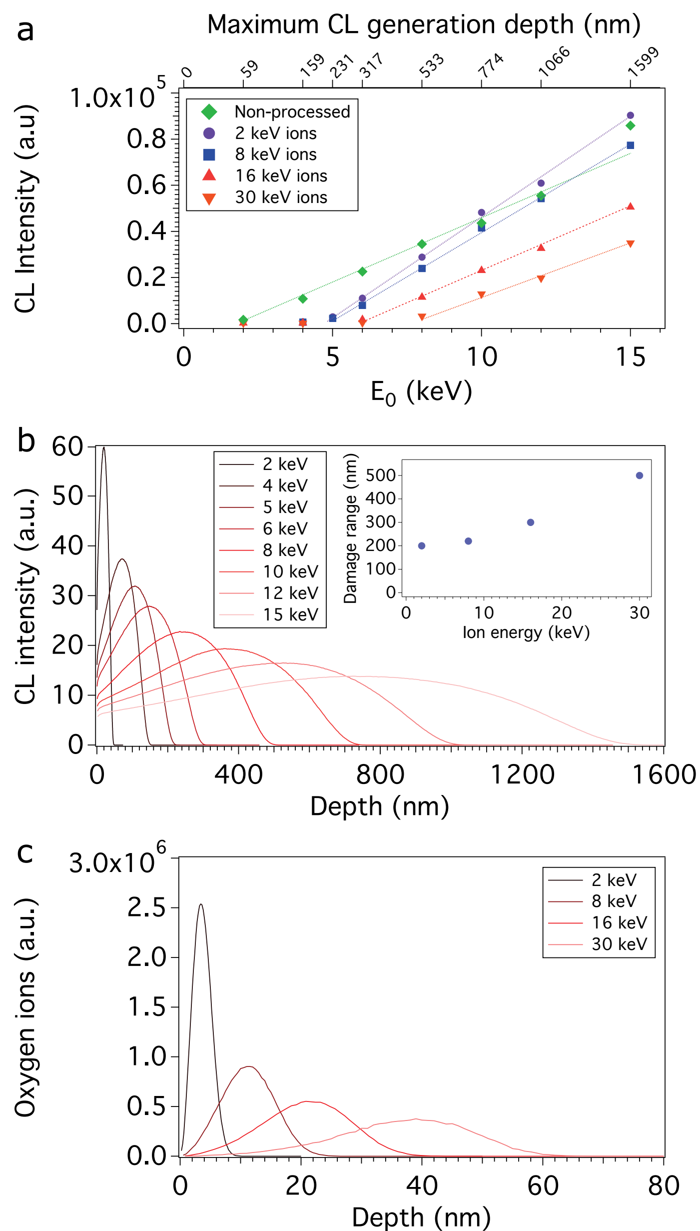

FIGURE 6.2: Profiling of oxygen ion induced damage in diamond. a) CL depth profiles measured from non-processed single crystal diamond and regions milled by 2, 8, 16 and 30 keV oxygen ions. b) CL generation profiles simulated for the electron beam energies used for CL depth profiling. *Inset:* Depth of damage in single crystal (100) diamond as a function of oxygen ion energy determined using the data shown in (a) and (b). c) Depth distributions of oxygen implanted in amorphous carbon simulated using SRIM for ion energies of 2, 8, 16 and 30 keV.

non-luminescent material. This method was applied to all four regions irradiated by oxygen ions to determine the damage range, shown in the inset of Figure 6.2b, as a function of oxygen ion energy. We note that 'non-processed' diamond also displays quenching of the

NV^0 emission within the first $\sim$ 50 nm of surface material. We ascribe this damage layer to non-luminescent defects produced by oxygen neutrals that spray the sample during FIB processing.

A minimum spot size diameter of $\sim$ 15 nm for a 30 keV (Xe) ion beam generated by an ICPS system has been reported [77]. However, the oxygen ion interaction volume in diamond decreases the resolution for fabrication to $\sim$ 500 nm, thereby limiting the practical use of a focused 30 keV oxygen ion beam to micropatterning. The oxygen ion interaction volume can be reduced by reducing the ion beam energy. However, a significant reduction in energy is at present not optimal due to broadening of the ion beam caused by existing ICPS FIB systems. This beam broadening greatly increases the ion beam spot size, making the fabrication of structures such as the undercut bridge impractical at energies much lower than 30 keV. This is however, a technological issue, that will likely be resolved in the coming years.

The range of damage generated by oxygen ions (inset of Figure 6.2b) is significantly greater than that produced by gallium ions (e.g. at 30 keV, oxygen ions give rise to a damage range of 500 nm, whereas Ga^+ FIB milling of diamond has been observed experimentally to generate a damage layer thickness of 46 nm [147]). To determine the reason behind the large damage range of oxygen ions, we compare the CL depth profiles to the range of O^+ ions in amorphous carbon simulated using SRIM [172] and the properties of diamond (density = 3.515 g cm^{-3}, displacement energy = 40 eV [230]).

Oxygen ion implantation depth distributions simulated for ion energies of 2, 8, 16 and 30 keV are shown in Figure 6.2c. Here we plot the range of oxygen ion implantation and not the range of vacancies induced by ions as we cannot exclude the possibility of an oxygen related non-radiative centre quenching NV emission. The two ranges however, are nearly identical in this ion energy range. At 30 keV, O ions penetrate to a depth of $\sim$ 60 nm in amorphous carbon material, which is significantly smaller than the damage range of 500 nm found by CL depth profiling of single crystal diamond. We ascribe this difference between SRIM and experimental results primarily to channelling of O ions in the single crystal diamond structure (which is neglected by the binary approximation model implemented in SRIM). Swelling of the material due to ion implantation [245] is a potential

secondary cause of the thick damage layers. At the ion energies used here, channelling of ^{15}N in diamond displays a similar difference between simulated and experimental data [246]. Channelling can be minimised by sample tilting. However, this is not optimal for the fabrication of arbitrary structure geometries, and the effectiveness and applicability of this method decreases with decreasing ion energy [247] and ion mass [248, 249] due to corresponding increases in the critical angles for channelling.

Next, we turn to post-fabrication removal of the damage layer generated by oxygen ions. Previously, some methods have been shown to remove amorphous material from diamond damaged by Ga^+ FIB milling [148, 149]. The ultimate goal of such post-processing treatments is complete, localised removal of the damaged layer and impurities implanted by the ion beam without the need for harsh chemical treatments that can be detrimental to hybrid diamond-based devices. H_2O-mediated EBIE is a nanoscale, localised dry chemical etch technique [42, 177] that volatilises carbon, and does not compromise the luminescent properties of single crystal diamond [178] (currently, no EBIE method exists for the removal of implanted gallium impurities). We applied H_2O-mediated EBIE to a region of diamond that had been milled by 30 keV focused oxygen ions. The milled area was imaged ex situ using an atomic force microscope (AFM), which shows that $\sim$ 70 nm of material was removed by EBIE (Figure 6.3).

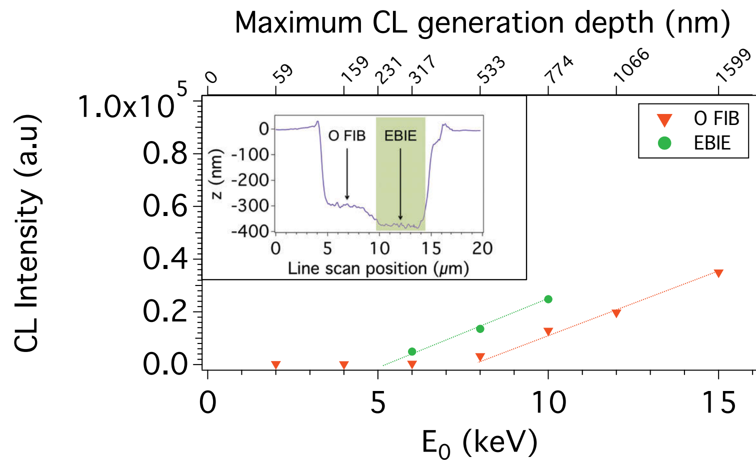

FIGURE 6.3: Removal of damaged material by EBIE. CL depth profile measured from a region milled by a 30 keV oxygen FIB before ('O FIB') and after EBIE was used to remove $\sim$ 70 nm of surface material ('EBIE'). *Inset:* AFM line scan across measured region.

CL depth profiles were obtained from the oxygen FIB milled and EBIE polished regions. The region etched by EBIE displays greatly enhanced CL emission when compared to the as milled region (Figure 6.3). While only 70 nm of material was removed from the 500 nm damage layer, the CL depth profile from the resulting region yields a damage layer thickness of $\sim$ 250 nm. We tentatively ascribe this discrepancy to partial recovery of material swelling and of damage caused by ion channelling by the high fluence electron beam irradiation treatment used for EBIE. Qualitatively, our results show that EBIE does not induce further amorphisation of the underlying pristine diamond and that it is a viable technique for removing damage layers generated by oxygen ions.

6.4 Conclusions

In summary, we have characterised the damage induced in single crystal (100) diamond during maskless milling with a focused oxygen ion beam. The thickness of a damage layer in which NV centre luminescence is quenched is shown to be significantly greater than the oxygen implantation range predicted by Monte Carlo binary approximation models. We ascribe the difference to channelling and volume expansion of the milled region. The damage layer can be removed by H_2O-mediated electron beam induced etching of carbon.

6.5 Methods

Bridge fabrication. The structure was fabricated by milling two 25 $\times$ 5 μm boxes separated by 2 μm using a 30 kV oxygen ion beam incident normal to the diamond. The gap was then undercut by milling at 45° until visual endpoint, rotating the sample through 180° and then milling further until visual endpoint.

Optical measurements. Raman measurements were performed using a Renishaw inVia Raman microscope with a 633 nm excitation laser. PL measurements were performed at room temperature using a custom confocal microscope with a 532 nm excitation laser. CL measurements were performed at room temperature using a FEI Quanta 200 scanning electron microscope (SEM) equipped with a Gatan parabolic CL collection mirror. The

mirror was positioned above the sample and directed the emitted light to a Hamamatsu charge-coupled device (CCD).

Removal of material by EBIE. EBIE was performed at room temperature using a Quanta 200 variable pressure [95] SEM, a H_2O pressure of 100 Pa, and a focused, 25 keV, 8.3 nA electron beam scanned over an area of 5 × 10 μm for 45 minutes (primary electron fluence = 2.8×10^{20} cm^{-2}). The milled area was imaged ex situ using the tapping mode of a Digital Instruments Dimension 3100 AFM, and analysed using the software package Gwyddion [158].

Author Contributions

Aiden Martin, Steven Randolph, Aurelien Botman, Milos Toth and Igor Aharonovich designed the project. Aiden Martin, Steven Randolph, Aurelien Botman and Igor Aharonovich performed the experiments. All authors analysed the data and contributed to the writing of the manuscript.

Chapter 7

Cryogenic Electron Beam Induced Chemical Etching

7.1 Abstract

Cryogenic cooling is used to enable efficient, gas-mediated electron beam induced etching (EBIE) in cases where the etch rate is negligible at room and elevated substrate temperatures. The process is demonstrated using nitrogen trifluoride (NF_3) as the etch precursor, and Si, SiO_2, SiC and Si_3N_4 as the materials volatilised by an electron beam. Cryogenic cooling broadens the range of precursors that can be used for EBIE, and enables high resolution, deterministic etching of materials which are volatilised spontaneously by conventional etch precursors as demonstrated here by NF_3 and XeF_2-mediated EBIE of silicon.

7.2 Introduction

EBIE enables maskless, beam-directed editing of materials at the nanoscale. Etching has been demonstrated using precursors such as H_2O, O_2, H_2, Cl_2, SF_6, XeF_2 and ClF_3 [1, 26, 27, 177]. However, the range of precursor-substrate combinations that is appropriate for EBIE has, to date, been small compared to conventional plasma etching [68, 69]

because many of the precursors that yield radicals responsible for plasma etching have properties that are undesirable for EBIE. Ideally, a substrate etched by EBIE is exposed to a vapor-phase precursor that adsorbs to, but does not etch the material spontaneously. An electron beam is then used to dissociate surface-adsorbed precursor molecules, generating fragments that react with the substrate to produce species which desorb, thereby volatilising substrate regions near the beam [1] (see inset of Figure 7.1a). EBIE is typically performed at room temperature because both heating and cooling can inhibit etching by increasing and decreasing the thermal desorption rate of surface-adsorbed precursor molecules and the final reaction products, respectively.

The limited scope of room temperature EBIE is exemplified by NF_3, a common fluorine precursor used in laser [85] and plasma [86] induced etching of Si and SiC [87]. NF_3 satisfies most key requirements for EBIE: it has a large electron dissociation cross-section [88]; high vapour pressure; relatively low toxicity and broad material compatibility (in particular, NF_3 does not cause corrosion of components in electron microscope chambers, and does not etch most solids spontaneously, including silicon [89]). Despite these favorable characteristics, NF_3-mediated EBIE has previously not been demonstrated, likely due to poor surface coverage at room temperature. Weak physisorption has been observed on platinum [250], gold (desorption energy = 0.219 eV) [251] and ruthenium [252]. Standard theory of EBIE processing [1, 26, 28, 42, 44, 46, 91–94] predicts that the low NF_3 adsorption energies (on the order of 200 meV) give rise to very low etch rates at and near room temperature (Supporting Information Section 7.6.3). Coverage can, in principle, be increased by substrate cooling since the desorption rate decreases exponentially with reciprocal temperature (Supporting Information 7.6.3). Cooling does, however, also inhibit thermal desorption of the final reaction products, and has therefore not been used to enhance EBIE.

Here we show that cryogenic substrate cooling can enable efficient EBIE in cases where the room temperature etch rate is negligible. We demonstrate efficient EBIE of materials that contain Si, C, N and O at temperatures as low as 100 K. The results show that a range of EBIE reaction products can desorb (during electron irradiation) at cryogenic substrate temperatures, and that cryogenic substrate cooling broadens the range of precursors that can be used to realise EBIE. NF_3-mediated EBIE of Si is particularly significant because

silicon is most often etched using XeF_2 which gives rise to spontaneous etching and roughening of Si, while the electron beam merely accelerates the local etch rate [22]. The only alternatives for EBIE of Si reported to date are SF_6 [25], which is highly inefficient, and Cl_2 [23, 24] which is highly corrosive, toxic and flammable. Cryogenic, NF_3-mediated EBIE overcomes these problems, and enables deterministic, high-resolution editing of Si and associated devices.

7.3 Methods

EBIE was carried out using an FEI Nova NanoSEM variable pressure [95, 253] scanning electron microscope (SEM) equipped with a magnetic immersion lens gaseous secondary electron detector [150] and a liquid nitrogen cooling stage. Substrates used for EBIE were Si, SiO_2, SiC and Si_3N_4. Cylindrical etch pits were fabricated under 8.4 Pa of NF_3 using a stationary, 10 keV, 3.4 nA electron beam that was under-focused to generate a top-hat flux profile (see Supporting Information Sections 7.6.1a and b for additional details). This configuration, shown schematically in the inset of Figure 7.1, yields conditions that are optimal for quantitative analysis of EBIE rates [14, 28, 94, 177]. The temperature was always above the condensation point of the precursor gas (Supporting Information Section 7.6.1c), in contrast to ice lithography and cryogenic electron beam induced deposition [254–257].

Comparisons to Cl_2-mediated EBIE of Si (Figure 7.3a) were performed using the electron exposure conditions used by Roediger et. al. [23, 24], an NF_3 pressure of 6.5 Pa and a substrate temperature of 106 K. Delocalised etching of Si caused by XeF_2 precursor vapor (Sigma Aldrich, 99.99 %) was demonstrated (Figure 7.3b) using a gas injection capillary located ~ 100 μm from the substrate surface in high vacuum ($\sim 3.8 \times 10^{-3}$ Pa), at room temperature (Supporting Information Section 7.6.1d). A framed 'NF3' symbol (Figure 7.4) was etched into Si by a 20 keV, 9.9 nA electron beam, using an NF_3 pressure of 6.5 Pa and a substrate temperature of 106 K. Total processing time was 5 minutes with an electron beam dwell time of 13 ms per pixel.

7.4 Results and Discussion

Figures 7.1a and b show plots of the depth of pits made in Si (measured using an atomic force microscope (AFM), see Supporting Information Section 7.6.1f) by NF_3-mediated EBIE as a function of temperature (T). The etch rate is negligible at room temperature and increases as the substrate temperature is reduced to $\sim$ 98 K. At any given temperature, the etch rate is constant with time (over the experimental time scale), as seen in Figure 7.2.

Figure 7.1b shows that the etch rate scales exponentially with $\frac{1}{T}$ at reciprocal temperatures greater than $\sim$ 0.0075 K^{-1}. At lower values of $\frac{1}{T}$ (i.e. higher temperatures), EBIE is inhibited through a thermally-activated mechanism that we ascribe tentatively to surface

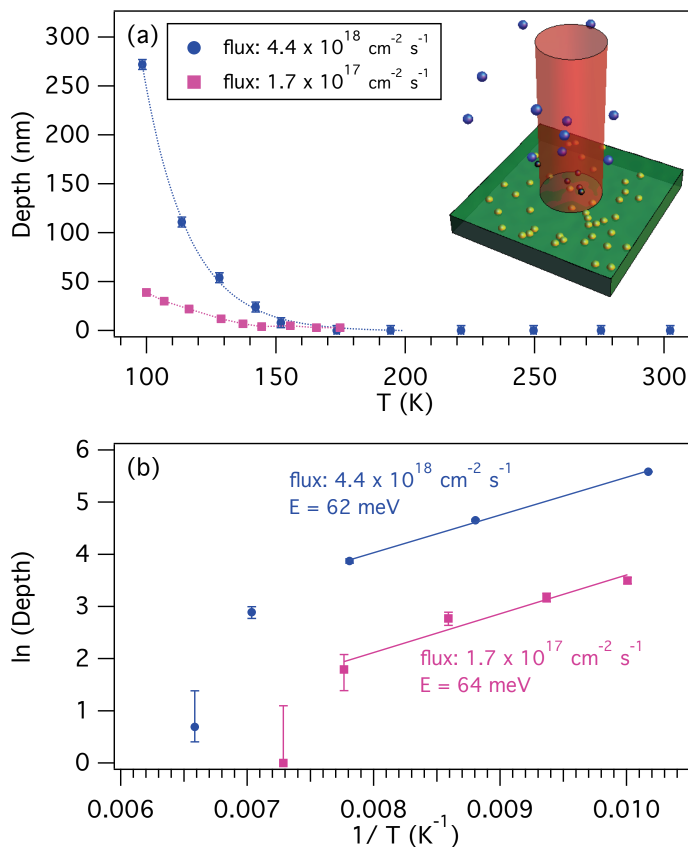

FIGURE 7.1: a) Etch pit depth versus substrate temperature (T) for NF_3-mediated EBIE of Si. b) Plots used to extract the activation energies E by Arrhenius analyses of the data in (a). *Inset:* Schematic illustration of EBIE performed using a stationary beam defocused to attain a top-hat electron flux profile.

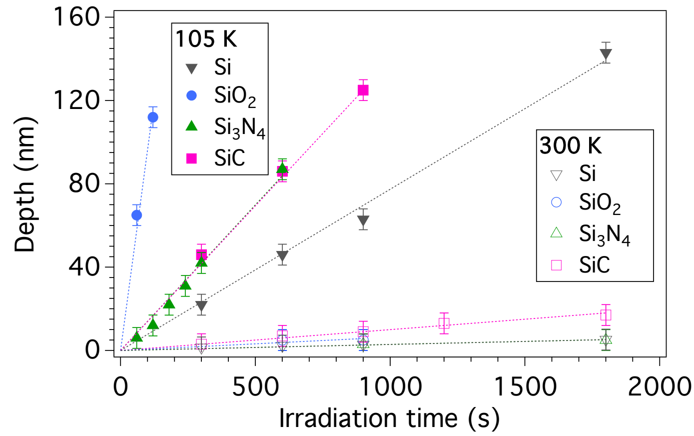

FIGURE 7.2: Etch pit depth versus time measured for Si, SiO_2, SiC and Si_3N_4 etched by NF_3-mediated EBIE at substrate temperatures of 105 and 300 K.

diffusion of residual contaminants (such as hydrocarbons and H_2O) [40, 258] present at the substrate surface. Residual contaminants compete for surface sites with NF_3 adsorbates and can therefore inhibit EBIE, particularly at elevated temperatures where the NF_3 coverage is low and diffusivity (of all species at the surface) is relatively high.

At reciprocal temperatures greater than ~ 0.0075 K^{-1}, the exponential increase in etch rate with $\frac{1}{T}$ is attributed to a corresponding increase in the surface coverage of NF_3 caused by a decrease in the NF_3 residence time at the substrate surface (Supporting Information Section 7.6.3). We note that an exponential increase in EBIE rate with $\frac{1}{T}$ can not be explained by the temperature-dependence of the adsorbate diffusion coefficient which decreases with $\frac{1}{T}$ (Supporting Information Section 7.6.3).

In our experiments, analysis of the EBIE reaction products by mass spectrometry was not possible due to the high NF_3 pressure and small quantity of volatile molecules generated in EBIE. However, based on other dry chemical etch processes [259], and XeF_2-mediated EBIE of Si [260], the etch reaction products are most likely of the form SiF_n, where $n = 1$ to 4, and the thermal desorption rate increases as n $\rightarrow$ 4 [261].

The etch pit depth data shown in Figure 7.1b can be used to extract the thermal activation energy (E) of the process responsible for the observed temperature dependence. Arrhenius analyses of the curves yield an activation energy of $\sim 63 \pm 1$ meV for EBIE performed using electron fluxes of 1.7×10^{17} cm^{-2}s^{-1} and 4.4×10^{18} cm^{-2}s^{-1}, respectively. This

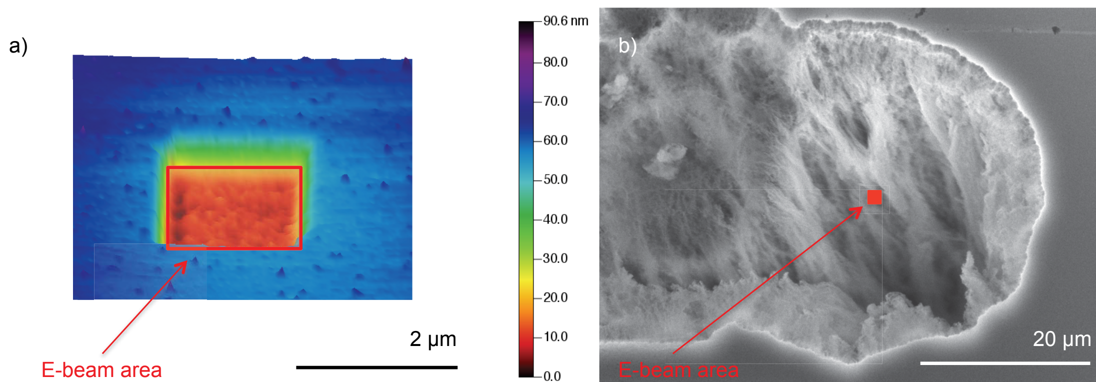

FIGURE 7.3: a) AFM image of a rectangular pit made in Si by NF_3-mediated EBIE, illustrating the absence of delocalised damage produced by spontaneous etching of Si. b) SEM image of Si processed by XeF_2-mediated EBIE using the same electron exposure parameters as those used in (a). Red rectangles show the areas that were scanned by the electron beam and correspond to the nominal areas of etch pits made by EBIE. The image in (b) shows delocalised damage caused by spontaneous etching of Si by XeF_2 that occurred during EBIE.

value of E serves as a lower limit for the adsorption energy of NF_3, as discussed in the Supporting Information (Sections 7.6.4 and 7.6.5).

NF_3-mediated EBIE was also applied to silicon oxide, carbide and nitride to determine the etch efficiency of materials other than Si. The etch rates of all three compounds are very low at room temperature, and increase significantly at the cryogenic temperature of 105 K, as seen in Figure 7.2. The volumetric etch rates at cryogenic temperature are 9.1×10^4, 1.1×10^6, 1.6×10^5 and 1.6×10^5 nm^3 s^{-1} for Si, SiO_2, Si_3N_4 and SiC, respectively. SiO_2 exhibited the highest volumetric etch rate, likely due to the existence of additional reaction pathways enabled by oxygen, such as the generation of $SiOF_2$ [262] and OF species [263], and a lower concentration of silicon atoms in the material.

In the case of SiO_2 and Si_3N_4, the desorption of nitrogen and oxygen is not surprising at cryogenic temperatures. However, the carbon present in SiC needs to be volatilised by radicals produced by electron dissociation of NF_3 adsorbates. The volatile reaction products are most likely of the form CF_x (where x = 1 to 4).

Next, we compare the efficacy of the cryogenic NF_3 etch process to room temperature alternatives reported to date in the EBIE literature. Electron exposure conditions used by Roediger et. al. for Cl_2-mediated EBIE of Si [23, 24] were replicated using XeF_2 and

NF_3. The use of XeF_2 results in highly delocalised damage, caused by rapid spontaneous etching of Si. For example, Figure 7.3b shows a substrate region that contains an etch box with a nominal area of 1.5×1.5 μm, and a region of severe damage produced by XeF_2 that extends $\sim$ 20 μm from the rectangle scanned by the beam. Such rapid, delocalised etching by XeF_2 is typical when the native oxide layer is compromised (by pinhole defects, or by EBIE). This behavior is clearly unfavorable as it inhibits the ability to etch Si with high spatial resolution (Supporting Information Section 7.6.1e). In comparison, NF_3-mediated EBIE did not give rise to any observable spontaneous etching of the Si substrate. Instead, it yielded a well defined etch pit with a depth of $\sim$ 55 nm (Figure 7.3a), and a volumetric etch rate that is $\sim$ 2.4 times greater than that of Cl_2 under the same electron exposure conditions.

A complex pattern etched into Si using NF_3 is shown in Figure 7.4. It demonstrates high resolution, localised editing of Si in the absence of highly toxic, flammable and corrosive precursors that are unsuitable for use in electron microscopes (ultimate EBIE resolution is governed by the electron beam diameter, proximity effects and material roughening that occurs during etching) [2]. We note that SF_6 has also been reported as a precursor for room temperature EBIE of Si [25]. This etch process is, however, extremely inefficient and inappropriate for high resolution EBIE, and may give rise to unintended deposition of sulfur [84].

7.5 Conclusions

In summary, cryogenic cooling was used to enable efficient EBIE using NF_3 as the etch precursor. The etch rate is limited by thermal desorption of weakly bound NF_3 adsorbates. The process was demonstrated using Si, SiO_2, SiC and Si_3N_4, and enables high resolution EBIE in the absence of artifacts caused by delocalised spontaneous etching of the substrates.

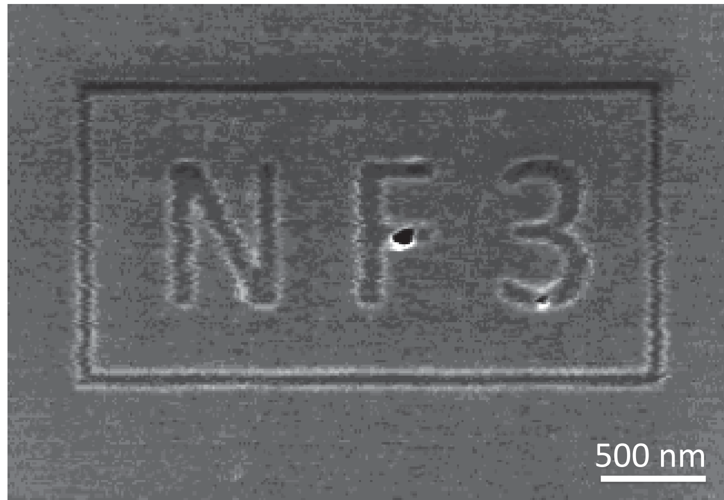

FIGURE 7.4: SEM image of a framed 'NF3' symbol etched into Si by NF_3-mediated EBIE with a line resolution of $\sim$ 85 nm.

7.6 Supporting Information

7.6.1 Notes

a) Substrates used for EBIE were Si [(111), p-type, 5-10 ohm cm], thermally grown SiO_2 (119 nm on Si), SiC [4H, (0001)] and Si_3N_4 (100 nm on Si). The substrates were cleaned by sonication for 30 minutes each in acetone, isopropyl alcohol and Milli-Q H_2O. Si was cleaned further using piranha etch (H_2SO_4:H_2O_2, 3:1) and $\sim$ 5 % HF solutions in order to remove residual hydrocarbons and surface oxide layer.

b) In order to perform NF_3-mediated EBIE, the SEM chamber was first evacuated to a base pressure of 3×10^{-4} Pa (3×10^{-6} mBar). NF_3 gas (99.995%, Advanced Speciality Gases) was then flown into the variable pressure SEM chamber at a rate needed to yield a steady state pressure of 8.4 Pa (i.e. a molecular flux of $\sim$ 1.5×10^{19} cm^{-2} s^{-1} at a gas temperature of 298 K). The temperature dependence of EBIE (Figure 7.1) was investigated using an electron irradiation time of 30 minutes, and electron fluxes of 1.7×10^{17} cm^{-2}s^{-1} (beam diameter, $d \sim 3989$ nm) and 4.4×10^{18} cm^{-2}s^{-1} ($d \sim 785$ nm). The time dependence (Figure 7.2) was characterised using an electron flux of 2×10^{18} cm^{-2}s^{-1} ($d \sim 1226$ nm)

at room temperature and 105 ± 3 K.

c) The condensation point of NF_3 was found by detecting a rapid decrease in the electron microscope chamber pressure during cooling. Condensation occurred at a substrate temperature of ∼ 90 K and a NF_3 pressure of 8.4 Pa (we note that the NF_3 likely condensed on the coolant delivery lines which reach a lower temperature than the substrates).

d) Comparisons to Cl_2-mediated EBIE of Si were performed using an electron beam energy and current of 20 keV and 9.9 nA, scan area of 1.5 × 1.5 μm^2, etch time of 20 minutes, and a dwell time per pixel of 1.68 ms.

Comparisons to XeF_2-mediated EBIE of Si were done using the capillary gas injection method because it localises the chamber volume that contains an elevated pressure of precursor gas [264, 265]. The alternative approach of filling the low vacuum SEM chamber [2] with XeF_2 could not be used for this comparison because XeF_2 causes rapid, delocalised decomposition of Si through the spontaneous etch process.

e) We note that strategies exist to locally suppress spontaneous etching by XeF_2. However, these involve modification of large areas of the Si substrate and are affected by subsequent exposure to an electron beam (e.g. during electron imaging used to monitor EBIE) [83].

f) Etch pit depths were measured ex situ using the tapping mode of a Digital Instruments Dimension 3100 AFM, and analysed using the software package Gwyddion [158]. Error bars (in Figures 1 and 2) account for measurement uncertainty and are dominated by the accuracy of substrate temperature measurements, thermal drift and the effects of surface roughness on AFM image analysis. In cases where no bars are shown, the marker size is smaller than the measurement uncertainty.

7.6.2 Modelling Introduction

In the following we use standard models of EBIE to elucidate: (i) the mechanism through which the EBIE rate is increased in cryogenic EBIE [Section 7.6.3], (ii) Arrhenius analysis

of single step EBIE reactions [Section 7.6.4], and (iii) Arrhenius analysis of a multistep reaction process such as NF_3-mediated EBIE of Si [Section 7.6.5].

7.6.3 Temperature Dependence of EBIE

The rates of electron beam induced etching and deposition typically scale with the concentration of surface-adsorbed precursor molecules (N_a), which can be found by solving rate equations of the form [1, 26, 28, 42, 44, 46, 92–94, 177, 191]:

$$\frac{\partial N_a}{\partial t} = \Lambda - \frac{N_a}{\tau} - \frac{\partial N_\alpha}{\partial t} + D_a \nabla^2 N_a, \tag{7.1}$$

where α represent surface-adsorbed fragments (e.g., F^*) produced by electron induced dissociation of the precursor molecules. $\frac{\partial N_a}{\partial t}$ is given by a sum of fluxes representing precursor adsorption ($\Lambda = sF(1-\Theta)$), desorption ($\frac{N_a}{\tau}$), electron induced dissociation ($\frac{\partial N_\alpha}{\partial t}$) and surface diffusion ($D_a \nabla^2 N_a$). N is number density at the surface, τ is the adsorbate residence time, F is the gas molecule flux incident onto the substrate, s is the sticking coefficient, Θ is adsorbate surface coverage (which is typically limited to 1 monolayer by the Langmuir isotherm, $\Theta = AN_a$), A is the area of a single surface site, and D_a is the diffusion coefficient [1, 26, 28, 42, 44, 46, 92–94, 191].

The rate of change of concentration of the reactive fragments α at the substrate surface is given by:

$$\frac{\partial N_\alpha}{\partial t} = \sigma f N_a, \tag{7.2}$$

where f is electron flux and σ is the effective [94] cross-section for the generation of fragments that volatilise the substrate. The EBIE rate scales with $\frac{\partial N_\alpha}{\partial t}$ (except for special cases where it is limited by the concentration of active sites at the surface [94], or by the re-dissociation of etch reaction products [92]).

Substrate cooling affects Equation 7.1 (and hence the etch rate) primarily through the dependencies of τ and D_a on temperature (T) [1, 42, 46]:

$$\tau = \tau_0 Exp\left(\frac{E_a}{k_b T}\right), \tag{7.3}$$

$$D_a = D_0 Exp\left(\frac{-E_{diff}}{k_b T}\right), \tag{7.4}$$

where E_a and E_{diff} are the activation energies for thermal desorption and diffusion of the adsorbates, τ_0 and D_0 are the respective pre-exponential factors, and k_B is Boltzmann's constant. From these relationships, the adsorption time and diffusion rate increase and decrease with reciprocal substrate temperature, respectively. Hence, sample cooling can not cause an increase in the EBIE rate through the dependence of D on T since the rate of precursor replenishment through diffusion decreases with reciprocal T. Cooling can, however, cause an increase in the etch rate through the dependence of τ on T. Specifically, τ causes N_a to increase with $\frac{1}{T}$ (up to a maximum value defined by the adsorption isotherm), and the etch rate is proportional to N_a (Equation 7.2). Hence, we ascribe our observed increase in measured EBIE rates with reciprocal substrate temperature to a corresponding increase in the adsorbate residence time τ.

7.6.4 Arrhenius Analysis of Single Step EBIE Reactions

Arrhenius analysis of EBIE rates can, in principle, be used to obtain E_a if the diffusion term in Equation 7.1 is negligible (i.e. if the temperature-dependence of D_a does not play a role in EBIE). This condition is satisfied in the so-called 'reaction-rate limited' (RRL) regime, where the extent of local adsorbate depletion caused by $\sigma f N_a$ is negligible and Equation 7.1 simplifies to [1, 26, 42]:

$$\frac{\partial N_a}{\partial t} = sF(1 - AN_a) - \frac{N_a}{\tau} - \sigma f N_a. \tag{7.5}$$

Hence, in the RRL regime, the precursor adsorbate concentration (N_a) and the rate of change of etch pit depth with time $\left(\frac{\partial z}{\partial t}\right)$ are given by [1, 42]:

$$N_a = \frac{sF}{sFA + \frac{1}{\tau} + \sigma f}, \tag{7.6}$$

$$\frac{\partial z}{\partial t} = V_\gamma \sigma f N_a, \tag{7.7}$$

where V_γ is the volume of a single molecule removed from the substrate in the etch reaction. Combining (7.6) with (7.7) and integrating yields an expression for the time-evolution of the etch pit depth (z):

$$z = V_\gamma \sigma f N_a t \quad (7.8)$$
$$= \frac{V_\gamma \sigma f s F t}{sFA + \frac{1}{\tau} + \sigma f}, \quad (7.9)$$

where sFA is the rate at which gas phase precursor molecules are reflected from occupied surface sites, $\frac{1}{\tau}$ is the precursor desorption rate, and σf is the rate at which surface-adsorbed precursor molecules are consumed in the etch reaction.

The activation energy for thermal desorption (E_a in Equation 7.3) can be obtained by simple Arrhenius analysis of the etch pit depth (or volume) if sFA and σf are both negligible in the denominator of Equation 7.9 (i.e. $\frac{1}{\tau} \gg sFA$, and $\frac{1}{\tau} \gg \sigma f$):

$$ln(z) = -ln\left(\frac{1}{\tau}\right) + ln(V_\gamma \sigma f s F t) \quad (7.10)$$
$$= \frac{E_a}{k_b T} + ln(V_\gamma \sigma f s F t \tau_0). \quad (7.11)$$

Hence, a plot of $ln(z)$ versus $\frac{1}{T}$ yields a straight line with a slope of $\frac{E_a}{k_b}$ (i.e. Arrhenius analysis yields the correct thermal desorption energy E_a). However, this is not the case if sFA and σf are not negligible, in which case Arrhenius analysis can underestimate E_a, as illustrated by the modeling results shown in Figure 7.5 (calculated using Equation 7.9 and the model input parameters listed in Section 7.6.6).

Figure 7.5a shows a plot of $ln(z)$ versus $\frac{1}{T}$ calculated for a number of values of the electron flux f [1]. Each curve is linear at low values of $\frac{1}{T}$, and has a positive slope that yields the correct activation energy E_a of 180 meV (Figure 7.5b). However, the curves saturate (due to surface site saturation by adsorbates) and the respective slopes become zero when $\frac{1}{T}$ is sufficiently large. In this regime, Arrhenius analysis of the etch pit depth (or volume) yields activation energies that are smaller than E_a, as shown in Figure 7.5b. Furthermore, Figure 7.5 shows that the temperature range over which Arrhenius analysis yields the incorrect

[1] We note that, at room temperature (corresponding to a reciprocal temperature of ~ 0.003 K^{-1}), the etch pit depths in Figure 7.5a are negligible because the desorption energy of 180 meV yields a very low adsorbate coverage of $\sim 2 \times 10^{-6}$.

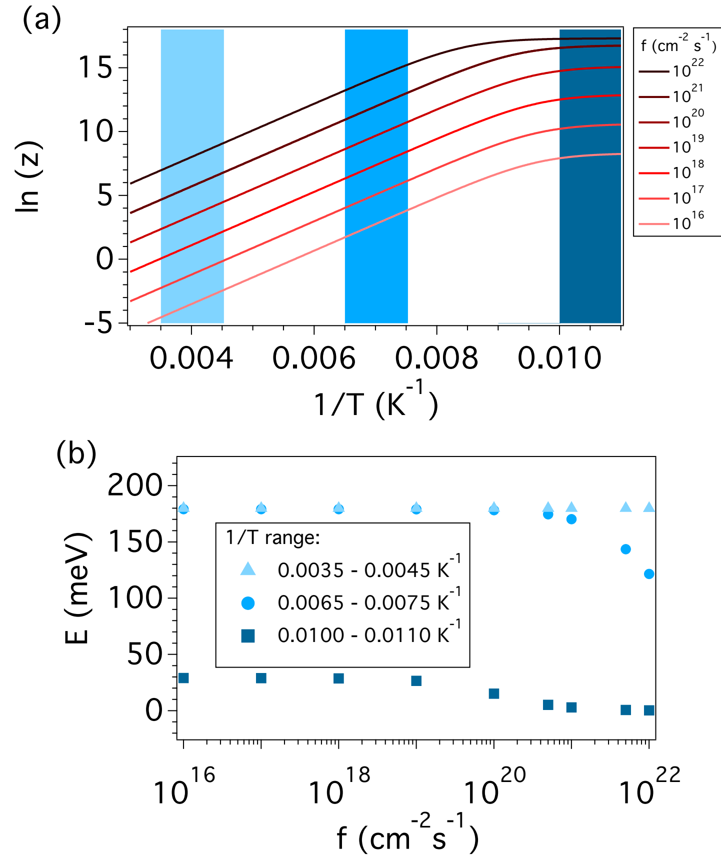

FIGURE 7.5: a) Plot of $ln(z)$ versus $\frac{1}{T}$ calculated for a single step EBIE reaction and a number of values of the electron flux f (10^{16} - 10^{22} cm^{-2} s^{-1}). The calculations were performed using Equation 7.9 and a desorption energy E_a of 180 meV. b) Plot of the activation energy E obtained as a function of f by Arrhenius analysis of the data in (a). The gradient used to obtain E was measured over the reciprocal temperate ranges shown in (a): 0.0035 – 0.0045, 0.0065 – 0.0075 and 0.0100 – 0.0110 K^{-1}.

value of E_a increases with f. The reason for this behavior is apparent in Equation 7.6 which shows that the adsorbate coverage scales inversely not only with $\frac{1}{\tau}$, but also with sFA and σf. When sFA or σf are not negligible, Equations 7.10 and 7.11 are of the form:

$$ln(z) = -ln\left(\frac{1}{\tau} + sFA + \sigma f\right) + ln\left(V_\gamma n \sigma f sFt\right) \quad (7.12)$$

$$= \frac{E_a}{k_b T} - ln\left(\tau_0 e^{\frac{E_a}{k_b T}}(sFA + \sigma f) + 1\right) + ln(V_\gamma n \sigma f sFt\tau_0), \quad (7.13)$$

and simple Arrhenius analysis does not yield E_a.[2]

7.6.5 Arrhenius Analysis of Multistep EBIE Reactions

The calculations in Section 7.6.4 indicate that Arrhenius analysis can be used to obtain E_a under conditions of low adsorbate coverage ($\Theta \ll 1$), and/or low electron flux ($f \lesssim 10^{20}$ cm^{-2}s^{-1} under the EBIE conditions used in the calculations). However, these conclusions are applicable only to single step EBIE reactions. In contrast, EBIE of Si by fluorine radicals is a multistep process that involves a number of possible reaction products [44] (i.e., SiF, SiF_2, SiF_3, and SiF_4), each of which can be dissociated by electrons, and has a characteristic binding energy at the sample surface. For example, SiF_2 can either gain a F to form SiF_3, dissociate to form SiF and F, or it can desorb from the sample surface:

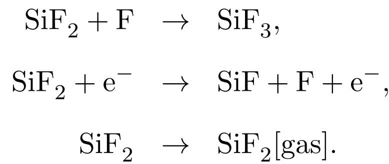

$$\begin{aligned} \mathrm{SiF_2 + F} &\rightarrow \mathrm{SiF_3}, \\ \mathrm{SiF_2 + e^-} &\rightarrow \mathrm{SiF + F + e^-}, \\ \mathrm{SiF_2} &\rightarrow \mathrm{SiF_2[gas]}. \end{aligned}$$

Multistep EBIE reactions can be modeled by solving a coupled set of differential rate equations that account for each adsorbate species at the substrate surface [44]. Hence, based on the approach in Reference 44, we model EBIE of Si by accounting for the precursor molecules N_a, radicals N_α, and the reaction products SiF, SiF_2, SiF_3, and SiF_4:

$$\frac{\partial N_a}{\partial t} = sF(1 - A_a N_a) - \frac{N_a}{\tau} - \frac{\partial N_\alpha}{\partial t}, \tag{7.14}$$

$$\frac{\partial N_\alpha}{\partial t} = \sigma f N_a, \tag{7.15}$$

[2] Furthermore, at values of f greater than $\sim 10^{20}$ cm^{-2}s^{-1} adsorbate depletion becomes significant. Consequently, adsorbate replenishment through diffusion becomes significant [1, 26, 42], and the value of E extracted by Arrhenius analysis is altered by the temperature dependence of the diffusion coefficient D.

$$\frac{\partial N_n}{\partial t} = \begin{cases} \frac{\partial N_\alpha}{\partial t}\frac{N_{(n-1)}}{N_\eta}(1-\Theta_\eta) + \sigma_r f N_{(n+1)} - N_n\left(\frac{1}{\tau_n} + \frac{\partial N_\alpha}{\partial t}\frac{1}{N_\eta}(1-\Theta_\eta) + \sigma_r f\right), & n = 1-3, \\ \frac{\partial N_\alpha}{\partial t}\frac{N_{(n-1)}}{N_\eta}(1-\Theta_\eta) - N_n\left(\sigma_r f + \frac{1}{\tau_n}\right), & n = 4. \end{cases} \tag{7.16}$$

N_n represents the concentrations of SiF, SiF_2, SiF_3 and SiF_4 molecules, σ_r is the cross-section for electron induced scission of the Si–F bond, and τ_n is the residence time of SiF_n:

$$\tau_n = \tau_0 Exp\left(\frac{E_n}{k_b T}\right), \tag{7.17}$$

where E_n is the binding energy of SiF_n. N_η is the concentration of surface sites at which F can bond to a Si atom, and Θ_η is the coverage of surface sites occupied by F:

$$N_\eta = \sum_{m=0}^{3} N_m, \tag{7.18}$$

$$\Theta_\eta = \sum_{n=1}^{4} \frac{1}{n} A_{\text{Si}} N_n. \tag{7.19}$$

The term $\frac{1}{n}A_{\text{Si}}$ limits the concentration of fluorinated Si atoms to one monolayer, m is an integer with lower and upper limits of 0 and 3 because an unfluorinated Si atom (designated by $m = 0$) can react with F to form SiF, whereas SiF_4 (designated by $m = 4$) can not gain an extra fluorine. The integer n is bound by 1 and 4 because the total coverage of sites occupied by F must account for SiF, SiF_2, SiF_3 and SiF_4 species. N_0 is given by:

$$A_{\text{Si}} N_0 = 1 - A_{\text{Si}} N_{\text{Si}}, \tag{7.20}$$

where A_{Si} is the area of a single Si surface site, and N_{Si} is the concentration of fluorinated Si sites:

$$\frac{\partial N_{\mathrm{Si}}}{\partial t} = \sum_{n=1}^{4} \frac{\partial N_n}{\partial t}. \tag{7.21}$$

The vertical etch rate is given by:

$$\frac{\partial z}{\partial t} = V_\gamma \sum_{n=1}^{4} \frac{N_n}{\tau_n}. \tag{7.22}$$

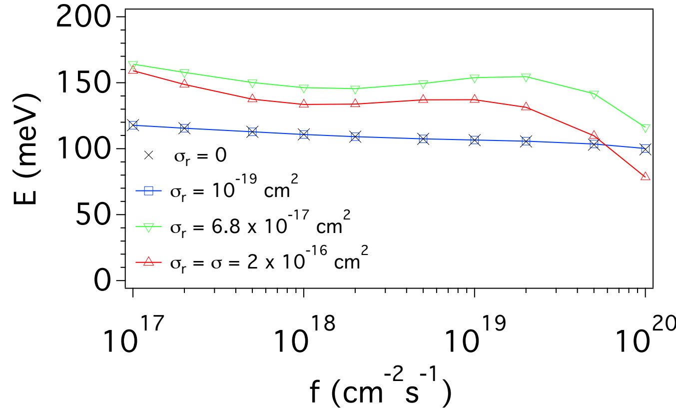

FIGURE 7.6: Plots of the activation energy E versus f for a multistep EBIE reaction obtained by Arrhenius analysis of etch pit depths calculated using Equation 7.22 and a precursor desorption energy of 180 meV. Arrhenius analysis was performed over the reciprocal temperate range used to analyse our experimental data (i.e. 0.008 – 0.010 K^{-1}). The plot is shown for a number of values of the cross-section (σ_r) for electron induced scission of the Si–F bond.

We used the above model to investigate the effects of f and σ_r on the activation energy E obtained by Arrhenius analysis of etch pit depths calculated using Equation 7.22 (the model input parameters are listed in Section 7.6.6). Figure 7.6 shows plots of E versus f calculated over the reciprocal temperate range used to analyse our experimental data (i.e. 0.008 – 0.010 K^{-1}), values of f greater than 10^{17} $cm^{-2}s^{-1}$, and values of σ_r in the range of 0 and σ. In our experiments, values of f lower than $\sim 10^{17}$ $cm^{-2}s^{-1}$ yielded etch rates that were too low to perform accurate measurements of etch pit depths. Similarly, values of $\frac{1}{T}$ lower than ~ 0.0075 K^{-1} yielded etch rates that were very low, and did not scale exponentially with $\frac{1}{T}$ (see Figure 7.1b).

The calculation results can be summarised as follows:

- The activation energy E obtained by Arrhenius analysis of the etch pit depth is always lower than the precursor desorption energy E_a.

- The existence of multiple reaction products SiF_n affects E even if the electron re-dissociation rate of these molecules is negligible (i.e. if $\sigma_r \leq 10^{-19}$ cm^2). This is a consequence of the fact that the reaction products SiF_n compete for surface sites and for F radicals generated by the electron beam.

- If the electron re-dissociation rate of the reaction products is significant (e.g. if $\sigma_r \geq 10^{-17}$ cm^2), it can cause a local increase or a decrease in $E(f)$. The behavior at any given value of f depends on the net effect of a small change in f on the dissociation rate of the precursor molecule adsorbates and that of each SiF_n species at the substrate surface.

The overarching qualitative implication for experimental EBIE is that Arrhenius analysis of the etch pit depth yields activation energies that are lower than the precursor desorption energy E_a. Qualitatively, this result is insensitive to the exact values of the model input parameters (listed in Section 7.6.6). Conversely, the magnitude of the underestimate depends on the absolute values of the input parameters. The availability and accuracy of the latter is presently limited, as has been discussed in detail elsewhere [1].

7.6.6 Model Input Parameters

The data in Figure 7.5 were calculated using the following model input parameters:

- $V_\gamma = 16.6$ Å^3 (volume of a Si atom),

- $A_a = 14.8$ Å^2 (estimated surface area of NF_3 on Si),

- $\sigma = 2$ Å^2 (estimated from the dissociative electron attachment [266] and dissociative electron ionisation cross-sections [88]),

- $s = 1$ (assuming a sticking probability of one),

- $F = 1183.31$ Å^{-2} s^{-1} (calculated using the NF_3 pressure used in our experiments),

- $t = 1800$ s (etch time used in experiments),
- $\tau_0 = 10^{-13}$ s (the reciprocal attempt frequency typically used in analyses of desorption kinetics [184]),
- $E_a = 180$ meV (this value yields good agreement between our modeling results and experimentally observed EBIE rates).

The data in Figure 7.6 were calculated using the above and the following input parameters:

- $A_n = V_\gamma^{\frac{2}{3}}$ (approximate area of a silicon surface site),
- $E_n = 260$, 230 and 200 meV for SiF_2, SiF_3 and SiF_4 (i.e. $n = 2, 3, 4$) respectively [261]. The value for SiF_2 is known, while the rest are estimates based on the observations of Vugts et. al. [261].
- $E_n = \infty$ for SiF. While SiF has been shown to desorb during spontaneous reaction between silicon and XeF_2 at room temperature [267], here under cryogenic, non-spontaneous conditions we assume that fluorine acts as a surface terminating species and that desorption in the form of SiF is insignificant.

Author Contributions

Aiden Martin and Milos Toth designed the project. Aiden Martin performed the experiments. Aiden Martin and Milos Toth performed the numerical modelling. All authors analysed the data and contributed to the writing of the manuscript.

Chapter 8

Extraction and Analysis of Microparticles Embedded in Silica Aerogel

8.1 Abstract

In 2006, NASA's Stardust spacecraft delivered to Earth dust particles collected from the coma of comet Wild-2, with the goal of furthering the understanding of solar system formation. Stardust cometary samples were collected in a low-density, nano-porous silica aerogel making their study technically challenging. This chapter demonstrates the identification, extraction and elemental composition analysis of particles analogous to those collected by NASAs Stardust mission using in situ scanning electron microscope (SEM) techniques. Backscattered electron (BSE) imaging was shown by experimental observation and Monte Carlo simulation to be suitable for locating particles embedded within silica aerogel. Selective removal of the silica aerogel encapsulating an embedded particle was performed by cryogenic NF_3-mediated electron beam induced etching (EBIE). The porous, low-density nature of the aerogel results in an enhanced etch rate compared to solid material, making it an effective, non-mechanical method for the extraction of particles. After extraction, elemental composition of the particle was analysed by energy-dispersive x-ray

spectroscopy using a high spectral resolution microcalorimeter. Signals from fluorine contamination were shown to correspond to non-removed silica aerogel, and only in residual concentrations.

8.2 Introduction

Studying cometary material is critical for determining the origin and evolution of the solar system. Comets formed from presolar and early nebular matter at the outermost edges of the solar system [96], and are an archive of chemical and physical processes which occurred during the early evolution of planetary bodies [97]. In 2006, NASA's Stardust spacecraft delivered to Earth thousands of dust particles collected from the coma of comet 81P/Wild 2 for laboratory study [96]. These samples were the first opportunity to directly study cometary particles of known origin in the laboratory [98]. Unlike previous studies of interplanetary dust particles of unknown origin, these dust particles were likely shielded from damage by thermal, aqueous or radiative processes, therefore retaining their properties since early solar system formation [99].

A portion of the Stardust samples has been analysed to determine their isotropic [97], elemental [268, 269], structural [270], organic [271], and mineralogy and petrology [98] composition using a broad range of techniques including Raman spectroscopy [270, 272], infrared spectroscopy [268, 272, 273], time-of-flight secondary ion mass spectrometry [274, 275], nano secondary ion mass spectrometry [273, 276], energy-dispersive x-ray spectroscopy [99, 105, 269, 275–278] (EDS), transmission electron microscopy [96, 99, 269, 273, 278], electron energy loss spectroscopy [273, 275], synchrotron x-ray diffraction [98], x-ray fluorescence spectroscopy [273], and x-ray absorption near edge structure (XANES) spectroscopy [273]. Preliminary examinations revealed many surprises, such as a large mineralogical diversity [269], almost complete absence of water [268, 269], and the presence of a calcium-aluminium rich inclusion and other kinds of presumably high temperature grains [275]. These findings have already had major implications for solar nebula models, namely that there appears to be a very efficient mechanism for delivering high temperature materials to the outer solar system region where comets accreted [97, 268].

Stardust cometary samples were collected in a low-density, nano-porous silica aerogel [100]. Cometary impact particles are fine-grained and fragile, so they disintegrate on impact with the aerogel. The largest and most robust particles penetrate deep into the aerogel, but the smallest fragments are distributed non-uniformly along the lengths of carrot-shaped impact tracks [101]. Prior to analysis of the particle, removal from the collection medium is generally required. Particles 3 μm and larger can be extracted essentially free of silica aerogel using silicon micro-tweezers and precision (200 nm) motorised micro-manipulators [102]. The process is monitored optically, and requires $>$ 50,000 discrete automatised motions over many hours to extract the particle from of the aerogel. Further optimisation of this process using borosilicate glass micro-needles enables the preparation of a silica aerogel keystone containing a complete impact event [103]. The keystone can then be analysed, or further processed by flattening, mounting on micro-forks and/or sectioning. Particles and fragments as small as 1 μm across can be extracted by sectioning a keystone embedded in epoxy by ultramicrotomy [104]. Techniques for extracting sub-1 μm particles and fragments are however, limited. Furthermore, directly observing the removal of small particles is not possible with light-based techniques. Direct, nanoscale etching techniques are ideal for this application, and a variety of analytical techniques can be also incorporated into these systems for rapid, in situ analysis of the particles.

In this chapter we combine three in situ SEM techniques to enable (i) identification, (ii) rapid extraction and (iii) elemental composition analysis of microparticles embedded in a silica aerogel keystone. A flattened keystone embedded with magnetite and ballistic glass particles was used to replicate Stardust sample conditions. BSE imaging was used to identify particles embedded in silica aerogel. Monte Carlo simulations of electron trajectories in silica aerogel were performed, revealing that BSE imaging is capable of detecting the embedded particles below the optical detection threshold. Extraction was performed by cryogenic NF_3-mediated EBIE [1, 182], which gives rise to selective nanoscale chemical etching in areas exposed to an electron beam and enables real-time imaging during etching. Imaging was performed in variable pressure [95] SEM mode to suppress charging of the electrically insulating silica aerogel [279]. Finally, the extracted particles were analysed in situ by EDS to determine their elemental composition as well as the extent of contamination caused by exposure to NF_3.

8.3 Methods

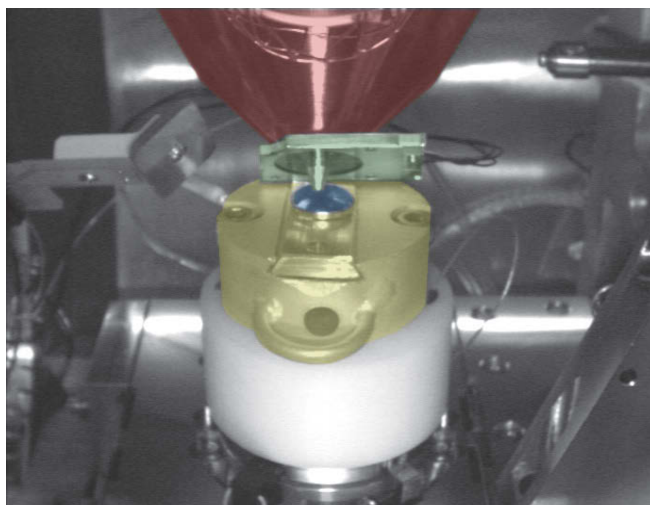

FIGURE 8.1: False colour CCD image of the SEM configured for cryogenic EBIE, showing the SEM pole piece (red), BSE detector (green), sample mounting area (blue) and liquid nitrogen cooling stage (yellow).

Experiments were performed using an FEI XL30 variable pressure SEM configured for cryogenic NF_3-mediated EBIE and high spectral resolution EDS. The capabilities available on this system enable in situ identification, extraction and elemental characterisation of particles embedded in silica aerogel keystones. Figure 8.1 is a false colour charge-coupled device (CCD) image of the SEM chamber, showing the SEM column, BSE detector, sample mounting stub and liquid nitrogen cooling stage.

8.3.1 Detection of Particles by BSE Imaging

Prior to extraction, the precise location of the particle must be determined in the SEM. Particles are encapsulated by the silica aerogel, therefore the imaging technique must be capable of generating contrast based on sub-surface information. Imaging of embedded particles in the SEM using conventional secondary electron detectors is not viable due to the very short escape range of secondary electrons [280]. However, BSEs can potentially produce a viable imaging signal [280]. Here the imaging capabilities of BSE imaging were

determined via experimental observation and Monte Carlo simulation of electron trajectory in solids (CASINO) program [171].

A series of images of a piece of silica aerogel covering an aggregate of silver particles were collected using a solid state BSE detector at varying primary electron energies. Sub-surface features were detected by comparing the contrast in the series of images. As the electron voltage is increased the penetration range of the electron beam is increased, and an increase in contrast is observed where sub-surface features are located. Imaging was performed under a He or NF_3 gaseous environment to suppress electrical charge build-up on the insulating silica aerogel surface. After imaging, the silica aerogel was removed by cryogenic NF_3-mediated EBIE to show the underlying silver aggregate structure for comparison to the sub-surface structure revealed by BSE imaging through the silica aerogel.

Experiments can quickly show the ability of detecting sub-surface particles, however determining the theoretical detection range of BSE imaging efficiently is difficult. CASINO (software version 3.2.0.4) was used to determine the maximum depth at which BSE imaging can resolve particles embedded in a silica aerogel medium. A pyrrhotite particle ($Fe_{0.83}S$, density: 4.61 g cm^{-3}) of varying size was used as the test particle, with simulations performed at varying primary electron energies and depths of the particle from the surface of non-flattened silica aerogel (SiO_2, density 0.02 g cm^{-3}). Properties of non-flattened aerogel were used for this calculation as the result corresponds to a critical keystone cutting parameter. Simply, BSE imaging will not resolve the particle if the cut surface is too far from the particle. At each data point 250,000 primary electron trajectories were simulated for a 10 nm electron beam spot located at the centre of the pyrrhotite particle in the x and y plane. The BSE coefficient at each point was determined by dividing the total number of > 50 eV energy electrons escaping the top plane of the silica aerogel by the total number of electrons used in the simulation. We define the particle as resolvable when the BSE coefficient is greater than the BSE coefficient of silica aerogel material.

8.3.2 Extraction of Particles by EBIE

The cryogenic NF_3-mediated EBIE [182] (Figure 8.2) method was investigated for the extraction of particles from silica aerogel. EBIE is a dry, selective chemical etch process

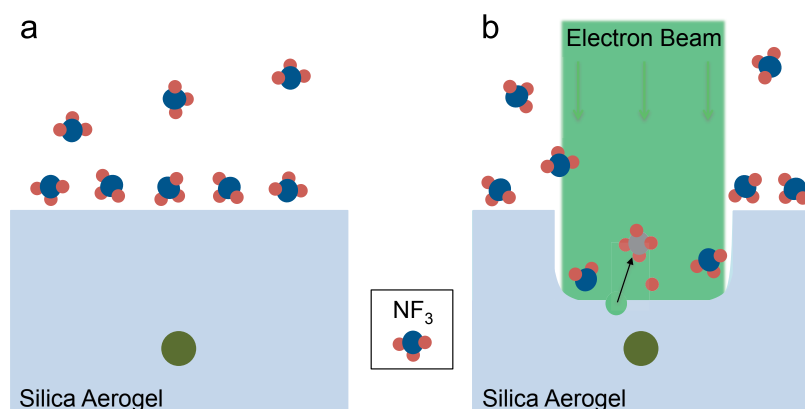

FIGURE 8.2: NF_3-mediated EBIE overview. a) NF_3 molecules adsorb to the silica aerogel. b) On exposure to an electron beam, NF_3 molecules dissociate into fragments (F*) that react with the silica aerogel (SiO_2) producing volatile compounds (SiF_x), which desorb from the surface leaving a void.

where surface adsorbed precursor molecules (i.e. NF_3) are dissociated by an electron beam, producing fragments (F*) that react with surface atoms (Si) to form a volatile compound (SiF_x, where x = 1 - 4) that desorbs from the surface, leaving a void. The technique is analogous to Ga^+ focused ion beam (FIB) milling, however EBIE does not give rise to sputtering, redeposition and gallium ion staining, which can result in noticeable damage to the particle [281].

To ensure the physical composition of particles is not changed during the extraction process, it is imperative that the EBIE precursor does not react spontaneously. XeF_2, widely used as an EBIE precursor for silicon, is therefore not ideal for this application [68]. We selected NF_3 as the EBIE precursor due to its broad material compatibility [89] and preferential removal of SiO_2 in comparison to other silicon containing compounds [182]. Additionally, when used in a variable pressure electron microscope, qualitative results indicate that NF_3 is an excellent electronic charge stabiliser during etching and imaging of insulating materials [182], which reduces the probability of particle loss by coulombic repulsion during etching.

A flattened silica aerogel keystone tile embedded with magnetite and ballistic glass particles was used to replicate a returned Stardust cometary sample. First, particles of interest were identified by BSE imaging in a He gaseous environment. Cryogenic NF_3-mediated

EBIE was then performed by filling the SEM chamber with ∼ 30 Pa of NF_3 and cooling the keystone tile to ∼ 100 K using a liquid nitrogen cold stage. The area of silica aerogel to be removed was scanned by the electron beam in imaging mode to induce etching whilst observing the etching progress in real-time. Etching was halted by blanking the electron beam when complete removal of the silica aerogel surrounding the particle was observed.

8.3.3 Analysis of Particles by X-ray Spectroscopy

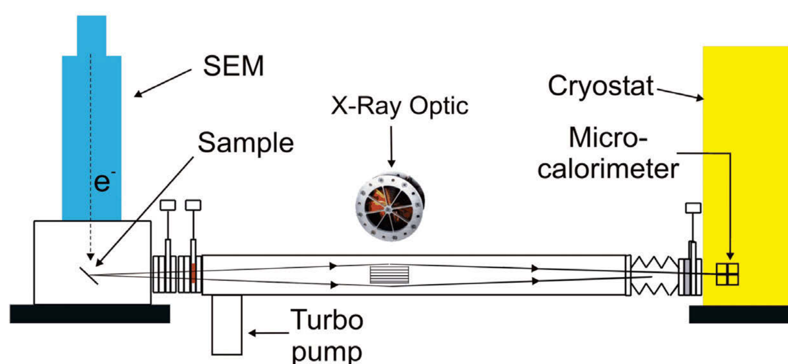

Figure 8.3: Schematic of the SEM configured with a high spectral resolution cryogenic microcalorimeter for EDS.

After extraction from the silica aerogel keystone, ideally the particle is analysed prior to exposure to atmosphere. Here the elemental composition of the particle was determined in situ by EDS, using a high spectral resolution cryogenic microcalorimeter [159] as the x-ray detector (Figure 8.3). The microcalorimeter consists of a tin absorber cooled to ∼ 60 mK, doped germanium semiconductor temperature probe, pulse counting unit and x-ray focusing optic [282]. X-ray energy is determined by measuring the temperature rise of the tin as it absorbs the incoming x-ray photon. In comparison to conventional silicon drift detectors, the microcalorimeter has superior energy resolution (6 eV instead of 130 eV at 6 keV x-ray energy) [159], providing improved element discrimination. Emitted x-rays are focused by the x-ray optic onto the microcalorimeter detector array significantly increasing the collection solid angle of the detector. In addition, by positioning the x-ray optic focal point at the sample, counts from stray x-rays generated in the gaseous environment of the SEM chamber are minimised.

During analysis of the extracted particle, NF_3 was removed from the chamber to prevent further etching. EDS was performed under an inert He environment to minimise sample charging and x-rays are excited by a 10 or 15 keV electron beam. Information for the elemental composition maps was collected by rastering an electron beam over the area of interest while simultaneously detecting x-ray photon emission. Elemental composition maps were constructed by plotting the intensity of the x-ray energy of interest as a function of position. Elemental concentration was calculated using the atomic number, absorbance and fluorescence (ZAF) correction scheme with standards [156, 160].

8.4 Results and Discussion

8.4.1 Detection of Particles by BSE Imaging

BSE images of a piece of silica aerogel covering an aggregate of silver particles were collected using a primary electron beam energy of 10 and 30 keV (Figure 8.4). At 30 keV a noticeable increase in signal was observed in the silica aerogel area directly adjacent to the uncovered silver aggregate. To confirm this increase was caused by sub-surface features, the silica aerogel covering the area was removed by cryogenic NF_3-mediated EBIE using the 30 keV electron beam. Figure 8.4c shows that the silver aggregate did extend under the silica aerogel in the area identified by the BSE image. This is a positive qualitative result for the identification of embedded particles with BSE imaging.

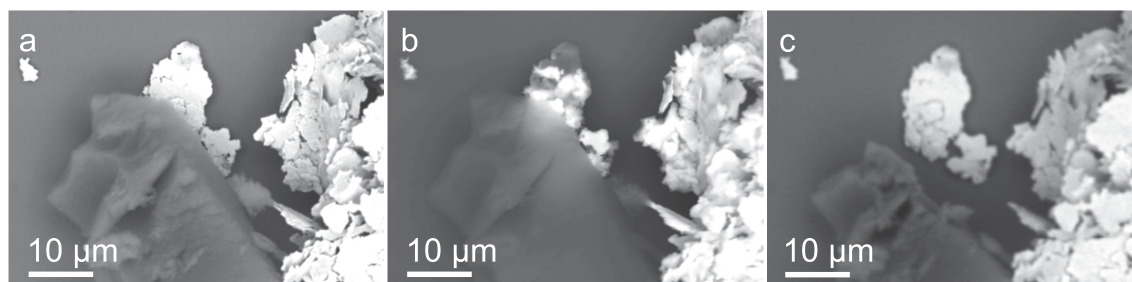

FIGURE 8.4: BSE images of a piece of silica aerogel covering an aggregate of silver particles collected using a (a) 10 and (b) 30 keV primary electron beam. Sub-surface objects are revealed by an increase in signal at higher energies. c) Underlying silver aggregate revealed by cryogenic NF_3-mediated EBIE.

To quantify the ability of the backscattered imaging technique for detecting embedded particles, simulations using CASINO were performed. Figure 8.5a shows the BSE coefficient of silica aerogel with an embedded 500 nm diameter pyrrhotite particle as a function of particle depth at 5, 10, 15 and 30 keV primary electron energy. Initially at shallow depths, the BSE coefficient at all energies is high. As the depth of the particle is increased, the coefficient decreases to a non-zero value corresponding to the BSE coefficient of silica aerogel. While the BSE coefficient at 30 keV is low at shallow depths compared to 10 and 15 keV, the decrease with depth is less pronounced and shows contrast between the measured BSE coefficient and the non-zero background to a depth of ~ 20 μm. This result shows that higher energies are preferable for detecting particles in initial searches, and lower energies are preferable for imaging.

Next, the BSE coefficient as a function of depth at 30 keV primary electron energy was simulated for 100, 200, 500, 1,000 and 3,000 nm diameter particles to determine the effect of size on particle detectability (Figure 8.5b). The depth at which particles are resolvable is dependent on size, for example 100 and 3,000 nm particles were resolved to a depth of ~ 8 μm and ~ 60 μm respectively. These simulation results show BSE imaging to be a promising technique for detecting particles in the low-density silica aerogel medium, especially for particles below the resolvable limit of light-based techniques.

8.4.2 Extraction of Particles by EBIE

Cryogenic NF_3-mediated EBIE was performed on the keystone Stardust replica to demonstrate the extraction of an embedded particle (Figure 8.6). An area rich in embedded particles was identified by BSE imaging in a He environment using a 30 keV, ~ 1 nA electron beam. The chamber was then filled with NF_3 and an area containing a large particle of interest imaged by the electron beam for a total of 30 minutes to induce EBIE, removing the encapsulating silica aerogel. From the size of the particle extracted by EBIE we estimate that the etch pit depth is of the order of microns in the 79×55 μm irradiated area.

The observed volumetric etch rate of material is very high when compared to etching of thermal silicon dioxide material [182]. The etch pit depth after 30 minutes of EBIE in

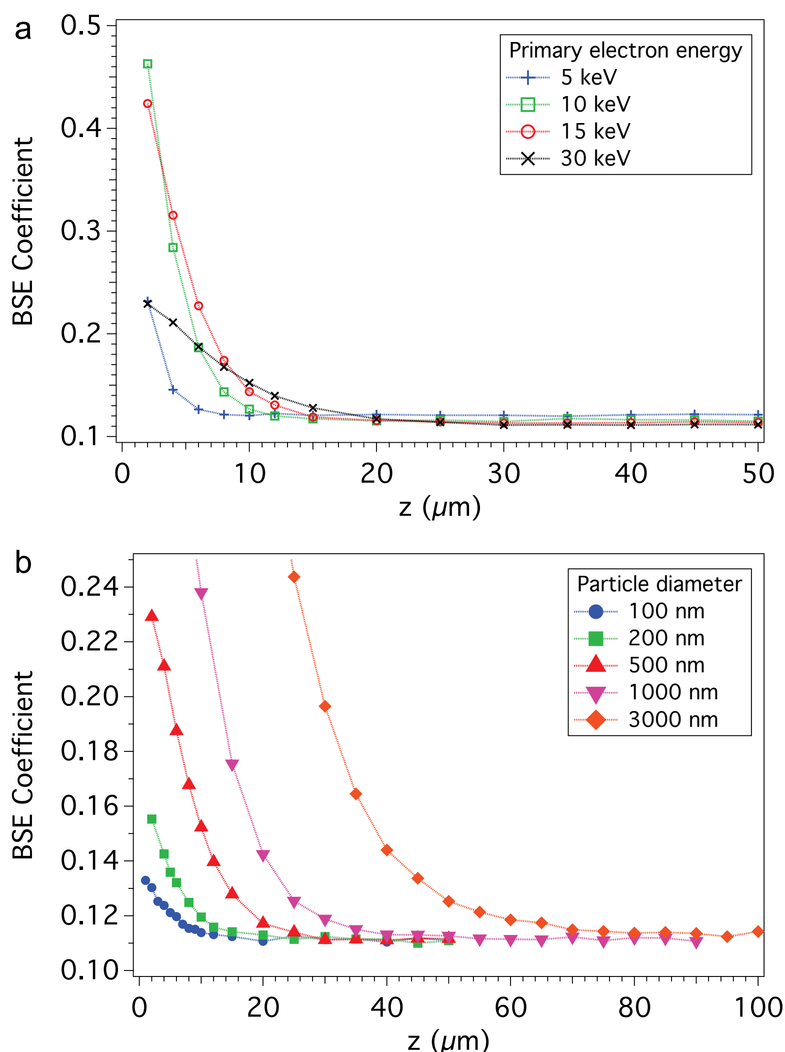

FIGURE 8.5: a) Simulated BSE coefficient of silica aerogel with an embedded 500 nm diameter, spherical pyrrhotite particle as a function of particle depth (z) at 5, 10, 15 and 30 keV primary electron energy. b) Simulated BSE coefficient of silica aerogel with embedded 100, 200, 500, 1,000 and 3,000 nm diameter pyrrhotite particles as a function of z at 30 keV primary electron energy.

thermal silicon oxide was calculated using a previously reported etch rate under similar conditions (Chapter 7) [182] (1.1×10^6 nm^3 s^{-1}). The calculated etch pit depth in thermal oxide is only 0.5 nm when processing an area of 79 × 55 μm. The high etch rate in aerogel material arises from the low-density and high surface area to volume ratio. The aerogel's high etch rate protects the particle from overexposure to possible EBIE reactions, which could result in removal of material. EBIE processing is therefore ideal for removing large volumes of aerogel encapsulating embedded particles. Based on the

observed etch rate of silica aerogel material, the extraction of a 3 μm diameter particle by removing a 10 $\times$ 10 μm area of surrounding aerogel material would take less than 1 minute. The extraction of particles by EBIE is rapid compared to extraction by mechanical micro-manipulators, which requires hours of processing time per particle.

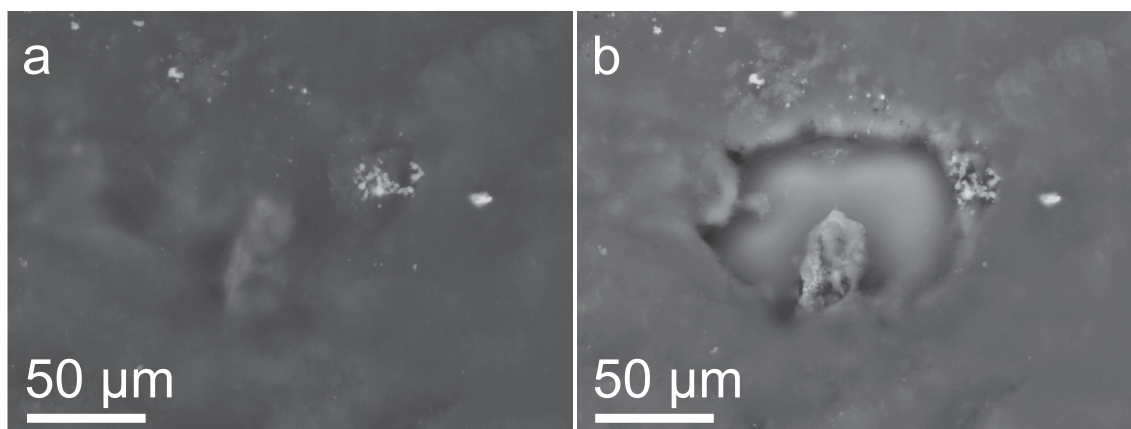

FIGURE 8.6: a) BSE image of a particle embedded in a silica aerogel keystone. b) Removal of encapsulating silica aerogel using cryogenic NF_3-mediated EBIE.

8.4.3 Analysis of Particles by X-ray Spectroscopy

The extracted particle was analysed in situ by EDS to determine its elemental composition and the extent, if any, of fluorine contamination from the EBIE process. EDS was performed using a 10 keV electron beam under a He gaseous environment. False colour images of the x-ray intensity assigned to C, Mg, O, Si, Ti, Al Fe, F and P as a function of location are shown in Figure 8.7. The particle is primarily composed of Mg and O, with concentrated amounts of Al and a small faction of Ti. Importantly, the intensity of detected F is low and correlates with areas of non-removed silica aerogel material.

Figure 8.8 shows an x-ray spectrum collected from the area circled in Figure 8.7 using a 15 keV electron beam under a He gaseous environment. Closer analysis of the particle reveals a small component of residual fluorine, with a concentration of $\sim$ 0.14 %. We ascribe the presence of fluorine to surface functionalisation of the particle induced by electron stimulated desorption of surface species and reaction with NF_3 [283]. This may have been exacerbated by over-etching in an effort to completely remove any trace of silica

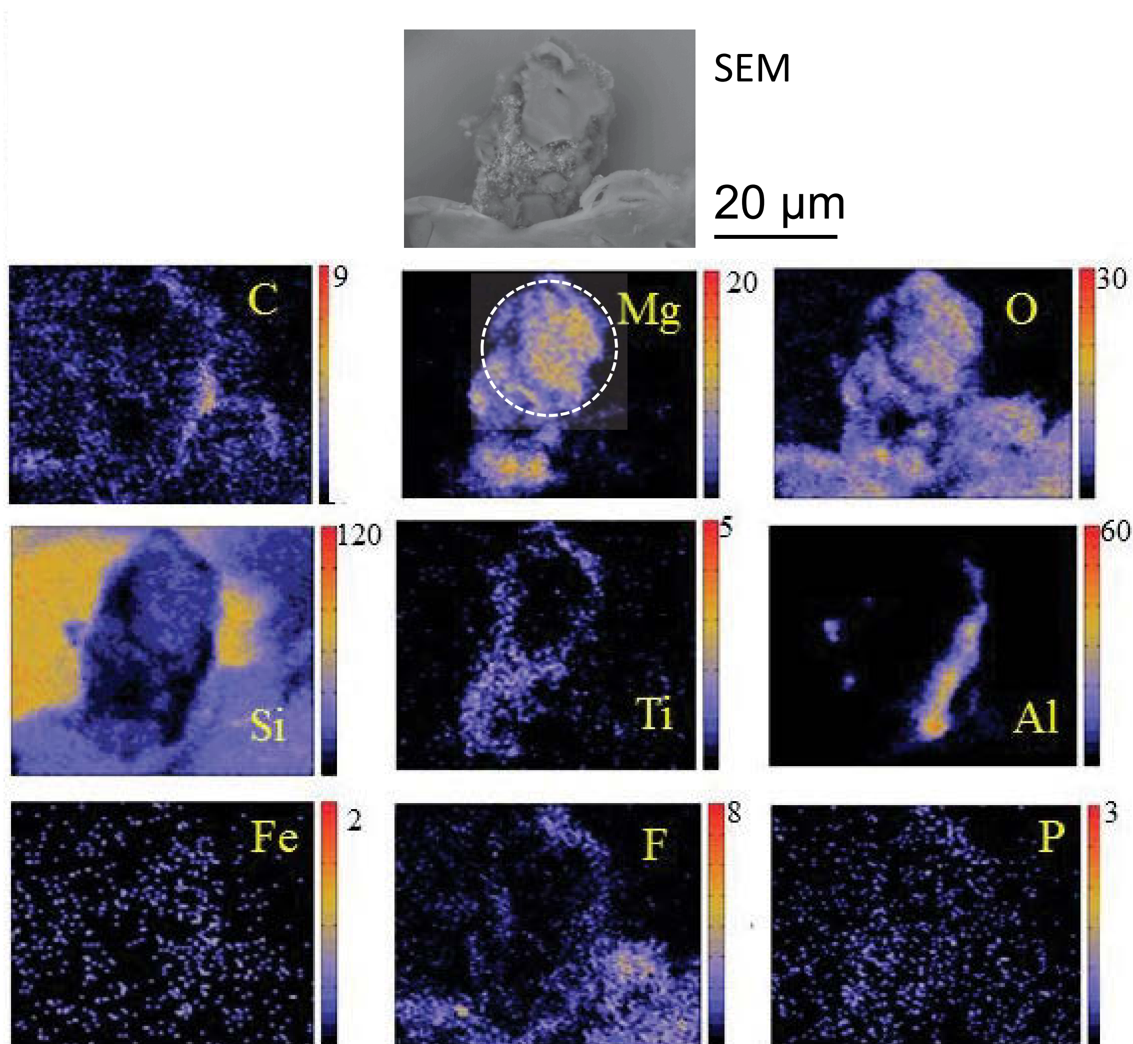

Figure 8.7: SEM image and elemental composition of a particle extracted by EBIE. Elemental composition determined by EDS.

aerogel from the particle. Interestingly, a signal corresponding to the presence of nitrogen is noticeably absent from our x-ray spectrum. Whether nitrogen is desorbed preferentially by further electron irradiation or simply not absorbed is not understood.

8.5 Conclusions

We have demonstrated the identification, rapid extraction and elemental composition analysis of microparticles embedded in silica aerogel keystones by in situ SEM based techniques.

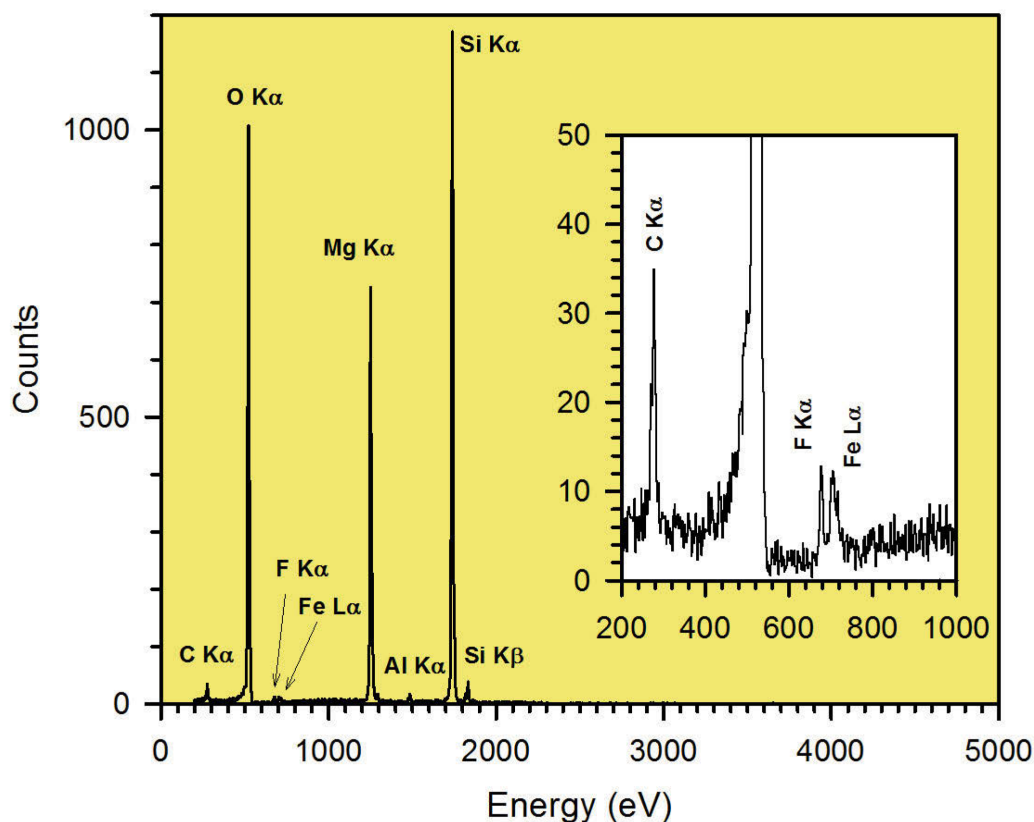

FIGURE 8.8: EDS spectrum of a particle extracted by EBIE (collection area circled in the Mg element map of Figure 8.7). The particle is rich in O, Mg and Si with small traces of F. The F signal intensity corresponds to a concentration of 0.14 %, which originates from remnant silica aerogel.

BSE imaging was shown by CASINO simulation to detect particles that are below the optical detection limit. The depth at which particles can be resolved is a function of particle size and primary electron energy. After locating an embedded particle, cryogenic NF_3-mediated EBIE successfully removed the encapsulating silica aerogel medium, without physically handling, modifying or damaging them. EBIE can be applied selectively to many particles within a single impact track. In situ analysis by EDS using a cryogenic microcalorimeter shows fluorine contamination to be minimal and corresponds to non-removed silica aerogel.

The combination of these three in situ techniques provides an excellent platform for the study of Stardust cometary samples, and when optimised, characterising interstellar cosmic

dust particles [284, 285]. EBIE can be extended to aerogels of other composition, such as carbon, if future missions use these as the collection medium. With the optimisation of existing gas precursor chemistries EBIE could also replace FIB milling for the extraction of particles from aluminum foil [105, 277]. In situ EDS analysis using a high spectral resolution cryogenic microcalorimeter provides unambiguous detection of light and heavy elements without requiring further processing or exposing the particles to atmosphere.

Author Contributions

Eric Silver, Ting Lin, Aiden Martin and Milos Toth designed the project. Aiden Martin, Ting Lin and Eric Silver performed the EBIE and BSE imaging experiments. Aiden Martin performed the BSE coefficient simulations. Eric Silver and Ting Lin performed the EDS measurements. All authors analysed the data and contributed to the writing of the manuscript.

Chapter 9

General Conclusions and Future Directions

9.1 General Conclusions

In this thesis, mechanisms of gas-mediated electron beam induced etching (EBIE) of carbon and silicon based materials were investigated to improve our fundamental understanding of these processes. The effect of residual contaminants, electron induced restructuring, material structure and precursor-substrate interaction were demonstrated, and the standard continuum EBIE model refined to included these observations. New applications and methods were developed by applying these findings, greatly expanding the applicability of EBIE as a tool for nanofabrication and editing.

A number of mechanisms proposed in the literature for electron beam induced removal of carbon were shown to be insignificant. These include atomic displacements caused by knock-on by low energy electrons, electron beam heating, sputtering by ionised gas molecules, and chemical etching driven by a number of gases that include N_2. The behaviour ascribed to these mechanisms was instead explained by chemical etching caused by electron beam induced dissociation of residual contaminants present in the vacuum systems that are typically used for EBIE.

The etch rate of ultra nano-crystalline diamond (UNCD) is super-linear with time, and cannot be described by existing standard models of EBIE. Models incorporating dynamic surface site activation and the role of electron beam damage are able to reproduce the observed etch kinetics. The models predict a rate kinetics regime limited by the concentration of active surface sites and reduces to standard EBIE models when the active site generation rate approaches zero. Analogous restructuring effects likely play a role in EBIE of other materials, and possibly account for atypical dependencies of etch rate on time which have been reported previously for a number of precursor-substrate combinations.

EBIE kinetics of single crystal diamond depend on the gaseous conditions. Anisotropic etching along crystallographic planes produces dynamic self-ordered patterns during the etching process. H_2O-mediated EBIE of (001) orientated diamond produces terraced steps across the surface. The anisotropy of etching changes with the addition of NH_3 due to the production of hydrogen and amine radicals by electron induced dissociation of NH_3. Hydrogen radicals terminate the surface, which restructures the lattice step edge atoms and stabilises the {111} set of planes. This gives rise to the formation of inverted pyramid structures across the surface. Anisotropic etching has not been observed in EBIE previously due to the precursor chemistry and substrate conditions used during etching. These results have major implications for EBIE of single crystal material. Anisotropic etching can be used to realise complex surface geometries and to gain insights into EBIE rate kinetics.

New applications for EBIE have been realised and demonstrate the potential of EBIE in comparison to traditional etching techniques for wide bandgap semiconductors. Patterning and sculpting of optically active diamond structures using H_2O-mediated EBIE can be achieved via mask-based lithographic and direct editing approaches. For the first time, direct 3D etching is realised on various facets of a single microparticle. Photoluminescence and Raman scattering analysis show that the unique optical properties of diamond are maintained and no graphitisation occurs during processing. EBIE can also be used for polishing surfaces milled by a focused ion beam (FIB). The polishing technique is limited to areas milled by ions such as O^+ or O_2^+ which can be removed by EBIE. The technique is not viable for areas milled by Ga^+ ions, as to date, there is no EBIE method to remove gallium and carbon material simultaneously. The resolution of the structures produced by

the combination of FIB milling and EBIE polishing is ultimately limited by the range of damage induced by the ion beam.

The general model of EBIE can be used to predict conditions that enable the use of precursors previously thought impractical for EBIE. For example, reducing the substrate temperature increases the concentration of surface bound precursor, enabling the use of precursors which weakly bind to the substrate surface. Substrate cooling has previously not been used as a method to accelerate EBIE as it also effects the thermal desorption rate of the final reaction products. The etch rate of NF_3-mediated EBIE of Si, SiO_2, SiC and Si_3N_4 is greatly enhanced by substrate cooling and comparable to existing precursors such as Cl_2. This shows that a range of EBIE reaction products (SiF_x) can still desorb at cryogenic substrate temperatures while irradiated by electrons and that cryogenic substrate cooling can be used to broaden the range of precursors that can be used to realise EBIE. The new precursor NF_3 enables high resolution EBIE in the absence of artifacts caused by delocalised spontaneous etching of the substrates, in contrast to XeF_2-mediated EBIE of silicon.

NF_3-mediated EBIE was applied to NASA'a Stardust project. Microparticles are rapidly removed from the silica aerogel collection medium and unlike existing techniques, EBIE can be applied selectively to many particles within a single impact track. A platform combining in situ backscatter imaging, EBIE and elemental analysis provides an excellent toolkit for the study of Stardust cometary samples. EBIE can also be extended to aerogels of other composition, such as carbon, if future missions use these as the collection medium.

9.2 Future Directions

As the field progresses, I predict EBIE will be a valuable tool for nanofabrication and the study of gas-solid-electron interactions. With features of interest decreasing in size to the range of damage induced by ions, EBIE must be considered for select applications which previously relied on FIB milling. This is already being observed in applications such as repair of chromium lithography masks [80] and is driving the push for EBIE development. As the understanding of reaction mechanisms increases and technological enhancements

are made such as multiple electron beam processing [152], it is hoped that etch rates can be increased to compete with FIB milling.

During the course of this work, the importance of material properties on the kinetics and mechanisms of EBIE has become evident. Obvious next steps are to find new substrate-precursor combinations where dynamic surface site activation and anisotropic etching can be reproduced. Anisotropic etching in particular can provide important information on material properties such as surface bond configuration, and also gives control over substrate surface topography. The development of a surface topography simulator which can model anisotropic etch rates and local electron flux profiles would enhance the ability to predict the geometry of structures fabricated by EBIE.

The next major focus of fundamental scientific study should be the dissociation process of precursor molecules on the substrate surface. Reactive fragments can be generated by two electron induced processes, dissociative electron attachment (DEA) and dissociative electron ionisation (DEI) [42]. The cross-sections of the two processes peak in two distinct incident electron energy ranges and produce species of varied charge and chemistry. Some work has already been performed in electron beam induced deposition to determine the role of these two processes [47, 48], however the mechanism that generates reactive species giving rise to EBIE is overlooked in current studies.

Based on the work with NF_3, many new precursors can be enabled or existing processes enhanced by manipulation of the substrate temperature. Reducing the substrate temperature is an efficient method to enable the use of precursors which bind weakly to the surface. Future work in methods to enable new EBIE processes could include heating of the substrate to increase the desorption rate of reaction products. In precursor-substrate combinations where the reaction rate is limited by the desorption of reaction products substrate heating may be a viable solution for increasing the rate of EBIE.

Despite the progress in applications and precursor chemistries made recently, methods for EBIE of III-V (e.g. GaAs and GaN) and ZnO semiconductors is still not available. Current precursors (i.e XeF_2) enable etching of As [153] and N components, however no chemistry is available to remove Ga or Zn from the surface at room temperature. To overcome this

problem, development of a new method or refinement of etch precursor chemistry will be required.

Bibliography

[1] I. Utke, S. Moshkalev, P. Russell, *Nanofabrication Using Focused Ion and Electron Beams: Principles and Applications.* Oxford University Press, New York (2012).

[2] M. Toth, et al., *Nano Lett.* **7**(2), 525 (2007).

[3] N. Yao, *Focused Ion Beam Systems: Basics and Applications.* Cambridge University Press, Cambridge (2011).

[4] C. R. Arumainayagam, H. Lee, R. B. Nelson, D. R. Haines, R. P. Gunawardane, *Surf. Sci. Rep.* **65**(1), 1 (2010).

[5] D. Fox, et al., *Appl. Phys. Lett.* **98**(24), 243117 (2011).

[6] S. Goler, et al., *J. Appl. Phys.* **110**(6), 064308 (2011).

[7] J. C. Meyer, et al., *Phys. Rev. Lett.* **108**(19), 196102 (2012).

[8] C. Thiele, et al., *Carbon* **64**, 84 (2013).

[9] Y. Lan, et al., *Small* **10**(22), 4778 (2014).

[10] T. D. Yuzvinsky, A. M. Fennimore, W. Mickelson, C. Esquivias, A. Zettl, *Appl. Phys. Lett.* **86**(5), 053109 (2005).

[11] P. Liu, F. Arai, T. Fukuda, in *IEEE-NANO 2006. Sixth IEEE Conference on Nanotechnology*, vol. 2, pp. 540–543. 17-20 June, 2006, Cincinnati, OH, U.S.A., Institute of Electrical and Electronics Engineers, New York (2006).

[12] P. S. Spinney, D. G. Howitt, S. D. Collins, R. L. Smith, *Nanotechnology* **20**(46), 465301 (2009).

[13] C. Thiele, et al., *Appl. Phys. Lett.* **99**, 173105 (2011).

[14] C. J. Lobo, A. Martin, M. R. Phillips, M. Toth, *Nanotechnology* **23**(37), 375302 (2012).

[15] D. Wang, P. Hoyle, J. Cleaver, G. Porkolab, N. Macdonald, *J. Vac. Sci. Technol., B* **13**(5), 1984 (1995).

[16] M. Toth, C. J. Lobo, G. Hartigan, W. Ralph Knowles, *J. Appl. Phys.* **101**, 054309 (2007).

[17] H. Miyazoe, I. Utke, J. Michler, K. Terashima, *Appl. Phys. Lett.* **92**, 043124 (2008).

[18] P. Hoffmann, et al., in *Proc. SPIE 5925, Nanophotonic Materials and Systems II*, vol. 5925, pp. 59256–592515. 31 July, 2005, San Diego, California, U.S.A., The International Society for Optical Engineering, Bellingham (2005).

[19] J. Niitsuma, X. Yuan, S. Koizumi, T. Sekiguchi, *Jpn. J. Appl. Phys.* **45**(1–3), L71 (2006).

[20] J. Taniguchi, I. Miyamoto, N. Ohno, S. Honda, *Jpn. J. Appl. Phys.* **35**(12S), 6574 (1996).

[21] J. Taniguchi, et al., *Jpn. J. Appl. Phys.* **36**(12S), 7691 (1997).

[22] S. Matsui, K. Mori, *Appl. Phys. Lett.* **51**(19), 1498 (1987).

[23] P. Roediger, H. Wanzenboeck, G. Hochleitner, E. Bertagnolli, W. Buehler, *J. Appl. Phys.* **108**, 124316 (2010).

[24] P. Roediger, G. Hochleitner, E. Bertagnolli, H. Wanzenboeck, W. Buehler, *Nanotechnology* **21**, 285306 (2010).

[25] N. Vanhove, P. Lievens, W. Vandervorst, *J. Vac. Sci. Technol., B* **28**(6), 1206 (2010).

[26] S. J. Randolph, J. D. Fowlkes, P. D. Rack, *Crit. Rev. Solid State Mater. Sci.* **31**(3), 55 (2006).

[27] P. D. Rack, et al., *Appl. Phys. Lett.* **82**(14), 2326 (2003).

[28] S. Randolph, M. Toth, J. Cullen, C. Chandler, C. Lobo, *Appl. Phys. Lett.* **99**, 213103 (2011).

[29] H. F. Winters, J. W. Coburn, *Appl. Phys. Lett.* **34**(1), 70 (1979).

[30] T. Bret, et al., *J. Vac. Sci. Technol., B* **27**(6), 2727 (2009).

[31] P. Roediger, H. Wanzenboeck, G. Hochleitner, E. Bertagnolli, *J. Vac. Sci. Technol., B* **29**, 041801 (2011).

[32] A. Ganczarczyk, M. Geller, A. Lorke, *Nanotechnology* **22**(4), 045301 (2011).

[33] F. J. Schoenaker, et al., *Nanotechnology* **22**(26), 265304 (2011).

[34] Y.-M. Sun, S. Wang, J. White, A. Stivers, T. Liang, *Applied Surface Science* **252**(2), 311 (2005).

[35] D. Winkler, H. Zimmermann, M. Mangerich, R. Trauner, *Microelectron. Eng.* **31**(1-4), 141 (1996).

[36] T. Lukasczyk, M. Schirmer, H. Steinrück, H. Marbach, *Small* **4**(6), 841 (2008).

[37] J. D. Barry, et al., *J. Vac. Sci. Technol., B* **24**(6), 3165 (2006).

[38] K. Mølhave, et al., *Nano. Lett.* **3**(11), 1499 (2003).

[39] J. Li, M. Toth, K. Dunn, B. Thiel, *J. Appl. Phys.* **107**(10), 103540 (2010).

[40] J. Li, et al., *Appl. Phys. Lett.* **93**(2), 023130 (2008).

[41] A. Botman, J. J. L. Mulders, C. W. Hagen, *Nanotechnology* **20**(37), 372001 (2009).

[42] I. Utke, P. Hoffmann, J. Melngailis, *J. Vac. Sci. Technol., B* **26**(4), 1197 (2008).

[43] A. Botman, J. J. L. Mulders, R. Weemaes, S. Mentink, *Nanotechnology* **17**(15), 3779 (2006).

[44] M. G. Lassiter, P. D. Rack, *Nanotechnology* **19**(45), 455306 (2008).

[45] M. Toth, C. J. Lobo, M. J. Lysaght, A. E. Vladar, M. T. Postek, *J. Appl. Phys.* **106**, 034306 (2009).

[46] J. Bishop, et al., *Phys. Rev. Lett.* **109**(14), 146103 (2012).

[47] J. D. Fowlkes, S. J. Randolph, P. Rack, *J. Vac. Sci. Technol., B* **23**(6), 2825 (2005).

[48] S. Engmann, M. Stano, Š. Matejčík, O. Ingólfsson, *Angew. Chem. Int. Ed. Engl.* **50**(40), 9475 (2011).

[49] R. Yang, et al., *Adv. Mater.* **22**(36), 4014 (2010).

[50] P. Bachmann, D. Leers, D. Wiechert, *Diamond Relat. Mater.* **2**(5–7), 683 (1993).

[51] I. Bello, et al., *Thin Solid Films* **368 (2)**, 222 (2000).

[52] D. B. Lee, *J. Appl. Phys.* **40**(11), 4569 (1969).

[53] L. Venema, *Nature* **479**(7373), 309 (2011).

[54] F. A. Zwanenburg, et al., *Rev. Mod. Phys.* **85**(3), 961 (2013).

[55] A. Morello, *Nat. Nanotechnol.* **8**(4), 233 (2013).

[56] J. T. Muhonen, et al., *Nat. Nanotechnol.* **9**(12), 986 (2014).

[57] J. Leuthold, C. Koos, W. Freude, *Nat. Photonics* **4**(8), 535 (2010).

[58] G. T. Reed, G. Mashanovich, F. Y. Gardes, D. J. Thomson, *Nat. Photonics* **4**(8), 518 (2010).

[59] D. Liang, J. E. Bowers, *Nat. Photonics* **4**(8), 511 (2010).

[60] V. Lindroos, M. Tilli, A. Lehto, T. Motooka (eds.), *Handbook of Silicon Based MEMS Materials and Technologies*. William Andrew Publishing, Boston (2010).

[61] D. Fine, et al., *Adv. Healthcare Mater.* **2**(5), 632 (2013).

[62] G. T. A. Kovacs, N. I. Maluf, K. E. Petersen, *Proc. IEEE* **86**(8), 1536 (1998).

[63] B. Wu, A. Kumar, S. Pamarthy, *J. Appl. Phys.* **108**(5), 051101 (2010).

[64] S. M. Rossnagel, W. D. Westwood, J. J. Haber, *Handbook of Plasma Processing Technology: Fundamentals, Etching, Deposition, and Surface Interactions*. Noyes Publications, Park Ridge (1990).

[65] H. P. Gillis, et al., *Appl. Phys. Lett.* **66**(19), 2475 (1995).

[66] H. P. Gillis, D. A. Choutov, K. P. Martin, S. J. Pearton, C. R. Abernathy, *J. Electrochem. Soc.* **143**(11), L251 (1996).

[67] Z. Huang, N. Geyer, P. Werner, J. de Boor, U. Gösele, *Adv. Mater.* **23**(2), 285 (2010).

[68] H. F. Winters, J. W. Coburn, *Surf. Sci. Rep.* **14**(4-6), 161 (1992).

[69] D. L. Flamm, *Pure Appl. Chem.* **62**(9), 1709 (1990).

[70] H. J. Levinson, *Principles of Lithography*, Second Edition. SPIE Press, Bellingham (2005).

[71] C. Mack, *Fundamental Principles of Optical Lithography.* John Wiley & Sons, Ltd, Chichester (2007).

[72] A. A. Tseng, K. Chen, C. D. Chen, K. J. Ma, *IEEE Trans. Electron. Packag. Manufact.* **26**(2), 141 (2003).

[73] Z. J. Zhou, in N. Yao, Z. L. Wang (eds.), *Electron Beam Lithography*, pp. 287–321. Springer US, Boston (2005).

[74] K. Sugioka, Y. Cheng, *Light: Sci. Appl.* **3**, e149 (2014).

[75] C. Li, et al., *J. Micromech. Microeng.* **19**(12), 125007 (2009).

[76] S. Reyntjens, R. Puers, *J. Micromech. Microeng.* **11**(4), 287 (2001).

[77] N. Bassim, K. Scott, L. A. Giannuzzi, *MRS Bull.* **39**(04), 317 (2014).

[78] A. A. Tseng, *J. Micromech. Microeng.* **14**(4), R15 (2004).

[79] L. A. Giannuzzi, F. A. Stevie, *Micron* **30**(3), 197 (1999).

[80] K. Edinger, et al., *J. Vac. Sci. Technol., B* **22**(6), 2902 (2004).

[81] M. J. M. Vugts, G. J. P. Joosten, A. van Oosterum, H. A. J. Senhorst, H. C. W. Beijerinck, *J. Vac. Sci. Technol., A* **12**(6), 2999 (1994).

[82] D. E. Ibbotson, D. L. Flamm, J. A. Mucha, V. M. Donnelly, *Appl. Phys. Lett.* **44**(12), 1129 (1984).

[83] M. Lassiter, T. Liang, P. Rack, *J. Vac. Sci. Technol., B* **26**, 963 (2008).

[84] H. J. Mattausch, *J. Vac. Sci. Technol., B* **1**(1), 15 (1983).

[85] J. H. Brannon, *J. Vac. Sci. Technol., B* **5**(5), 1399 (1987).

[86] G. Bruno, P. Capezzuto, G. Cicala, P. Manodoro, *J. Vac. Sci. Technol., A* **12**(3), 690 (1994).

[87] A. Tasaka, et al., *J. Vac. Sci. Technol., A* **20**(4), 1254 (2002).

[88] P. D. Haaland, C. Q. Jiao, A. Garscadden, *Chem. Phys. Lett.* **340**(5-6), 479 (2001).

[89] R. Miotto, A. Ferraz, G. Srivastava, *Surf. Sci.* **454–456**(0), 152 (2000).

[90] D. Joy, 'Environmental e-beam systems for the metrology, editing and repair of lithographic masks, and for nanofabrication', Tech. Rep. P018474, Semiconductor Research Corporation, Durham, NC, U.S.A. (2007).

[91] M. Huth, et al., *Beilstein J. Nanotechnol.* **3**(1), 597 (2012).

[92] D. A. Smith, J. D. Fowlkes, P. D. Rack, *Small* **4**(9), 1382 (2008).

[93] J. D. Fowlkes, P. D. Rack, *ACS Nano* **4**(3), 1619 (2010).

[94] A. A. Martin, M. R. Phillips, M. Toth, *ACS Appl. Mater. Interfaces* **5**(16), 8002 (2013).

[95] G. D. Danilatos, *Adv. Electron. Electron Phys.* **71**, 109 (1988).

[96] D. Brownlee, et al., *Science* **314**(5806), 1711 (2006).

[97] K. D. McKeegan, et al., *Science* **314**(5806), 1724 (2006).

[98] M. E. Zolensky, et al., *Science* **314**(5806), 1735 (2006).

[99] J. Stodolna, D. Jacob, H. Leroux, *Meteorit. Planet. Sci.* **44**(10), 1511 (2009).

[100] P. Tsou, *J. Non-Cryst. Solids* **186**(0), 415 (1995).

[101] A. T. Kearsley, et al., *Meteorit. Planet. Sci.* **47**(4), 737 (2012).

[102] A. J. Westphal, et al., *Meteorit. Planet. Sci.* **37**(6), 855 (2002).

[103] A. J. Westphal, et al., *Meteorit. Planet. Sci.* **39**(8), 1375 (2004).

[104] G. Matrajt, D. E. Brownlee, *Meteorit. Planet. Sci.* **41**(11), 1715 (2006).

[105] J. C. Bridges, I. A. Franchi, S. F. Green, in *Lunar and Planetary Science Conference XXXVII, abstract 1664*. March 13-17, 2006, League City, Texas, U.S.A., Lunar and Planetary Institute, Houston (2006).

[106] A. K. Geim, K. S. Novoselov, *Nat. Mater.* **6**(3), 183 (2007).

[107] A. H. Castro Neto, N. M. R. Peres, K. S. Novoselov, A. K. Geim, *Rev. Mod. Phys.* **81**(1), 109 (2009).

[108] W. Choi, I. Lahiri, R. Seelaboyina, Y. S. Kang, *Crit. Rev. Solid State Mater. Sci.* **35**(1), 52 (2010).

[109] K. S. Novoselov, et al., *Nature* **490**(7419), 192 (2012).

[110] S. B. Sinnott, R. Andrews, *Crit. Rev. Solid State Mater. Sci.* **26**(3), 145 (2001).

[111] O. A. Shenderova, V. V. Zhirnov, D. W. Brenner, *Crit. Rev. Solid State Mater. Sci.* **27**(3-4), 227 (2002).

[112] C. J. H. Wort, R. S. Balmer, *Mater. Today* **11**(1-2), 22 (2008).

[113] I. Aharonovich, et al., *Rep. Prog. Phys.* **74**(7), 076501 (2011).

[114] M. Loncar, A. Faraon, *MRS Bull.* **38**(02), 144 (2013).

[115] O. Auciello, et al., *J. Phys.: Condens. Matter* **16**(16), R539 (2004).

[116] O. Auciello, A. V. Sumant, *Diamond Relat. Mater.* **19**(7-9), 699 (2010).

[117] J. Zhang, M. Zhou, W. Wu, Y. Tang, *Plasma Sci. Technol.* **15**(6), 552 (2013).

[118] C. D. McGray, R. A. Allen, M. Cangemi, J. Geist, *Diamond Relat. Mater.* **20**(10), 1363 (2011).

[119] M. P. Hiscocks, et al., *Opt. Express* **16**(24), 19512 (2008).

[120] C. Vivensang, G. Turban, E. Anger, A. Gicquel, *Diamond Relat. Mater.* **3**(4-6), 645 (1994).

[121] G. S. Sandhu, W. K. Chu, *Appl. Phys. Lett.* **55**(5), 437 (1989).

[122] P. Leech, G. Reeves, A. Holland, F. Shanks, *Diamond Relat. Mater.* **11**(3–6), 833 (2002).

[123] Y. Yamazaki, K. Ishikawa, N. Mizuochi, S. Yamasaki, *Jpn. J. Appl. Phys.* **46**(1), 60 (2007).

[124] B. R. Stoner, G. J. Tessmer, D. L. Dreifus, *Appl. Phys. Lett.* **62**(15), 1803 (1993).

[125] A. Joshi, R. Nimmagadda, *J. Mater. Res.* **6**(7), 1484 (1991).

[126] M. J. Burek, et al., *Nano Lett.* **12**(12), 6084 (2012).

[127] B. J. M. Hausmann, et al., *Nano Lett.* **13**(5), 1898 (2013).

[128] I. Aharonovich, et al., *Adv. Mater.* **24**(10), OP54 (2012).

[129] Y. Tao, C. Degen, *Adv. Mater.* **25**(29), 3962 (2013).

[130] I. Bayn, B. Meyler, J. Salzman, R. Kalish, *New J. Phys.* **13**, 025018 (2011).

[131] A. V. Krasheninnikov, F. Banhart, *Nat. Mater.* **6**(10), 723 (2007).

[132] A. Perentes, G. Sinicco, G. Boero, B. Dwir, P. Hoffmann, *J. Vac. Sci. Technol., B* **25**(6), 2228 (2007).

[133] H. W. Goldstein, *J. Phys. Chem.* **68**(1), 39 (1964).

[134] F. Banhart, *Rep. Prog. Phys.* **62**(8), 1181 (1999).

[135] V. Kuznetsov, et al., *Carbon* **32**(5), 873 (1994).

[136] D. Teweldebrhan, A. A. Balandin, *Appl. Phys. Lett.* **94**(1), 013101 (2009).

[137] G. Liu, D. Teweldebrhan, A. A. Balandin, *IEEE Trans. Nanotechnol.* **10**(4), 865 (2011).

[138] A. P. Magyar, et al., *Appl. Phys. Lett.* **99**(8), 081913 (2011).

[139] S. Kaufmann, et al., *Proc. Natl. Acad. Sci. U. S. A.* **110**(27), 10894 (2013).

[140] P. Maletinsky, et al., *Nat. Nanotechnol.* **7**(5), 320 (2012).

[141] J. Riedrich-Moeller, et al., *Nat. Nanotechnol.* **7**(1), 69 (2012).

[142] X. Zhu, et al., *Nature* **478**(7368), 221 (2011).

[143] V. V. Dobrovitski, G. D. Fuchs, A. L. Falk, C. Santori, D. D. Awschalom, *Annu. Rev. Condens. Matter Phys.* **4**, 23 (2013).

[144] L. Childress, R. Hanson, *MRS Bull.* **38**(2), 134 (2013).

[145] A. Faraon, et al., *New J. Phys.* **15**(2), 025010 (2013).

[146] D. McCloskey, et al., *Appl. Phys. Lett.* **104**(3), 031109 (2014).

[147] W. R. McKenzie, M. Z. Quadir, M. H. Gass, P. R. Munroe, *Diamond Relat. Mater.* **20**(8), 1125 (2011).

[148] I. Bayn, et al., *Appl. Phys. Lett.* **99**(18), 183109 (2011).

[149] J. Riedrich-Möller, et al., *Nano Lett.* **14**(9), 5281 (2014).

[150] B. Thiel, et al., *Rev. Sci. Instrum.* **77**(3), 033705 (2006).

[151] M. Toth, W. R. Knowles, B. L. Thiel, *Appl. Phys. Lett.* **88**(2), 023105 (2006).

[152] P. C. Post, A. Mohammadi-Gheidari, C. W. Hagen, P. Kruit, *J. Vac. Sci. Technol., B* **29**(6), 06F310 (2011).

[153] W. C. Simpson, P. R. Varekamp, D. K. Shuh, J. A. Yarmoff, *J. Vac. Sci. Technol., A* **13**(3), 1709 (1995).

[154] Y. Sugimoto, M. Taneya, K. Akita, H. Kawanishi, *J. Appl. Phys.* **69**(4), 2725 (1991).

[155] M. Toth, M. Uncovsky, W. R. Knowles, F. S. Baker, *Appl. Phys. Lett.* **91**(5), 053122 (2007).

[156] J. Goldstein, et al., *Scanning Electron Microscopy and X-ray Microanalysis, 3rd edition.* Springer US, New York (2003).

[157] G. Binnig, C. F. Quate, *Phys. Rev. Lett.* **56**(9), 930 (1986).

[158] D. Nečas, P. Klapetek, *Cent. Eur. J. Phys.* **10**(1), 181 (2012).

[159] E. Silver, M. LeGros, N. Madden, J. Beeman, E. Haller, *X-Ray Spectrom.* **25**(3), 115 (1996).

[160] V. D. Scott, G. Love, *X-Ray Spectrom.* **21**(1), 27 (1992).

[161] S. Zhang, *Raman Spectroscopy and its Application in Nanostructures.* John Wiley & Sons, Ltd, Chichester, U.K. (2012).

[162] A. C. Ferrari, J. Robertson, *Philos. Transact A Math. Phys. Eng. Sci.* **362**(1824), 2477 (2004).

[163] J. Orwa, K. Nugent, D. Jamieson, S. Prawer, *Phys. Rev. B: Condens. Matter Mater. Phys.* **62**(9), 5461 (2000).

[164] T. Aoki, *Characterization of Materials*, chap. Photoluminescence Spectroscopy. John Wiley & Sons, Inc., Hoboken, NJ, U.S.A. (2002).

[165] J. Smith, *Quantum Information Processing with Diamond*, chap. Characterisation of single defects in diamond in the development of quantum devices, pp. 68–97. Woodhead Publishing, Cambridge, U.K. (2014).

[166] B. G. Yacobi, D. B. Holt, *Cathodoluminescence Microscopy of Inorganic Solids.* Springer US, New York (1990).

[167] M. Toth, M. R. Phillips, *Scanning* **20**(6), 425 (1998).

[168] K. Fleischer, et al., *Appl. Phys. Lett.* **74**(8), 1114 (1999).

[169] M. W. Doherty, et al., *Phys. Rep.* **528**(1), 1 (2013).

[170] P. Hovington, D. Drouin, R. Gauvin, *Scanning* **19**(1), 1 (1997).

[171] H. Demers, et al., *Scanning* **33**(3), 135 (2011).

[172] J. F. Ziegler, J. P. Biersack, M. D. Ziegler, *SRIM - The Stopping and Range of Ions in Matter*. SRIM Co., Chester, MD, U.S.A (2008).

[173] T. E. Derry, R. W. Fearick, J. P. F. Sellschop, *Nucl. Instrum. Methods* **170**(1-3), 135 (1980).

[174] J. Feng, et al., *Nanoscale* **4**(16), 4883 (2012).

[175] S. Castelletto, et al., *New J. Phys.* **13**(2), 025020 (2011).

[176] Y. Dan, Y. Lu, N. J. Kybert, Z. Luo, A. T. C. Johnson, *Nano Lett.* **9**(4), 1472 (2009).

[177] M. Toth, *Appl. Phys. A: Mater. Sci. Process.* **117**(4), 1623 (2014).

[178] A. A. Martin, M. Toth, I. Aharonovich, *Sci. Rep.* **4**, 5022 (2014).

[179] T. C. Isabell, P. E. Fischione, C. O'Keefe, M. U. Guruz, V. P. Dravid, *Microsc. Microanal.* **5**(2), 126 (2002).

[180] A. T. Marshall, *J. Microsc. (Oxford, U. K.)* **133**(1), 119 (1984).

[181] J. J. Hren, *Introduction to Analytical Electron Microscopy.* Plenum Press, New York (1979).

[182] A. A. Martin, M. Toth, *ACS Appl. Mater. Interfaces* **6**(21), 18457 (2014).

[183] S. M. Wetterer, D. J. Lavrich, T. Cummings, S. L. Bernasek, G. Scoles, *J. Phys. Chem. B* **102**(46), 9266 (1998).

[184] K. Fichthorn, R. Miron, *Phys. Rev. Lett.* **89**(19), 196103 (2002).

[185] P. L. Dickrell, N. Argibay, O. L. Eryilmaz, A. Erdemir, W. G. Sawyer, *J. Tribol.* **131**(3), 032102 (2009).

[186] J. Hagymassy, Jr., S. Brunauer, R. S. Mikhail, *J. Colloid Interface Sci.* **29**(3), 485 (1969).

[187] B. Y. Wei, H. M. Lin, H. J. Lai, Y. S. Yang, S. H. Chien, *Rev. Adv. Mater. Sci.* **5**, 306 (2003).

[188] L. Gardner, M. Kruk, M. Jaroniec, *J. Phys. Chem. B* **105**(50), 12516 (2001).

[189] J. Rouquerol, et al., *Pure Appl. Chem.* **66**(8), 1739 (1994).

[190] J. M. Perry, Z. D. Harms, S. C. Jacobson, *Small* **8**(10), 1521 (2012).

[191] C. J. Lobo, M. Toth, R. Wagner, B. L. Thiel, M. Lysaght, *Nanotechnology* **19**(2), 025303 (2008).

[192] A. V. Krasheninnikov, K. Nordlund, *J. Appl. Phys.* **107**(7), 071301 (2010).

[193] R. F. Egerton, P. Li, M. Malac, *Micron* **35**(6), 399 (2004).

[194] J. Barjon, et al., *Appl. Phys. Lett.* **93**(6), 062108 (2008).

[195] J. M. Carlsson, F. Hanke, S. Linic, M. Scheffler, *Phys. Rev. Lett.* **102**(16), 166104 (2009).

[196] V. Adiga, et al., *Phys. Rev. B: Condens. Matter Mater. Phys.* **79**, 245403 (2009).

[197] L. Ostrovskaya, V. Perevertailo, V. Ralchenko, A. Dementjev, O. Loginova, *Diamond Relat. Mater.* **11**, 845 (2002).

[198] C. Popov, et al., *Diamond Relat. Mater.* **17**(7-10), 1229 (2008).

[199] A. E. Vladar, M. T. Postek, R. Vane, in *Proc. SPIE 4344, Metrology, Inspection, and Process Control for Microlithography XV*, vol. 4344, pp. 835–843. 25 February, 2001, Santa Clara, CA, U.S.A., The International Society for Optical Engineering, Bellingham (2001).

[200] W. B. White, K. Rykaczewski, A. G. Fedorov, *Phys. Rev. Lett.* **97**(8), 086101 (2006).

[201] T. Everhart, P. Hoff, *J. Appl. Phys.* **42**(13), 5837 (1971).

[202] S. J. Randolph, J. D. Fowlkes, P. D. Rack, *J. Appl. Phys.* **98**(3), 034902 (2005).

[203] M. R. Bradley, J. M. E. Harper, *J. Vac. Sci. Technol., A* **6**(4), 2390 (1988).

[204] S. Rusponi, C. Boragno, U. Valbusa, *Phys. Rev. Lett.* **78**(14), 2795 (1997).

[205] W. Chan, N. Pavenayotin, E. Chason, *Phys. Rev. B: Condens. Matter Mater. Phys.* **69**(24), 245413 (2004).

[206] Q. Wei, J. Lian, W. Lu, L. Wang, *Phys. Rev. Lett.* **100**(7), 076103 (2008).

[207] R. M. Bradley, P. D. Shipman, *Phys. Rev. Lett.* **105**(14), 145501 (2010).

[208] D. P. Adams, M. J. Vasile, T. M. Mayer, V. C. Hodges, *J. Vac. Sci. Technol., B* **21**(6), 2334 (2003).

[209] A. Botman, A. Bahm, S. Randolph, M. Straw, M. Toth, *Phys. Rev. Lett.* **111**(13), 135503 (2013).

[210] S. Facsko, et al., *Science* **285**(5433), 1551 (1999).

[211] H. Jansen, M. d. Boer, R. Legtenberg, M. Elwenspoek, *J. Micromech. Microeng.* **5**(2), 115 (1999).

[212] A. A. Martin, S. Randolph, A. Botman, M. Toth, I. Aharonovich, *Sci. Rep.* **5**, 8958 (2015).

[213] S. Matsui, T. Ichihashi, M. Mito, *J. Vac. Sci. Technol., B* **7**(5), 1182 (1989).

[214] D. L. Flamm, *Plasma Etching: An Introduction, p. 148.* Academic Press, Boston (1989).

[215] R. Broudy, *Phys. Rev. B: Condens. Matter Mater. Phys.* **1**(8), 3430 (1970).

[216] S. Hong, M. Chou, *Phys. Rev. B: Condens. Matter Mater. Phys.* **57**(11), 6262 (1998).

[217] H. Seiler, *J. Appl. Phys.* **54**(11), R1 (1983).

[218] F. de Theije, O. Roy, N. van der Laag, W. van Enckevort, *Diamond Relat. Mater.* **9**(3–6), 929 (2000).

[219] R. Klauser, et al., *Surf. Sci.* **356**(1–3), L410 (1996).

[220] S. Szunerits, et al., *Electrochem. Commun.* **8**(7), 1185 (2006).

[221] F. C. Frank, K. E. Puttick, E. M. Wilks, *Philos. Mag.* **3**(35), 1262 (1958).

[222] J. C. Angus, T. J. Dyble, *Surf. Sci.* **50**(1), 157 (1975).

[223] F. de Theije, E. van Veenendaal, W. van Enckevort, E. Vlieg, *Surf. Sci.* **492**(1-2), 91 (2001).

[224] M. E. Dudley, K. W. Kolasinski, *J. Electrochem. Soc.* **155**(3), H164 (2008).

[225] Y. Lu, A. R. Barron, *J. Mater. Chem. A* **2**(30), 12043 (2014).

[226] K. Kanaya, S. Okayama, *J. Phys. D: Appl. Phys.* **5**(1), 43 (1972).

[227] F. C. Ziem, N. S. Gotz, A. Zappe, S. Steinert, J. Wrachtrup, *Nano Lett.* **13**(9), 4093 (2013).

[228] K. Ohashi, et al., *Nano. Lett.* **13**(10), 4733 (2013).

[229] O. Benson, *Nature* **480**(7376), 193 (2011).

[230] B. Campbell, A. Mainwood, *Phys. Status Solidi A* **181**(1), 99 (2000).

[231] C. Clark, H. Kanda, I. Kiflawi, G. Sittas, *Phys. Rev. B: Condens. Matter Mater. Phys.* **51**(23), 16681 (1995).

[232] C. Wilbertz, et al., *Nucl. Instrum. Methods Phys. Res., Sect. B* **63**(1-2), 120 (1992).

[233] R. Borret, K. Jousten, K. Böhringer, S. Kalbitzer, *J. Phys. D: Appl. Phys.* **21**(12), 1835 (2000).

[234] B. W. Ward, J. A. Notte, N. P. Economou, *J. Vac. Sci. Technol., B* **24**(6), 2871 (2006).

[235] N. S. Smith, et al., *J. Vac. Sci. Technol., B* **24**(6), 2902 (2006).

[236] C. E. Otis, et al., *J. Vac. Sci. Technol., B* **30**(6), 06F604 (2012).

[237] V. Sidorkin, et al., *J. Vac. Sci. Technol., B* **27**(4), L18 (2009).

[238] M. C. Lemme, et al., *ACS Nano* **3**(9), 2674 (2009).

[239] J. Yang, et al., *Nanotechnology* **22**(28), 285310 (2011).

[240] J. Martin, R. Wannemacher, J. Teichert, L. Bischoff, B. Köhler, *Appl. Phys. Lett.* **75**(20), 3096 (1999).

[241] Z. Huang, et al., *Appl. Phys. Lett.* **103**(8), 081906 (2013).

[242] M. M. Taklo, A. Klumpp, P. Ramm, L. Kwakman, G. Franz, *Microsc. Anal.* **114**(11), 9 (2011).

[243] A. Ferrari, J. Robertson, *Phys. Rev. B: Condens. Matter Mater. Phys.* **64**(7), 075414 (2001).

[244] A. G. Alekseev, et al., *Tech. Phys. Lett.* **26**(6), 496 (2000).

[245] A. Stanishevsky, *Diamond Relat. Mater.* **8**(7), 1246 (1999).

[246] D. M. Toyli, C. D. Weis, G. D. Fuchs, T. Schenkel, D. D. Awschalom, *Nano Lett.* **10**(8), 3168 (2010).

[247] G. Hobler, *Nucl. Instrum. Methods Phys. Res., Sect. B* **115**(1-4), 323 (1996).

[248] A. E. Michel, R. H. Kastl, S. R. Mader, B. J. Masters, J. A. Gardner, *Appl. Phys. Lett.* **44**(4), 404 (1984).

[249] A. J. Steckl, H. C. Mogul, S. W. Novak, C. W. Magee, *J. Vac. Sci. Technol., B* **9**(6), 2916 (1991).

[250] K. H. Junker, J. White, *Surf. Sci.* **382**(1-3), 67 (1997).

[251] I. I. Rzeźnicka, J. Lee, J. T. Yates, Jr., *Surf. Sci.* **600**(19), 4492 (2006).

[252] M. Walczak, A. Johnson, P. Thiel, T. Madey, *J. Vac. Sci. Technol., A* **6**(3), 675 (1988).

[253] B. L. Thiel, M. Toth, *J. Appl. Phys.* **97**(5), 051101 (2005).

[254] M. Bresin, B. L. Thiel, M. Toth, K. A. Dunn, *J. Mater. Res.* **26**(3), 357 (2011).

[255] M. Bresin, M. Toth, K. A. Dunn, *Nanotechnology* **24**(3), 035301 (2013).

[256] G. M. King, G. Schürmann, D. Branton, J. A. Golovchenko, *Nano. Lett.* **5**(6), 1157 (2005).

[257] J. A. Gardener, J. A. Golovchenko, *Nanotechnology* **23**(18), 185302 (2012).

[258] A. Perentes, P. Hoffmann, *J. Vac. Sci. Technol., B* **25**(6), 2233 (2007).

[259] H. Jansen, H. Gardeniers, M. d. Boer, M. Elwenspoek, J. Fluitman, *J. Micromech. Microeng.* **6**(1), 14 (1999).

[260] N. Vanhove, P. Lievens, W. Vandervorst, *Phys. Rev. B: Condens. Matter Mater. Phys.* **79**(3), 035305 (2009).

[261] M. J. M. Vugts, *J. Vac. Sci. Technol., A* **14**(5), 2766 (1996).

[262] M. M. Hills, *Appl. Surf. Sci.* **78**(2), 165 (1994).

[263] B. E. E. Kastenmeier, P. J. Matsuo, G. S. Oehrlein, J. G. Langan, *J. Vac. Sci. Technol., A* **16**(4), 2047 (1998).

[264] I. Utke, V. Friedli, S. Amorosi, J. Michler, P. Hoffmann, *Microelectron. Eng.* **83**(4-9), 1499 (2006).

[265] V. Friedli, I. Utke, *J. Phys. D: Appl. Phys.* **42**(12), 125305 (2009).

[266] D. Nandi, S. A. Rangwala, S. V. K. Kumar, E. Krishnakumar, *Int. J. Mass Spectrom.* **205**(1-3), 111 (2001).

[267] H. F. Winters, F. A. Houle, *J. Appl. Phys.* **54**(3), 1218 (1983).

[268] L. P. Keller, et al., *Science* **314**(5806), 1728 (2006).

[269] D. J. Joswiak, et al., *Meteorit. Planet. Sci.* **47**(4), 471 (2012).

[270] B. Wopenka, *Meteorit. Planet. Sci.* **47**(4), 565 (2011).

[271] S. A. Sandford, et al., *Science* **314**(5806), 1720 (2006).

[272] A. Rotundi, et al., *Meteorit. Planet. Sci.* **43**(1-2), 367 (2008).

[273] G. Matrajt, et al., *Meteorit. Planet. Sci.* **43**(1-2), 315 (2008).

[274] T. Stephan, G. J. Flynn, S. A. Sandford, M. E. Zolensky, *Meteorit. Planet. Sci.* **43**(12), 285 (2010).

[275] S. B. Simon, et al., *Meteorit. Planet. Sci.* **43**(11), 1861 (2008).

[276] P. R. Heck, P. Hoppe, J. Huth, *Meteorit. Planet. Sci.* **47**(4), 649 (2012).

[277] G. A. Graham, et al., *Meteorit. Planet. Sci.* **41**(2), 159 (2006).

[278] H. Leroux, et al., *Meteorit. Planet. Sci.* **43**(1-2), 97 (2008).

[279] S. O. Kucheyev, et al., *Langmuir* **23**(2), 353 (2007).

[280] L. Reimer, *Scanning Electron Microscopy: Physics of Image Formation and Microanalysis*. Springer Verlag, Paris (1998).

[281] G. A. Graham, et al., *Meteorit. Planet. Sci.* **39**(9), 1461 (2004).

[282] E. H. Silver, G. Austin, D. Caldwell, T. Lin, U.S. patent US8831175 B2 (9 September 2014).

[283] T. W. Shanley, A. A. Martin, I. Aharonovich, M. Toth, *Appl. Phys. Lett.* **105**(6), 063103 (2014).

[284] M. Landgraf, M. Müller, E. Grun, *Planet. Space Sci.* **47**(8–9), 1029 (1999).

[285] A. J. Westphal, et al., *Science* **345**(6198), 786 (2014).